Breaking Perceived Limits of Performance for Nanoscale Interrogation & Transport Systems

A THESIS

SUBMITTED TO THE FACULTY OF THE GRADUATE SCHOOL

OF THE UNIVERSITY OF MINNESOTA

BY

Subhrajit Roychowdhury

IN PARTIAL FULFILLMENT OF THE REQUIREMENTS

FOR THE DEGREE OF

DOCTOR OF PHILOSOPHY

Murti Salapaka

March, 2015

© Subhrajit Roychowdhury 2015
ALL RIGHTS RESERVED

Acknowledgements

The journey to this point of completing my PhD has been a culmination of a dream that I had conceived with a very young mind. I feel honored and privileged to have had the opportunity to accomplish what was most coveted to me. I have been through many troughs and crests while pursuing my PhD., but above all it has taught me sheer commitment and holding onto to my goals through all that may come. Looking back, the first and the foremost name that comes to my mind is that of my adviser, Prof. Murti Salapaka. This journey would not have been possible without his supreme guidance. I feel blessed to have had a mentor as dedicated and savant as he is. I am immensely grateful to him for his wise counsel and insights. I can never be more thankful to him for guiding me and inspiring me every day with his acumen and rectitude.

I am indebted to my fellow labmates and friends for their words of encouragement at times when I felt low and celebrating my achievements with me in times I missed my family. This would not have been possible without the the support of Sayan Ghoshal, Shreyas Bhaban, Saurav Talukdar and Mangal Prakash who have been with me during the last few years of this journey. I would like to thank Dr, Hullas Sehgal, Dr. Pranav Agarwal, Dr.Tanuj Aggarwal and Dr.Govind Saraswat, all of who were there to direct me during my initial years when I was a mere novice in this journey. I have been extremely lucky to have found some of the most helpful and supportive friends who have been

nothing short of my pillars of strength here far away from home. Dr. Sauptik Dhar, Dr. Ayan Paul and Sanjoy Dey have each performed there unique shares in providing me strength in times of despair and always being there to share a laugh with.

I am thankful to my parents for encouraging and motivating me to follow my dreams and work towards a my goals. Words cannot express how there blessings have helped me through all my endeavors. I feel blessed to have had parents as understanding and loving as they have been and would earnestly work towards making them proud of me. Finally, I am immensely thankful to my wife, Shatarupa, who has been with through a major part of this journey and always accepted the highs and lows alike with a smile and motivated me to shoot for the sky.

Dedication

To my parents, Prabhat Narayan Roychowdhury and Swapna Roychowdhury, for bringing up rather unruly child of theirs

To my wife, Shatarupa Roychowdhury, for always sharing my dreams and struggle of PhD with a smile.

Abstract

Scientific instruments for nano-interrogation, in particular optical field based probing instruments, typically do not leverage modern control paradigm, thereby constraining themselves to false limits of performance. The first part of my reserach is on developing a novel disturbance estimation paradigm built upon LMI based mixed objective synthesis, which is geared towards systems requiring regulation of a certain system variable against an external disturbance while simultaneously providing a real-time estimate of the disturbance. Examples of such systems include optical traps, scanning probe microscopy, microfluidic sensors, high density data storage systems etc. In general this disturbance is corrupted by process noise (which for nano-scale systems is primarily thermal noise) and the disturbance estimation scheme has to mitigate the effect of such noise to provide any meaningful estimate. In the particular context of the optical field based probing and manipulation, I have experimentally demonstrated more than an order of magnitude improvement in bandwidth over previous state-of-the-art using the aforementioned paradigm. This optimal force clamp will enable biologists to study motor proteins at in-vivo speeds which is not currently possible.

The later part of my research is on control of Brownian ratchet based stochastic transport mechanisms where I have used physical insights to reduce the model complexity in order to analytically derive the approximate evolution of the probability density function of the system state. This allowed for obtaining design parameters for optimal performance, which was missing from the previous literature. I will also demonstrate the advantages of using dynamic programming based multi-objective optimization techniques to obtain transport strategies that strike an optimal velocity-efficiency trade-off. Here a key insight obtained is that maximizing velocity of transport can significantly

compromise efficiency of transport; an aspect not realized/emphasized by researchers in the area. Extensive Monte Carlo simulations demonstrates up to 35% increase in efficiency from other closed loop strategies and more importantly, being an optimal strategy, provides a benchmark of comparison for other heuristic strategies in the domain.

Contents

List of Figures

Chapter 1

Introduction

The current thesis is broadly divided in two parts. One major focus of my research is at the interface where engineering concepts have a direct role to play in physics and biology where a major thrust is on interrogation science and technology for single-molecule studies. Intracellular transport is crucial for many cellular processes where a large fraction of the cargo is transferred by motor-proteins over a network of microtubules. Malfunctions in the transport mechanism underlie a number of medical maladies. The current revolution occurring in bio-science and technology have created a huge demand for high bandwidth interrogation techniques and instrumentation to effectively study the behavior of single bio-molecules under conditions close to their native environment. High bandwidth techniques enable exploration of new spatial and temporal realms essential for corroborating hypotheses, which in turn develop new paradigms that require rethinking traditional notions. Here my instrumentation related research lays the foundations for the next generation of optical tweezers based probing and manipulation and my theoretical studies lays the foundation for semi-analytical approaches to understanding the mechanism of transport where a cargo is carried by multiple carriers.

The other thrust of my research is on Brownian ratchet mechanisms, where noise is

utilized to do useful work at nano-scale. The energetics of motor-protein based transport and their related functionalities can gain much insight from proper understanding of the Brownian ratchet mechanism, as researchers have pointed to the possibility of a similar underlying mechanism in their transport. My work to the limits of performance study for Brownian ratchets based on optimization frameworks will also benefit the field of engineered transport of material at the nano/micro scale manufacturing platforms of the future at large.

The thesis is organized as follows:

- Chapter 1 introduces the work to be described in the thesis and gives an general outline.

- Chapter 2 presents the motivation and methodology of developing a high bandwidth constant force clamp and points out the drawbacks of the existing ones. The approach circumvents the limitations of existing active force clamps with the use of experimentally determined models for various components of the optical tweezing system and using a mixed objective modern control synthesis technique, thus making it possible to probe motor proteins at their native speeds, which was not possible before.

- Chapter 3 describes a semi-analytical methodology that determines the probability distribution function of motor-protein behavior in an exact manner is developed.The method utilizes a finite-dimensional projection of the underlying infinite-dimensional Markov model, which retains the Markov property, and enables the detailed and exact determination of motor configurations, from which meaningful inferences on transport characteristics of the original model can be derived.

- Chapter 4 presents a systematic methodology for designing open-loop Brownian ratchet mechanisms that optimize velocity and efficiency is developed. In the

case where the particle position is available as a measured variable, closed loop methodologies are studied. Here, it is shown that methods that strive to optimize velocity of transport may compromise efficiency. A dynamic programming based approach is presented that provides a systematic way to strike velocity-efficiency trade-off in closed loop, which was lacking from the present literature.

- Chapter 5 presents a way to model the kinesin transport by stochastic ratchet mechanism.
- Chapter 6 presents a final discussion of the work presented in the thesis.
- Appendix A describes the experimental setup that is used for the experimentation described in this thesis.
- Appendix B describes the protocol of the kinesin bead assay used for experimentation described in the thesis.

Chapter 2

High Bandwidth Optical Probing of Motor Proteins

Motor proteins such as kinesin and dynein are critical components of intracellular transport. Their study is important to understand cellular functionality, where malfunction in their transport may cause neuro-degenerative diseases such as Alzheimer's [2, 3]. Optical traps provide an efficient way of probing the motor proteins via bead handles as they enable nm spatial resolution and fN force resolution capabilities[4]. Challenge in furthering the interrogative capabilities of optical tweezer based studies of motor-proteins stem from the significant impact of thermal noise and the nonlinear dynamics of the system.

In optical trap based in-vitro studies, the cargo is attached to the motor protein at the tail domain. The cargo is then optically trapped and brought close to the microtubule, where, heads of the motor protein attach to the microtubule. In the presence of ATP, the motor protein walks on the microtubule while carrying the cargo. The extension of the stalk of the motor molecule (see Fig. 2.1(b)) when it takes a step produces a force on the bead, which displaces the bead from the trap centre x_T. The trap then

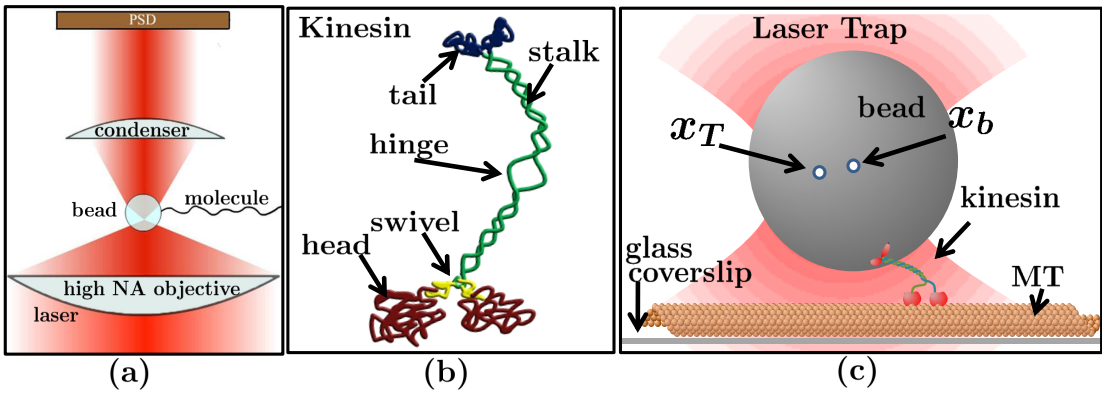

Figure 2.1: (a) Schematic of an optical trap: A collimated laser, passing through a high NA objective, creates a trap for a bead near the focus. The position of the laser on the PSD depends on the position of the bead and provides a measurement of the bead position. (b) Schematic showing the structure of a kinesin: The stalk is approximately 100 nm long and the *heads* are used as legs to walk on Microtubule tracks, while carrying the cargo at the *tail* end. (c) A high resolution method to study kinesin motion is to optically trap the cargo (the bead) carried by the kinesin while it walks on microtubule. The bead position x_b is changed in response to the change in trap position x_T and the force exerted by the kinesin as it moves.

exerts a restoring force in an attempt to bring it back to its centre. The equilibrium position of the bead x_b is thus decided by the balancing of these forces (see Fig. 2.1(c)).

In many in-vitro experimental scenarios, it is important for the biologists to keep the load force constant on the bead despite external disturbances (such as motor stepping and thermal force). This would allow them to simulate the in-vivo condition of constant load force on the cargo which in turn would enable them to study different properties of the molecules accurately under such condition [5]. The constant force clamps, or the *isotonic clamps*, as they are referred sometimes, reported in literature till date basically tries to keep the quantity $x_T - x_b$ constant at steady state by moving the trap as the bead moves. The efficacy of this method depends on the *disturbance rejection bandwidth* (the

disturbance in this case being the motor stepping motion x_m), that is how fast the effects of the protein motion are countered to maintain a constant trapping force. However, the state-of-the-art force clamps have low bandwidths. Therefore they are effective only for slow stepping motions[5, 1] and fail to regulate the trapping force when the protein is moving at a much higher speed (elaborated later). Passive clamps have been used to increase bandwidth, where either a laser is scanned rapidly along a line to create an artificial zero stiffness region or a region on the laser potential is identified where an extent has a constant force. However they are not suitable for probing fast moving motor proteins due to reduced trapping force [6] and limited extent of constant force region [7].

A force regulation on bio-molecules is also important if we are trying to study the energetics of motor motion or any biological phenomenon in general. The work done in extending a bio-molecule is given by the change in Helmoltz free energy if the force is unregulated while the work is given by the change in Gibbs free energy if one can achieve perfect force regulation. One can hypothesize that the work done with a non-perfect force clamp will lie between the two extremes, with the work done being more skewed towards Gibbs free energy with better force regulation. Thus, if the work done is to estimated theoretically using configurational changes using free energies, then a force clamp with higher bandwidth would experimentally yield a work done closer to that given by the theoretical estimate.

Another scenario where a constant force clamp comes in handy is the study of molecular motor stepping. As the force-extension relationship of the motor is highly non-linear in nature, the bead position x_b can be assumed to reflect the motor motion only if a constant force and hence a constant extension for the motor is maintained. Even then, unfolding of motor domains may include hysteresis in the force-extension relationship of the motor. This renders the bandwidth of force regulation very important, as excursion

to nonlinear regions may nullify the aforementioned assumption of constant extension under constant force at steady state. This treatment for isotonic clamps is missing from the current literature and is addressed in this work for the first time.

Also, the current work [8, 9] addresses the issue of lack of real time motor motion estimation that is of importance in several scenarios. Typical scenarios include studying the stepping statistics in real time, specially in multi-motor scenarios (e.g., when kinesin and dynein are pulling a cargo together), where online adjustments of experimental conditions would save experimentation times in contrast to repeating the experiments with readjusted conditions after postprocessing.

Typically, with current schemes, x_b is very noisy mainly because of the presence of thermal noise, and various postprocessing algorithms are used to detect steps in the noisy data. Recent literature shows different attempts from system researchers to suppress the Brownian motion and thereby making x_b less noisy. While supression of Brownian motion is important in many scenarios, in the current application, where the main aim is the detection and estimation of events generated by the system being probed, influencing the system by suppression of Brownian motion might not necessarily lead to a better resolution or bandwidth in discerning the signal/event to be sensed. To circumvent this issue, we take resort to mixed objective H_2/H_∞ controller syntheis, where we minimize the H_∞ norm from the disturbances to force regulation and estimation errors while keeping the H_2 norm from the thermal noise to the estimated signal bounded below a certain value. This way, we avoid influencing the system being probed while still reducing the effect of Brownian noise on the estimated signal. A real time estimation of motor motion can be fed to machine learning based engines that can generate the stepping statistics in real time (or with a constant delay of several samples), which is not possible with bead trace due to very low SNR.

2.1 System modeling

An optically trapped bead carried by a molecular motor can be modeled as a spring mass damper system with stiffness k_T and k_m for the trap and the motor respectively , if the bead displacement from the trap center and the change in the motor extension from the operating condition is small [5]. Let x_T, x_b and x_m denote the positions of the trap center, bead center and the motor head on the microtubule respectively and β represent the viscous damping coefficient. The system has been observed to be highly over-damped and hence the equation of motion of the bead (ignoring geometric effects due to its finite size) in presence of thermal noise η can be written as [5],

$$\beta \dot{x}_b = k_T(x_T - x_b) + k_m(x_m - x_b) + \eta \tag{2.1}$$

Taking Laplace transform and rearranging, we get,

$$x_b(s) = G(s)(k_T x_T(s) + k_m x_m(s) + \eta(s)) \tag{2.2}$$

where $G(s) = \frac{1}{\beta s + k_T + k_m}$. The control hardware and actuation system dynamics have been observed to significantly affect the overall system [10, 11] and thus should be taken into account for a good controller design. The change in trap position $x_T(s)$ for a trap movement command $u(s)$ is given by $x_T(s) = D(s)u(s)$, where $D(s)$ represents the Laplace domain input-output relationship, also termed as the *transfer function*, of the instrument dynamics. Thus, in absence of any motor force and thermal noise, for a given command u, the measured bead position in open loop would be governed by the equation,

$$\tilde{x}_b(s) = x_b(s) + n(s) = k_T G_p(s) D(s) u(s) + n(s) \tag{2.3}$$

where n is the measurement noise and $G_p(s) = \frac{1}{\beta s + k_T}$. If measurement noise is neglected, we can get the frequency response of $H(s) = k_T G_p(s) D(s)$ by giving a sinusoid of varying frequency and measuring the ratio of amplitudes and the phase difference of $x_b(j\omega)$ and

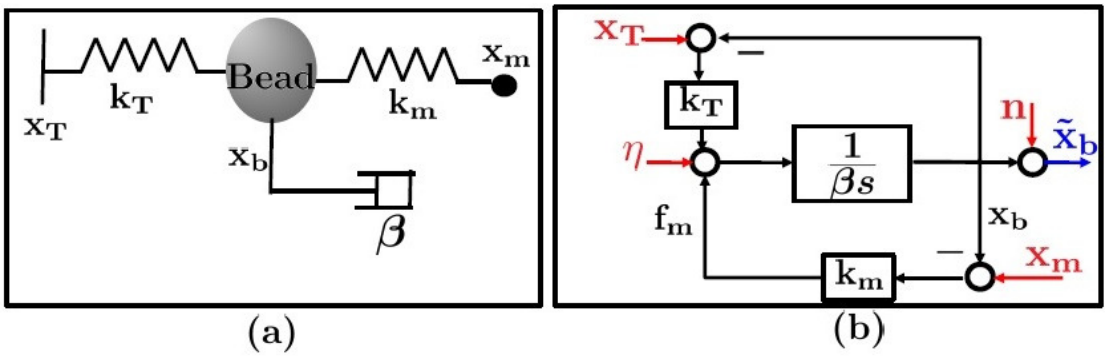

Figure 2.2: (a) The motor protein carrying an optically trapped bead is modeled as a spring mass damper system. For small changes from the nominal force, the motor and the trap can be modeled as linear springs with respective stiffness k_m and k_T. The trap center and the motor head position on the microtubule is denoted by x_T and x_m respectively. The damper signifies the damping effect felt by the bead moving in a viscous fluid. (b) The aforementioned spring-mass-damper model is cast into a block diagram showing the relation among different signals. Here η is the thermal noise and n is the measurement noise.

$u(j\omega)$, which would in turn give us $H(s)$. Also, β and k_T can be measure via Stoke's law and power spectrum respectively. Thus, we can get the instrument dynamics as $D(s) = \frac{H(s)}{k_T G_p(s)}$.

2.2 System identification

The speed limitations in active clamps primarily arise due to the dynamics of the actuators that manipulate the trap position. In existing force clamp designs, the latencies caused by the physics of the actuators are not modeled appropriately, which forms one of the primary causes for limited speeds of operation of these designs. In an acousto optic deflector (AOD) (which is typically used to manipulate trap position in state-of-the-art optical trapping systems), a diffraction grating is created by propagating sound

waves through a crystal. The frequency of the sound wave is controlled by an input radio frequency (RF) wave. The first order diffracted spot created by passing a laser through this grating contains the majority of the light and is used to create a trap. The trap position can be manipulated by altering the input RF frequency, which affects the spacing of the grating caused by a change in the frequency of the sound wave traveling through the crystal. Here the position of the laser spot at the output of the AOD does not settle until the propagating sound wave has crossed the entire width of the laser beam. Thus the limitation in response time of the desired change in the trap location is determined by the velocity of the sound wave traveling in the crystal and the diameter of the laser beam. Another significant issue is caused by the partial reflection of the sound waves at the crystal boundaries. When the input frequency is changed, a mixture of waves of different frequencies exist in the crystal till the reflected waves die out completely. Thus, the time taken by the trap position to settle to its commanded position also depends on how well the sound waves get absorbed at crystal boundaries and the time taken by for the reflected waves to die out[12].

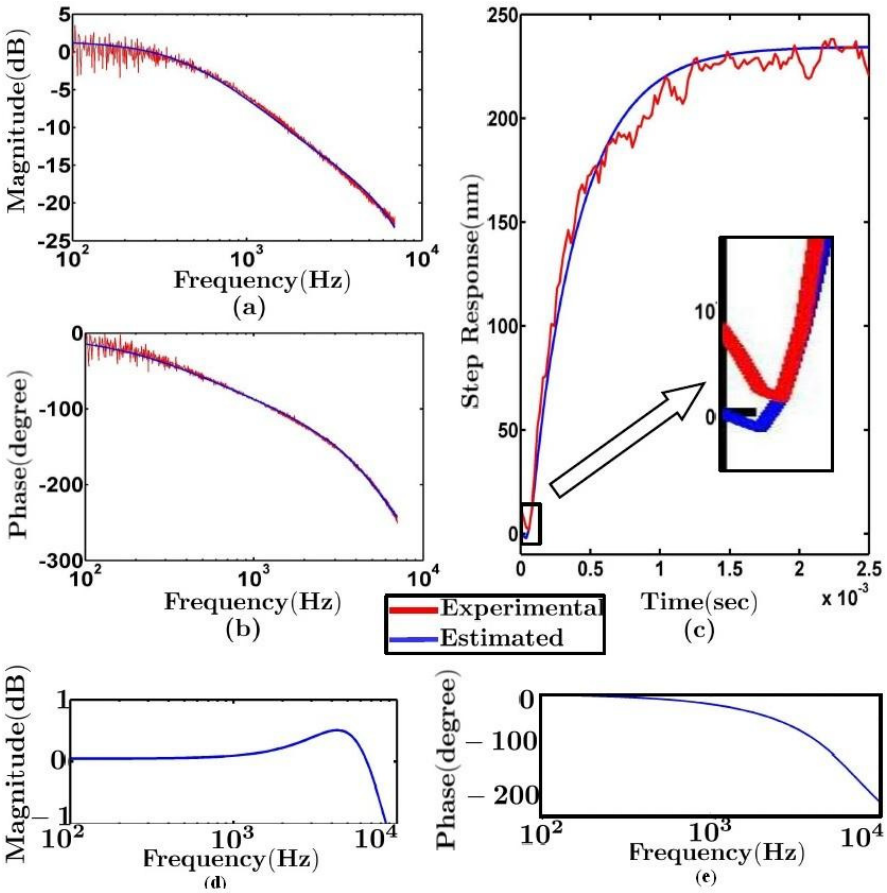

Figure 2.3: The characterization of the system by frequency sweep method is demonstrated here. The red plots in (a) and (b) shows the experimentally obtained magnitude and phase response of the system while the blue curve corresponds to the transfer function fit of the same. (c) validates the estimated transfer function by comparing the simulated step response with the estimated transfer function (blue) with that obtained experimentally. The initial negative kick present in both the experimental and simulated step response (shown inset) is a signature of the delay present in the actuator. (d) and (e) shows the magnitude and phase response of the instrument dynamics respectively, which is extracted from the estimated transfer function and using estimated values for viscous drag coefficient and trap stiffness.

In this work, we incorporate into the design models of components of the optical trapping system including the AOD. Here the trap location x_T manipulable via the AOD exerts a trapping force depending on $x_T - x_b$, x_b being the bead position which is sensed by a photosensitive detector (PSD). Figures 2.3(a)-(c) illustrate the responses of a bead in a trap when the AOD is actuated with known signals. Figures 2.3(a) shows the amplification in the amplitude of the sinusoidal bead motion (as measured by the PSD) obtained when the AOD is commanded to change the trap location sinusoidally over a range of frequencies. Here the phase shown in Figure 2.3(b) is the phase lag of the response sinusoid with respect to the command sinusoid provided to the AOD. This frequency response data can be used to obtain the *transfer function* (Laplace domain input-output relationship that describes the dynamic relationship between the actuation input to the AOD and the PSD measurement)[13]. As alluded to earlier, the AOD physics describing the latencies can be quite complicated. However, the model of the AOD obtained using the experimentally obtained frequency response is accurate; indeed, as is evident from Figure 2.3(c), for the AOD and the experimentally obtained responses when the trap location is commanded to change by a step, quantitatively matches the response predicted by the model. It is also evident from the inset in Figure 2.3(c) that the bead initially moves in a direction opposite to the commanded direction which is a signature of delays present in the system [13]. Such behavior cannot be explained by the spring-mass-damper[5, 4] models typically used to describe trap dynamics alone (see supplemental text for more details). The transfer function $D(s)$ from the trap movement command u, provided as an input to the AOD, and the actual trap movement x_T, is determined to be $D(s) = \frac{0.66(s^2 - 7.98\times10^4 s + 2.78\times10^9)}{s^2 + 5.51\times10^4 s + 1.81\times10^9}$ (also see supplemental text for details). The corresponding frequency response $D(j\omega)$ is shown in Figure 2.3(d) and 2.3(d)(e), which is obtained by setting $s = j\omega$ at various angular frequencies ω. $|D(j\omega)|$ signifies the amplification and $\tan^{-1} D(j\omega)$ signifies the phase lag

from input to output for an input sine-wave of frequency ω. It can be seen that as the phase lag becomes significant at higher frequencies, the assumption that trap position moves instantaneously in response to the input command (or, in other words $D(s)$ can be treated as unity) remains valid only for low frequencies. Violation of this assumption would not only prevent from achieving desired performance at higher frequencies, but may introduce instability in the system as well[7].

We emphasize that unlike current works, it is not assumed that the trap position x_T is manipulable directly. However, as we have modeled the AOD dynamics, the trap position x_T can be estimated from the trap command u using the model $D(s)$. For slow stepping motion, the disturbance effects on the trap are predominantly in the low frequency and therefore approximating $D(s)$ by unity (and thus $u = x_T$) is valid whereas for fast stepping motion it is not. For fast stepping motion, $x_T \neq u$ and thus the error in force regulation $e_f = f_d - k_T(x_b - x_T)$ (where f_d is the desired force to be maintained and k_T is the stiffness of the trap) cannot be directly estimated, rendering active force clamps which depend on error e_f ineffective for high bandwidth studies. To circumvent this issue, in this letter we provide a new method that does not rely on the regulated variables (such as e_f) to be measurable to achieve the goals of regulating a constant trapping force.

2.3 Design Objectives

Figure 2.4 provides a block diagram view of the framework where blocks in the figure represent transfer functions. The bead position x_b is fed back to the controller K along with the desired force command f_d, which then generates the command u to move the trap position x_T. The controller, unlike in traditional schemes, also provides an estimate $\hat{x}_m$ for the stepping motion x_m. We use the notation $T_{ab}(s)$ and $T_{ab}(j\omega)$ to denote the transfer function and the frequency response from an input a to an output b

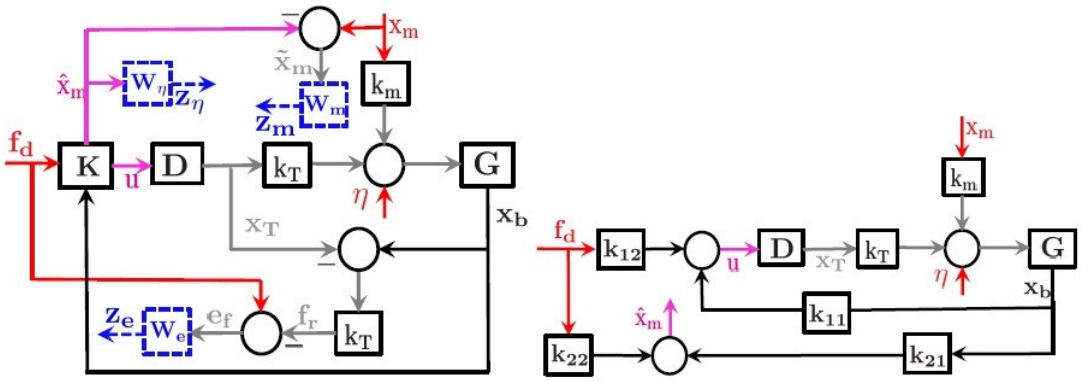

Figure 2.4: Block diagram on the left hand elaborating the modern controller design paradigm. Red signals denote system inputs (commands or disturbances), magenta signals denote controller outputs, black signals denote the observable signals while the grey signals denote the unobservable ones. Blue boxes denote the weighting functions that capture the performance specifications and the corresponding blue signals are fictitious signals introduced during the design phase to meet various design objectives. Here the aim is to obtain an estimate $\hat{x}_m$ of motor motion x_m, with small influence of the thermal noise η on the estimate $\hat{x}_m$, while maintaining the force f_r on the motor regulated at a desired value f_d. Here G denotes the plant transfer function, D denotes the AOD transfer function (the variable s in dropped for notation convenience), k_T and k_m denote the trap and (simulated) motor stiffness respectively. The weighting functions $W_e(s)$, $W_\eta(s)$ and $W_m(s)$ capture the objectives of force regulation (e_f being the error between desired and achieved load force) , limiting the effect of thermal noise on stepping motion estimate and step estimation bandwidth respectively. The right hand block diagram shows the control architecture and the different filters embedded in the controller K. k_{11} and k_{12} produces the control signal for force regulation while k_{21} and k_{22} generates the estimate of motor stepping motion.

respectively. Also, we use the notation $||T_{ab}||_\infty = \max_\omega |T_{ab}(j\omega)|$ to denote the maximum amplification from a to b over all frequencies and $||T_{ab}||_2 = (\frac{1}{2\pi}\int_0^\infty |T_{ab}(j\omega)|^2 d\omega)^{\frac{1}{2}}$ to denote the rms of the output b due to a white noise input a. The design requirements can be listed as follows:

- A small value of $\|T_{x_m e_F}\|_{H\infty}$ would ensure that the motor stepping motion doesn not significantly alter the force on the system, which is the main objective of the isotonic clamp. The range of frequencies for which we want to impose this objective is captured in z_e by the corresponding weighting function W_e.

- For good command tracking $\|T_{f_r e_F}\|_{H\infty}$ should be small, where f_r is the desired force to be maintained on the molecule.

- For good estimation of motor motion, $\|T_{x_m \tilde{x}_m}\|_{H\infty}$ should be small, where $\tilde{x}_m = \hat{x}_m - x_m$ denotes the error in estimation of motor motion. z_m captures the desired bandwidth of estimation through W_m.

- To minimize the effect of thermal noise on the estimate of the motor motion, $\|T_{\eta \hat{x}_m}\|_{H_2}$ should be small. z_η captures the desired range of filtering via W_η.

- To avoid losing the bead from the trap due to sudden spikes in trap position, we require $\|T_{x_m x_T}\|_{H\infty} \leq 1$, as that would ensure that the input disturbance is not magnified to the trap position. Also, for the linearity assumptions to hold good, trap movement should be small.

- Any controller should be robust enough to endure certain variation of the motor spring constant k_m.

- It has been observed that a good controller should be able to take care of the measurement noise in similar systems and thus no additional objective is required to be specified.

It can be seen that the requirements for different objectives are competing and thus all of them can not be satisfied simultaneously for all frequencies. Hence in the controller design, we emphasize different objectives in different designs while still achieving good

enough bound for the rest. The different controllers that we design are important for different experimental scenarios.

Weighting functions, denoted by blue dashed boxes in Figure 2.4, allow for the specification of frequency ranges in which a certain objective needs to be achieved. Appropriate selection of weighting function also ensures varying degrees of emphasis on different objectives. Once the problem is cast in the framework mentioned above, solution of the related optimization problem [14] yields a controller that meets the specified design requirements with guaranteed performance limits set by γ_f, γ_m and ν_m. Note that the underlying optimization problem is a non-convex one and is a hard problem to solve. We apply the transformations mentioned in the next section to map it into an equivalent convex optimization problem, whose solution can be obtained by solving a set of linear matrix inequalities. The details of the methodology can be found in the next section. We mention here that if the design requirements become too stringent, the solution to the related optimization problem becomes infeasible. Relaxation of constraints is then required by changing the weighting functions and the performances limits to make the problem feasible.

2.4 Mixed-objective controller design

In this section, we give a brief overview of multi-objective controller synthesis via LMI based approach. The main advantage that this approach offers is that different objectives can be specified for different I/O channels, thus allowing for the flexibility of weighing some objectives more than others for an optimized controller synthesis. In this approach, all the objectives are cast into a set of LMI via Lyapunov shaping paradigm, and thus the controller synthesis problem boils down to solving that set of LMI.

Consider a generalized plant P having the following state space realization,

$$P\begin{cases}\dot{x} = Ax + B_w w + Bu \\ z = C_z x + D_{zw} w + D_z u \\ y = Cx + D_w w\end{cases} \tag{2.4}$$

where u is control input, y is measured output, w is a vector of exogenous inputs and z contains performance related fictitous outputs. Considering our control signal to be $u = Ky$, where the controller K admits the state space realization $[A_k, B_k, C_k, D_k]$, we obtain the closed loop transfer function Ψ from w to z having state space realization $[\mathcal{A}, \mathcal{B}, \mathcal{C}, \mathcal{D}]$.

A specific closed loop channel Ψ_j from w_j to z_j with an assigned objective can be selected as $\Psi_j = L_j \Psi R_j$, where L_j and R_j satisfies $w = R_j w_j$ and $z_j = L_j z$. The state space form of Ψ_j can be obatined as,

$$\left[\begin{array}{c|c} \mathcal{A} & \mathcal{B}_j \\ \hline \mathcal{D}_j & \mathcal{C}_j \end{array}\right] = \left[\begin{array}{cc|c} A + BD_kC & BC_k & B_j + BD_kF_w \\ B_kC & A_k & B_kF_w \\ \hline C_j + E_jD_kC & E_jC_k & D_j + E_jD_kF_j \end{array}\right] \tag{2.5}$$

where $B_j = B_w R_j$, $C_j = L_j C_z$, $D_j = L_j D_{zw} R_j$, $E_j = L_j D_z$ and $F_j = D_w R_j$. Our objective is to synthesise a single controller K that would meet all the performance requirements for different channels and internally stabilize the system. We next discuss briefly how the H_∞ and H_2 objectives for a given Ψ_j can be captured in an LMI framwork by the use of KYP lemma.

- $\mathcal{A}$ is internally stable and $\|\Psi_j\|_{H_\infty} < \gamma$ iff there exists a symmetric $P_j > 0$ such that

$$\begin{pmatrix} \mathcal{A}^T P_j + P_j \mathcal{A} & P_j B_j & C_j^T \\ B_j^T P_j & -\gamma I & D_j^T \\ C_j & D_j & -\gamma I \end{pmatrix} < 0 \tag{2.6}$$

- $\mathcal{A}$ is internally stable and $\|\Psi_j\|_{H_2}^2 < \nu$ iff there exists symmetric $P_j = S_j^{-1}$ and Q satisfying $\mathrm{Tr}(Q) < \nu$ such that

$$\begin{pmatrix} \mathcal{A}^T P_j + P_j \mathcal{A} & P_j B_j \\ B_j^T P_j & -I \end{pmatrix} < 0, \begin{pmatrix} P_j & C_j^T \\ C_j & Q \end{pmatrix} > 0, D_j = 0 \tag{2.7}$$

  where S_j satisfies $\mathcal{A} S_j + S_j \mathcal{A}^T + B_j B_j^T < 0$.

Expressions like $\mathcal{A}^T P_j + P_j \mathcal{A}$ make the problem nonlinear and hence not easily tractable because of the presence of products of P_j and controller variables. To make the LMI optimization problem convex and affine in LMI variables, the following steps are done.

- The constraint $P_1 = P_2 = \ldots = P_m = P$ is imposed from Lyapunov shaping paradigm, the Lyapunov matrix P is made to be equal for all performance channels.

- A change of variable is done to introduce a new set of LMI variables $X = \{\mathfrak{A}, \mathfrak{B}, \mathfrak{C}, \mathfrak{D}, \mathfrak{X}, \mathfrak{Y}\}$.

The transformations give the following set of LMIs for respective performance channels to obatin a stabilizing controller.

- $\|\Psi_j\|_{H_\infty} < \gamma$ yields $\mathfrak{F}_1(X)^1 \ < 0 \ \mathfrak{F}_2(X)^2 \ > 0$

- $\|\Psi_j\|_{H_2}^2 < \nu$ yields $\mathfrak{H}_1(X)^3 \ < 0$, $\mathfrak{H}_2(X)^4 \ > 0$, $\mathfrak{H}_3(X)^5 \ < \nu$, $\mathfrak{H}_4(X)^6 \ = 0$

---

1 $\begin{pmatrix} \mathfrak{S}(A\mathfrak{X} + B\mathfrak{C}) & \mathfrak{A}^T + (A + B\mathfrak{D}C) & * & * \\ \mathfrak{A} + (A + B\mathfrak{D}C)^T & \mathfrak{S}(A\mathfrak{Y} + \mathfrak{B}C) & * & * \\ (B_j + B\mathfrak{D}F_j)^T & (\mathfrak{Y}B_j + \mathfrak{B}F_j)^T & -\gamma I & * \\ C_j\mathfrak{X} + E_j\mathfrak{C} & C_j + E_j\mathfrak{D}C & D_j + E_j\mathfrak{D}F_j & -\gamma I \end{pmatrix} < 0$

2 $\begin{pmatrix} \mathfrak{X} & I \\ I & \mathfrak{Y} \end{pmatrix} > 0$

3 $\begin{pmatrix} \mathfrak{S}(A\mathfrak{X} + B\mathfrak{C}) & \mathfrak{A}^T + (A + B\mathfrak{D}C) & B_j + B\mathfrak{D}F_j \\ \mathfrak{A} + (A + B\mathfrak{D}C)^T & \mathfrak{S}(A\mathfrak{Y} + \mathfrak{B}C) & \mathfrak{Y}B_j + \mathfrak{B}F_j \\ (B_j + B\mathfrak{D}F_j)^T & (\mathfrak{Y}B_j + \mathfrak{B}F_j)^T & -I \end{pmatrix} < 0$

4 $\begin{pmatrix} \mathfrak{X} & I & (C_j\mathfrak{X} + E_j\mathfrak{C})^T \\ I & \mathfrak{Y} & (C_j + E_j\mathfrak{D}C)^T \\ C_j\mathfrak{X} + E_j\mathfrak{C} & C_j + E_j\mathfrak{D}C & Q \end{pmatrix} > 0$

5 $\mathrm{Tr}(Q) < \nu$

6 $D_j + E_j\mathfrak{D}F_j = 0$

where $\mathfrak{S}(A)$=$A + A^T$.

Solution of entire set of LMIs for all channels gives us the values of $\mathfrak{A}, \mathfrak{B}, \mathfrak{C}, \mathfrak{D}, \mathfrak{X}, \mathfrak{Y}$, from which the controller variables can be recovered as follows:

$$\begin{aligned} A_k &= N^{-1}(\mathfrak{A} - NB_kC\mathfrak{X} - \mathfrak{Y}BC_kM^T \\ &\quad -\mathfrak{Y}(A + BD_kC)\mathfrak{X})M^{-T} \\ B_k &= N^{-1}(\mathfrak{B} - \mathfrak{Y}BD_k) \\ C_k &= (\mathfrak{C} - D_kC\mathfrak{X})M^{-1} \\ D_k &= \mathfrak{D} \end{aligned} \tag{2.8}$$

where $M,\ N$ are found by using $MN^T = I - \mathfrak{X}\mathfrak{Y}$.

Here note that the performance bounds γ and ν enters the LMI linearly and hence can be considered as LMI variables for the channels whose performances we want to optimize. Then an appropriate function of all those γ and ν should be minimized subject to the set bounds in the remaining channels to obtain an optimized controller.

$\mathbf{H_2/H_\infty}$ mixed synthesis: Suppose we have two closed loop performace channels Ψ_1 and Ψ_2, where we want to find a stabilizing controller that would minimize $\|\Psi_1\|_{H_\infty}$ subject to $\|\Psi_2\|_{H_2} < \nu$. To cast the problem in LMI framework, we introduce a new LMI variable γ and find a solution for the complete set of LMIs corresponding to $\|\Psi_1\|_{H_\infty} < \gamma$ and $\|\Psi_2\|_{H_2} < \nu$ that would minimize γ.

$\mathbf{H_\infty}$ synthesis: To find a stabilizing controller that would minimize $\|\Psi\|_{H_\infty}$ for a closed loop system Ψ, we introduce a new LMI variable γ and find a solution for the set of LMIs corresponding to $\|\Psi\|_{H_\infty} < \gamma$ that would minimize γ.

Figure 2.9 shows the different exogenous input signal vector w, weighted output signal vector z, measurement signal vector y and control signal vector $\hat{u}$ in the open loop system (on the left) and the system cast in a modern control framework (on the

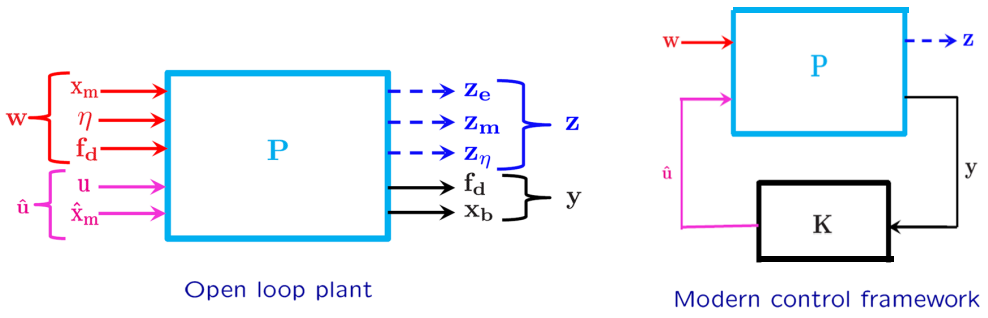

Figure 2.5: Figure showing the exogenous input signal vector w, weighted output signal vector z, measurement signal vector y and control signal vector $\hat{u}$ in the open loop system (on the left) and the system cast in a modern control framework (on the right).

right). The transfer matrix of the open loop plant P from $[w\ \hat{u}]^T$ to $[z\ y]^T$ is given as

$$P = \left[\begin{array}{ccc|cc} -W_e k_T k_m G & W_e k_T G & 0 & W_e k_T D(1-k_T G) & 0 \\ 1 & 0 & 0 & 0 & -1 \\ 0 & 0 & 0 & 0 & W_\eta \\ \hline 0 & 0 & 1 & 0 & 0 \\ k_m G & G & 0 & k_T D & 0 \end{array}\right]. \tag{2.9}$$

Let's define the closed loop transfer matrix Ψ from w to z as

$$\Psi = \left[\begin{array}{c|c} A_k & B_k \\ \hline C_k & D_k \end{array}\right], \tag{2.10}$$

where $z = \Psi w$. In this approach, instead of choosing the controller K that would minimize $||\Psi||_\infty$, we choose the following performance channels:

- Ψ_1 : From x_m to z_e
- Ψ_2 : From x_m to z_m
- Ψ_3 : From η to z_η

and choose our controller K to minimize $||\Psi_2||_{H_\infty}$ subject to $||\Psi_1||_{H_\infty} < \gamma$ and $||\Psi_3||_{H_2} < \nu$. Thus this approach helps avoid posing artificial constraints on all channels thereby enhancing the performance of the channels of interest.

2.5 Experimental Results

2.5.1 Model system

For experimental studies, we employed optical tweezers with a trap stiffness of $k_T = 0.015$pN/nm and a bead with drag coefficient $\beta = 1.7 \times 10^{-5}$pN-s/nm. The desired force to be maintained, f_d, is set at 2.4pN. The disturbance simulating the motor stepping motion is realized for an effective motor stiffness of $k_m = 0.3$pN/nm. The motor stepping motion is simulated by giving square pulse disturbances with 50% duty cycle with a time period which is double the intended dwell time of the stepping motion. The estimated $D(s)$ is used to compute x_T from u in the analysis below. Using a dedicated field programmable gate array (FPGA) to implement the controller, a loop closure rate of 100kHz (significantly faster than existing force clamps[5, 1] where this is less than 1kHz) was achieved, which is critical in achieving the desired performance.

Histograms in Figure 2.6(a) and (b) show the quality of the force regulations achieved against simulated motor velocities of 400nm/s and 10μm/s respectively, where the control scheme[1] ignores the AOD dynamics (or in other words, assumes $D(s) = 1$) and updates the trap position as $u = x_{bf} - x_{bT}$, where x_{bf} is the filtered version of x_b and x_{bT} is the desired distance to be maintained between the trap and the bead center. The bead position x_b is filtered to minimize the high frequency noise, so that the assumption $u = x_T$ (or $D(s) = 1$) remains valid. It is evident from the figure that the above scheme is limited for force regulation on motor proteins moving slowly (400mn/s, similar to what is achieved in [1] but not on motor proteins moving at significantly higher

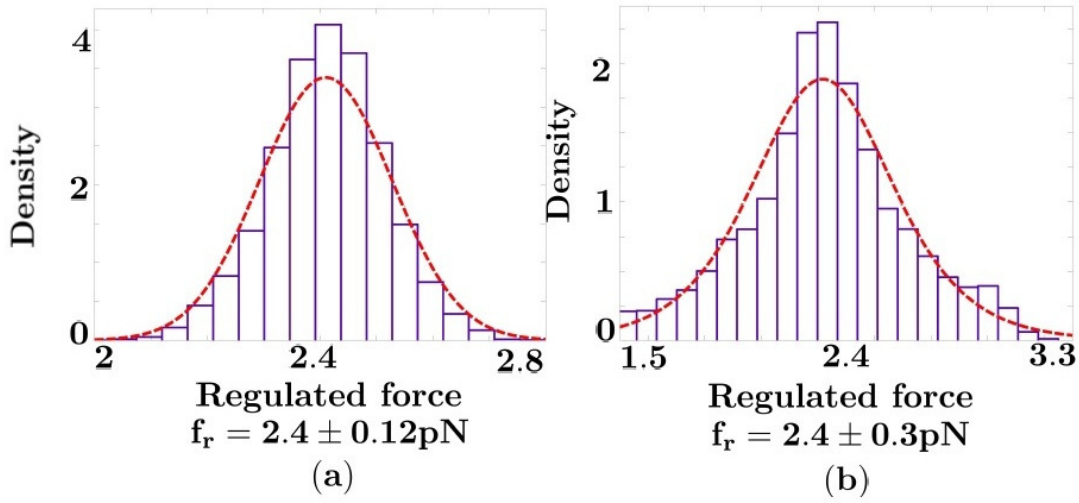

Figure 2.6: Histograms showing the force regulation achieved with a traditional control scheme[1] for different square pulse disturbances: (a) amplitude 8nm and dwell time 20ms, which corresponds to a motor velocity of 400nm/s and (b) amplitude 25nm and dwell time 2.5ms, which corresponds to a motor velocity of 10μm/s. It can be seen from the histograms that the controller maintains the force within 5% of desired value for lower motor velocity whereas the regulation deteriorates (12.5%) for higher motor velocity.

velocities (10μ/s).

Histograms in Figure 2.7(a) and (b) show the force regulations achieved for the same simulated motor velocities as in the previous case with an optimal controller designed following our method which incorporates the estimated $D(s)$, where the only objective is force regulation. Here the controller is suitable for force regulation on motor proteins moving at velocities that are an order of magnitude or more than achieved in [5, 1]. The limitation on achievable bandwidth is now caused by the bead-handle dynamics (how fast the bead can respond to the motor motion), which is common to all active as well as passive clamps. Clearly, the limitations of low disturbance rejection bandwidth and instability about feedback based force clamps, as mentioned in [7] can be overcome.

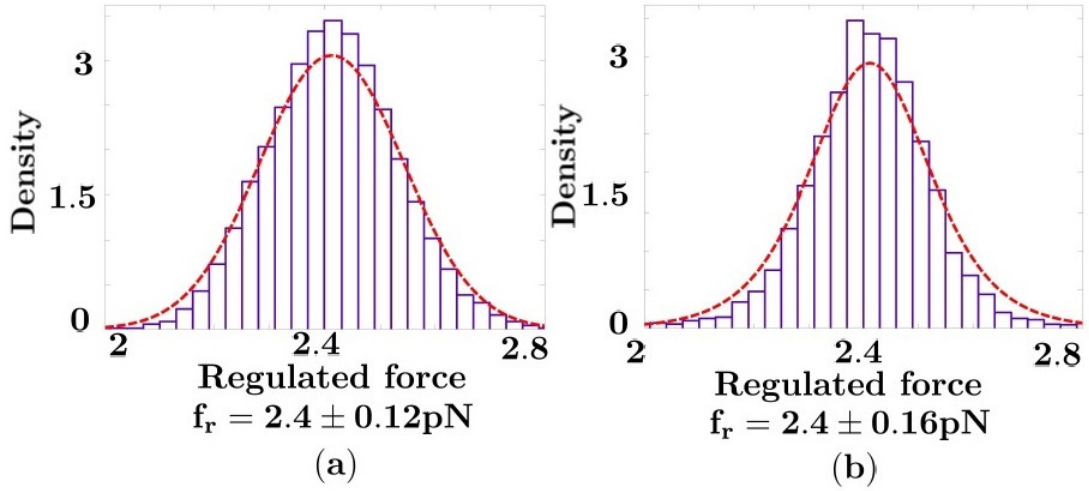

Figure 2.7: Histograms showing the force regulation achieved with an *optimal* controller with the only objective of force regulation for different square pulse disturbances: (a) amplitude 8nm and dwell time 20ms, which corresponds to a motor velocity of 400nm/s and (b) amplitude 25nm and dwell time 2.5ms, which corresponds to a motor velocity of 10μm/s. It is evident from the histograms that the controller maintains the force within 6.7% of desired value even for high frequency high magnitude disturbances (higher velocity).

Another limitation arises due to the presence of right half plane zeros in the AOD dynamics (see $D(s)$), which poses a fundamental limit on the achievable performance [11].

Figure 2.8(a) and (b) demonstrates the *real-time* step estimation capability achieved by our method while Figures 2.8(e) and (f) show that corresponding force regulations are within satisfactory limit so that bead displacement can be used to infer motor motion without the need for linkage corrections[5]. The corresponding noisy bead position traces are shown in Figure 2.8(c) and (d) from which the steps are typically estimated offline.

2.5.2 Kinesin bead assay

To verify the performance of the force clamp on actual biological systems, we prepared a kinsein bead assay system with 1μ diameter beads. The motor proteins are attached to the bead via appropriate biochemistry. The beads are then trapped by an optical trap and the kinesin is placed on microtubule tracks to facilitate their walking by manipulating the laser and stage positions. When the kinesin starts walking and in the process increses the force on the bead, the clamp is not engaged till the desired force builds up. At this point, the force clamp automatically engages and the trap position is controlled to keep constant force on the motor till the limit of the detection system range. The automatic engagement and action of the force clamp is demonstrated in Figure 2.9.

Figure 2.10 demonstrates the advantage of the modern control based design over the traditional force clamp. The histograms shows the variation of the force from the desired point as the motors move for the two control schemes. Here the desired force to be regulated is set to 0.8pN. The low load force is chosen as it is tougher to regulate against a low load force as either the thermal noise is a bigger fraction of the desired $x_b - x_t$ to be regulated for same stiffness or the stiffness is lower increasing the thermal noise. We have seen in the model system that both force clamps performs similarly for higher load force and slower speed with the modern control based clamp outperforming the traditional one only at higher speeds, whereas for lower load forces the modern control based clamp clearly outperforms the traditional clamp even at lower speeds. This opens up the possibility for biologists to investigate motor proteins at sub-piconewton load forces, which to the best of my knowledge has not been reported with the force regulation achieved.

Figure 2.11 demonstrates the real-time step estimation capability of the control scheme. The red trace corresponds to the bead motion while the blue trace corresponds

to the estimated motor motion. Although the estimated signal can not give the true step-sizes, it gives the edges or starting points of the steps which can be exploited further by approximate dynamic programming or SVM based learning algorithms to reconstruct the motor motion and generate the stepping statistics in real time or with a constant delay of several samples. Raw bead trace being extremely noisy is not useful for these learning algorithms to extract steps online. Also, making sure that only one motor is attached (by dilution experiments) would keep the step size constant and thus enhance the estimated signals which in the present scenario is corrupted by smaller steps due to presence of multiple active motors attached to the bead.

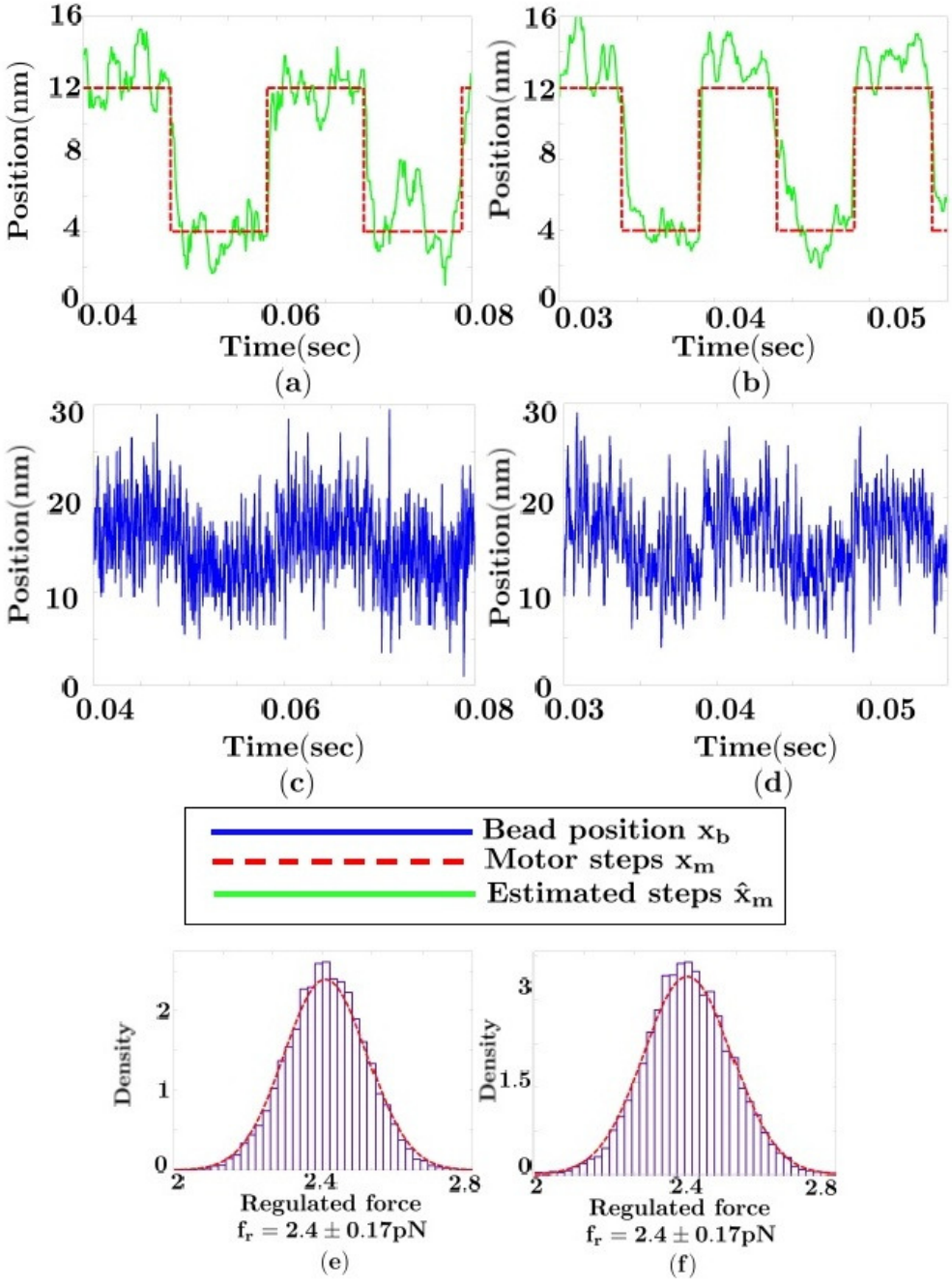

Figure 2.8: The real time step estimation for step size 8nm is demonstrated for (a) dwell time 10ms, which corresponds to a motor velocity 800nm/s and (b) dwell time 5ms, which corresponds to a motor velocity 1600nm/s. (c) and (d) shows the corresponding noisy bead position measurements, from which the steps are typically estimated via post-processing, while (e) and (f) shows the corresponding force regulation achieved.

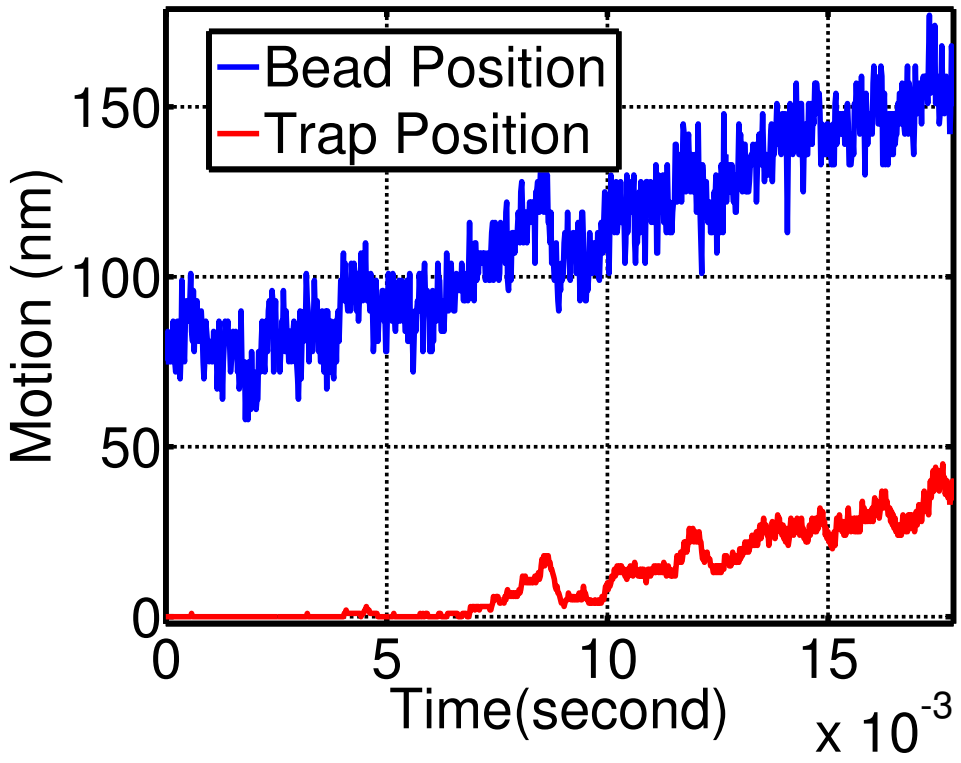

Figure 2.9: Figure showing the engagement and action of a force clamp as the kinesin walks. The blue trace shows the bead position x_b while the red trace shows the position of the trap x_t as it follows the bead in an isotonic clamp. In the initial part $x_b - x_t$ is less than the desired distance and the force clamp does not engage. When it exceeds a preset value as the kinesin walks, the clamp engages and a constant $x_b - x_t$ is maintained.

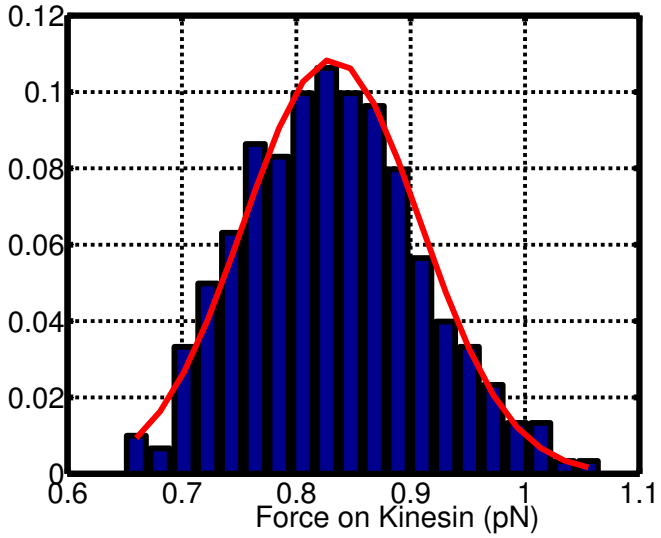

(a) Traditional force clamp

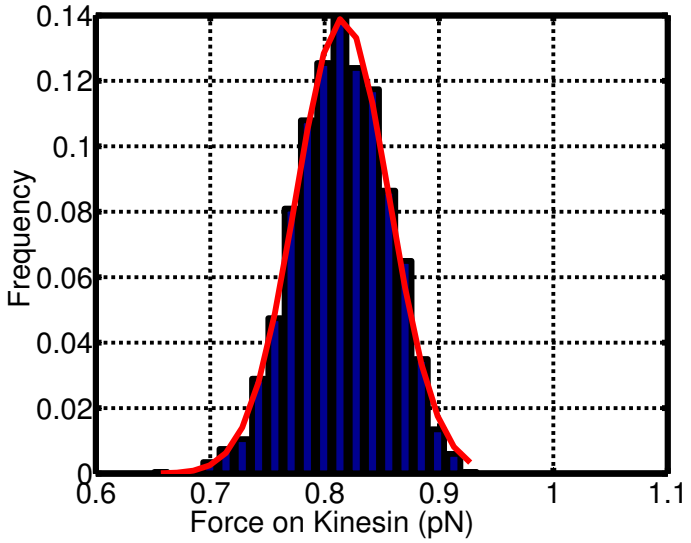

(b) High BW force clamp

Figure 2.10: Figure showing the comparison of force regulations of different force clamps. (a) shows the histogram for the traditional force clamp while (b) shows that for the modern control based force clamp. Both of the clamps attempted to regulate a force of 0.8pN on motors moving approximately at 200nm/s. The modern control based clamp achieves a regulation of 4.9% in contrast to 9.8% of that achieved by the traditional clamp.

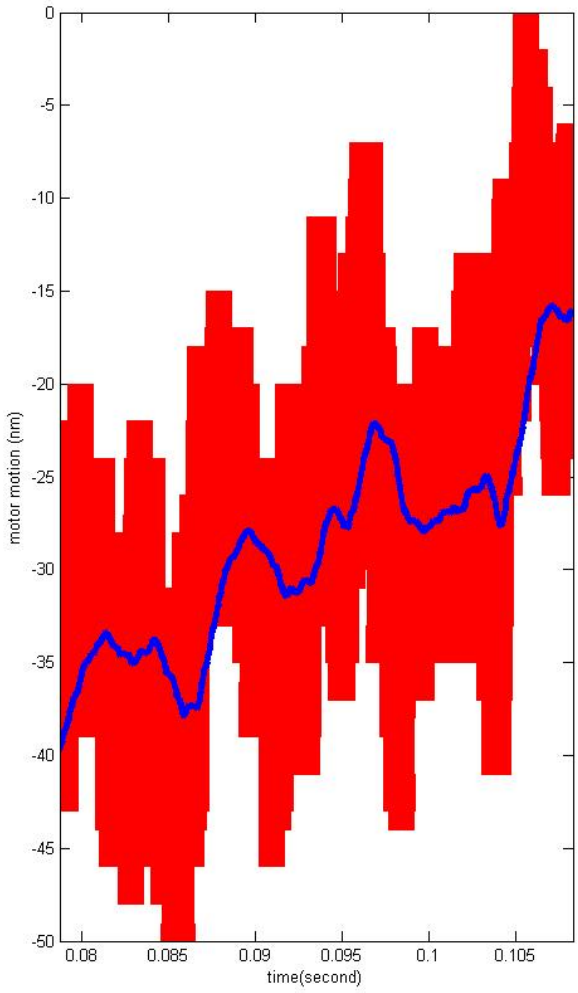

Figure 2.11: Figure showing the real time motor motion estimation scheme. The red trace shows the bead motion while the blue trace shows the estimated motor motion.

Chapter 3

An exact approach for studying cargo transport by an ensemble of molecular motors

The behavior of motor proteins is relatively well characterized when one motor protein is involved in the transport of a cargo. Indeed, it is possible to monitor the motion of a single molecular motor under highly tunable experimental conditions and obtain measurements with sufficiently accurate spatial and time resolution [15, 16, 17]. The resulting experimental data has led to many theoretical descriptions of motor-protein mechanisms which take into account the complex mechanochemical processes involved and yield insights into transitions between the multiple conformational states possible [18].

In vivo, often, an ensemble of molecular motors is responsible for the transport of a common cargo [19, 20]. *In vitro* and simulation studies where multiple motors are involved in transport have provided unique insights into features of a common cargo being transported by many motors (see for example, [21, 22]). The dynamics when multiple

motors transport cargo can be considerably more involved where a number of significant questions remain open. For example, it is not yet clear when and if motors synchronize their behavior, whether they move independently and whether they are antagonistically engaged in a "tug-of-war" [20, 23]. Despite major improvements in instrumentation and techniques, understanding behavior of multiple coupled motors remains extremely challenging. The main difficulty is the substantially higher spatial and temporal resolution needs imposed by the fractional motion of the cargo and the increased number of possible transitions between conformational states [24, 22]; possibilities introduced by the multiplicity of motors carrying a single cargo.

The available detailed characterization of how single motors transport cargo can be leveraged to develop models that describe how multiple-motors coordinate the motion of a common cargo. Indeed, using single molecule experimental data, accurate descriptions on the probability that a motor takes a step and its dependence on environmental factors such as temperature and ATP concentration, are reported in [25, 26, 27]. Similar estimates on the attachment and detachment rates of molecular motors to and from a microtubule can be found in [28, 27, 29]. A model that describes how multiple motors carry a common cargo can be obtained by using the information on single motor protein behavior and by introducing the coupling of the individual motor-proteins via the dynamics of the shared common cargo. Using Monte-Carlo simulations on such a model, [21] reported novel insights into the behavior of kinesin motors, such as, a smaller velocity of transport of cargo when carried by multiple motors as opposed to a single one, and a dependence of the expected run-length on the stiffness of the motor linkage. While Monte-Carlo techniques form an important set of tools, they involve a trade-off between the accuracy desired and the computational effort needed. As a consequence, important features of the dynamics, especially if associated with rare events, can be missed. This aspect takes particular significance in the study of biological systems,

where pathological behaviors are caused or triggered by events which are improbable under normal conditions but occur with significant adverse impact.

Existing approaches have utilized models with simplifying assumptions that can be treated analytically or semi-analytically in order to understand the basic features of the coordinated motion of motor proteins. For example, in [30] mean-field theory is applied for analyzing large ensembles of motors, whereas, in [31] the cooperative transport of cargo realized by two motor proteins is studied in order to identify distinct operational regimes. In [28] apart from providing estimates of attachment and detachment rates of motors to microtubules, analytical dependence of run-length on the number of motors involved in the transport of a common cargo is obtained.

In this article, we present a general methodology which determines the probability distribution function of various motor behaviors[32, 33]. This different approach provides several advantages over Monte-Carlo simulation based methods. In our method the probabilities of outcomes are determined exactly, unlike Monte-Carlo simulation based methods; however, our method does not sacrifice the detailed description of the system possible with Monte-Carlo simulations. Our strategy is particularly well suited for characterizing rare-events that take prohibitive number of simulations in a Monte-Carlo setting. Moreover, in the new framework, delineation of the detailed causes of an observed functionality is straightforward (which involves a simple step of identifying states that are associated with the observation and analyzing these states). At the same time, our model has a high level of accuracy and detail. Compared with other analytical studies, such as the ones previously reported, a larger number of motors can be studied. In [34] and [31] the study is limited to only two motors and certain simplifying assumptions are often made (i.e. the aggregation of microstates with same energy in [34]). In [34] a stochastic model that takes into account only the number of

motors engaged on the microtubule is adopted in order to understand the level of coupling among two motor proteins carrying a common cargo. In [30] groups of more than two motor proteins are studied. Related work [28] alluded to earlier analyzes the run-length, average velocity, steady state distribution of bound motors and effects of load force on velocities. In both, the mean-field approach of [30] and the approach in [28], the proteins are not individually modeled anymore (for example, it is assumed that the load is equally shared on all the engaged motors). Under the methodology described in this paper, each motor is individually modeled and analytical or semi-analytical results can still be provided. Thus, more accurate conclusions on how the interaction between multiple-motors affects a transportation modality can be reached.

The article develops a Markov model, where the number of motors at any particular location on the microtubule lattice form states, and such a state determines the location of the common shared cargo. Here the transition probabilities between states can be derived from studies on single motor-protein based transport. The physics of the system is utilized to project the resulting infinite dimensional model onto a finite dimensional one. We show that the finite dimensional model, apart from the benefit of increased computational tractability, has other important features such as the existence of a unique steady-state probability distribution. Furthermore, we demonstrate that the probability distribution of the projected model can be used to answer most of the biologically relevant queries on transport modality. In particular, probabilities of rare events and the related mechanisms can be unraveled. The capabilities of the methodology are tested with existing data and via extensive Monte-Carlo simulations. These features can significantly ease the computational burden as well as provide unique insights into transport modalities.

3.1 Methods

Here we provide a methodology for analyzing the dynamics of an ensemble of motor proteins carrying a single cargo on a microtubule lattice. Each individual motor behavior is described stochastically: it can detach or attach to the microtubule and take steps on the filament according to prescribed probabilities that are governed by specified transition rates. The derived stochastic model provides an intuitive representation of the physical system, but, being infinite-dimensional, is not tractable and provides no general guarantees on the existence of stationary steady behavior. This impasse is overcome by building an alternative, and effective, Markov model with the advantage of being described by a *finite* number of states. In this model only the information pertinent to the relative configuration of the motor-proteins is incorporated where the relative positions of motor proteins with respect to each other determine the state. The evaluation of the probability distribution for all these possible arrangements can be determined by computing the exponential of a matrix with a dimension that is dependent on the number of arrangements. We show that the number of states does not become excessively large and that the solution via matrix exponential is viable, allowing a direct way to compute the probability distribution of motor arrangements. Furthermore we show how quantities of interest such as, average cargo run-length, average number of engaged motors and average speed of the cargo can be derived, from the determined probability distribution on the relative configurations.

We instantiate the methodology to the case where cargoes are transported by multiple kinesin motors. Despite being specific to these molecules, most of these strategies can be extended or adapted to other classes of motor proteins and also to model a cargo transported by multiple species of proteins, as well.

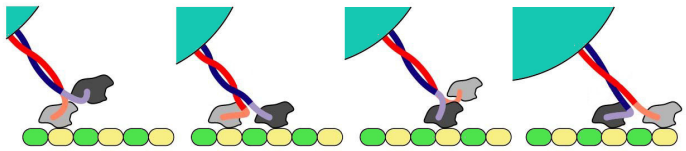

Figure 3.1: *Four stages describing the processive motion of a single molecular motor on a microtubule*

3.1.1 Description of the system and main modeling assumptions

The motion of a motor occurs by discrete steps on a microtubule. Their heads move forward by hydrolyzing ATP and producing shear forces against specific binding sites that are equally spaced (see Figure 3.1). Every motor of the ensemble is bound to the cargo molecule via a flexible linkage. We assume that the linkage has a known rest length l_0, which behaves like an elastic spring when stretched, and offers no resistance when compressed [21]. In particular, the exerted force F, as a function of its length l, is expressed as

$$F(l) = \begin{cases} k_{el}(l + l_0) & \text{if } l \leq -l_0 \\ 0 & \text{if } |l| < l_0 \\ k_{el}(l - l_0) & \text{if } l \geq l_0, \end{cases} \tag{3.1}$$

where k_{el} is the stiffness of the linkage. If the linkage is stretched beyond a certain stalling force F_s, the motor can not take any forward step. We remark that F_s is typically measured in order to quantify the number of motors that are actively pulling a cargo. Backward steps are neglected in the model and the motors are irreversibly bound to the cargo particle. A motor head that is attached to the microtubule has a certain chance of detaching from it, while a motor head that is not attached has a certain chance of binding to the microtubule. An unbound motor-protein can bind to the microtubule at a location only when it is within a distance l_0 of the cargo. Thus a floating motor

binds to the microtubule without stretching its linkage. The cargo is subjected to a constant load F_{load} that opposes the motor motion. The cargo position is described in probabilistic terms by a Gaussian distribution with variance σ_{th} and truncated on the interval $[-3\sigma_{th}, 3\sigma_{th}]$. The mean position of the cargo x_{eq} is the equilibrium position determined by the load F_{load} on the cargo and forces exerted by the motors through their linkages. The effect of thermal fluctuations is incorporated into the probabilities of cargo position by determining the variance parameter σ_{th} of the cargo position in a steady state situation. When a motor steps forward or detaches, the probability distribution of the position of the cargo is assumed to reach a new distribution with negligible transient. Thus we assume that the time scale of the cargo dynamics is much faster than the rate at which motor configurations change. The system is assumed to be spatially invariant: its stochastic behavior does not change if the motor ensemble and the cargo shift to a new position along the microtubule. Finally, if, at any time, there are no motors engaged with the microtubule, the cargo is assumed to be "lost" which forms the stopping criterion for the stochastic model.

The microtubule is modeled as a sequence of equally spaced locations $a_k = a_0 + kd_s$ where a_k represents the linear position of the k-th location, k is an integer index and d_s is the periodicity of the filament (in the case of microtubules $d_s = 8nm$). We assume that $\overline{m}$ motors constitute the ensemble. They are all permanently bound to the cargo particle while they can be engaged or not with the microtubule. We represent the locations of motors with a bi-infinite sequence of natural numbers $Z := \{z_k\}_{k\in\mathcal{I}}$ where the z_k are the number of motors engaged on the microtubule at the location a_k and $\mathcal{I}$ is the set of integer numbers. This bi-infinite sequence Z provides the *absolute configuration* of the motors on the microtubule lattice (see Figure 3.2). In the model, it is assumed that multiple proteins could share the same location on the microtubule, even though the motor proteins actually bind to physically different areas of the cargo macromolecule.

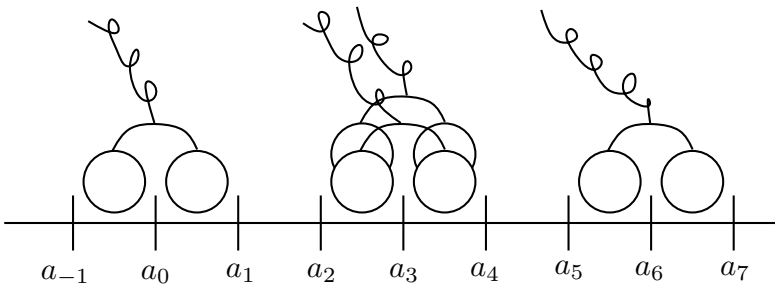

Figure 3.2: *Schematic representation of the configuration of an ensemble of motors: one motor is engaged at location a_0, two are engaged in configuration a_3 and a fourth one is engage at location a_6*

The motivation and justification for this assumption are provided later.

We denote the set of all absolute configurations as $\mathbf{Z}$. For any absolute configuration Z, we define the right-shift operator ρ that moves all the terms z_k by one place to the right. In a similar manner we define the left-shift operator ρ^{-1} and generalize the notation to ρ^{α} for a shift by α places. For a fixed value of $F_{load} > 0$, the mean cargo position x_{eq} is a function of the absolute configuration Z, that is $x_{eq} = x_{eq}(Z)$. There are only three possible transitions from one configuration Z to another Z': a motor can step forward to the next location; if attached then it can detach from the microtubule; and if unattached it can attach to the microtubule. We represent the transition from an absolute configuration Z to another absolute configuration Z' as $Z \to Z' = Z + R$, where R is a suitable sequence that characterizes the specific transition. For example, in the case of a motor at location a_k stepping forward, the transition is represented as follows

$$Z = \begin{pmatrix} \vdots \\ z_k \\ z_{k+1} \\ \vdots \end{pmatrix} \overset{STEP}{\longrightarrow} \begin{pmatrix} \vdots \\ z_k \\ z_{k+1} \\ \vdots \end{pmatrix} + \begin{pmatrix} \vdots \\ -1 \\ +1 \\ \vdots \end{pmatrix} = Z + R_k^{(step)}.$$

Analogously, for a attachment/detachment transition at location a_k, we have

$$Z = \begin{pmatrix} \vdots \\ z_k \\ z_{k+1} \\ \vdots \end{pmatrix} \overset{ATT/DET}{\longrightarrow} \begin{pmatrix} \vdots \\ z_k \\ z_{k+1} \\ \vdots \end{pmatrix} + \begin{pmatrix} \vdots \\ \pm 1 \\ 0 \\ \vdots \end{pmatrix} = Z \pm R_k^{(att)}$$

where the plus sign $(+)$ is for the attachment transition and the minus sign $(-)$ is for the detachment transition. The sequences $R_k^{(step)}$ and $R_k^{(att)}$ represent the change in number of motors from the starting configuration Z to the ending configuration Z'. Assuming that the probability rate of the transition $Z \to Z + R$ is known and is given by $\lambda_{abs}(Z + R, Z)$, it is possible to define an infinite dimensional Markov model, analogous to the ones described in [35, 36]. Here $\lambda_{abs}(Z', Z)\Delta t$ denotes the probability that the absolute configuration is Z' at time $t + \Delta t$ given that it was Z at time t. Implicit is the assumption that λ_{abs} does not depend on t. It follows that, given an initial time t_0 and an initial state $\overline{Z}$, for $t \geq t_0$, $P_{abs}(Z, t|\overline{Z}, t_0)$, the probability of the absolute configuration being equal to Z at time t given that it was equal to $\bar{Z}$ at t_0 satisfies the Master Equation

$$\frac{\partial}{\partial t} P_{abs}(Z, t|\overline{Z}, t_0) = -P_{abs}(Z, t|\overline{Z}, t_0) \sum_{Z' \in \mathbf{Z}} \lambda_{abs}(Z', Z) + \sum_{Z' \in \mathbf{Z}} \lambda_{abs}(Z, Z') P_{abs}(Z', t|\overline{Z}, t_0), \tag{3.2}$$

that represents the conservation law of the probability measure. We will drop the conditioning on the initial absolute configuration being $\bar{Z}$ at time t_0 and assume that all probabilities described below are implicitly conditioned on $(\bar{Z}, t_0)$.

We also observe that the spatial invariance hypothesis translates into an immediate condition on the transition rates, namely that $\lambda_{abs}(Z', Z) = \lambda_{abs}(\rho^\alpha Z', \rho^\alpha Z)$ for any integer α. This condition, along with the presence of a stalling force for the motors, is used to arrive at an effective finite-dimensional Markov model.

3.1.2 Derivation of an effective finite-dimensional Markov model

The representation of an ensemble of motors as a bi-infinite sequence allows one to describe the system in a rather intuitive manner and highlights the similarities with a Gillespie model for the purpose of stochastic simulations [35, 36]. However, such a model is ill-suited for an exact analysis because of its infinite dimension. A finite dimensional model can be obtained by aggregating (or projecting) states of the infinite dimensional model into "macro-states". In general, this approach leads to the loss of the Markov property. However, in the following we provide a projection of the infinite states of the original model on a finite set in such a way that the Markov property is preserved. This allows us to pursue an exact analysis and determine explicit formulas for the computation of biologically relevant quantities.

To arrive at the relative configuration description, we represent the arrangement of motors using strings of two symbols. The empty string Ø refers to the case where there are no motors engaged on the microtubule (loss of the cargo). The engaged motor that lags behind all the other motors is the "rear-guard" motor and serves as a reference. Starting with the rear-guard motor we write a symbol ('M') for a motor in each location and use a separator ('|') to distinguish distinct locations. As an example, the configuration of four motors shown in Figure 3.3(a) is represented as "$M||MM||M$" and, after the leading motor has stepped, the representation changes to "$M||MM|||M$" (see Figure 3.3(b)). This intuitive string representation provides the *relative configuration* which characterizes how various motors carrying the cargo are positioned with respect to each other.

We make the following observations:

- Strings representing relative configurations can have arbitrary length.

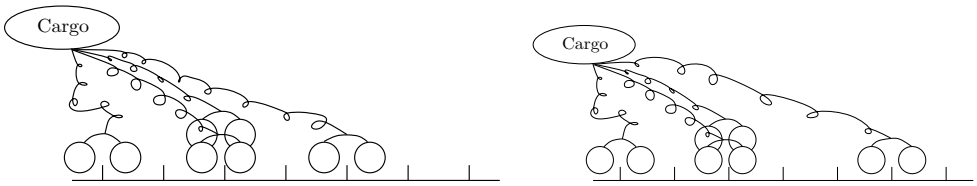

(a) (b)

Figure 3.3: *The string representation for the arrangement of four motors in (a) is "$M||MM||M$" and, after the leading motor has stepped, the representation changes into "$M||MM|||M$", as depicted in (b).*

- Two different absolute configurations of the motors, Z' and Z, on the microtubule may have the same relative configuration if Z is a "shifted version" of Z'. Two absolute configurations have the same relative configuration, if and only if the relative distances among the engaged motors of the ensemble are the same. This defines a class of equivalence on absolute configurations: two absolute configurations belong to the same equivalence class if both have the same relative configuration.

- From a relative configuration we can obtain the relative positions of the motors, but not their absolute positions on the microtubule lattice.

Consider the following assumptions on the model,

1. An ensemble contains $\overline{m}$ molecular motors (which is the number of motors attached to the cargo)

2. Motor linkages are elastic springs with constant k_{el} and rest length l_0

3. There is constant load F_{load} on the cargo

4. The stalling force is F_s

5. An unattached motor can attach to the microtubule only to locations that are within distance l_0 from the cargo center of mass (the attachment occurs a locations that are close enough not to stretch the linkage)

6. All motors are attached at the same location on the cargo and multiple motors can share the same microtubule location.

The last assumption is introduced for the following reason. From a mathematical perspective, there is no loss of generality on assuming that all molecular motors are bound to the same cargo location. Indeed it is possible to apply a coordinate change to each motor's position whereby all motors are attached at the same location on the cargo. With this assumption we have to allow for multiple motors to be attached to the same microtubule location, as, identically stretched motors that are physically attached to the cargo at different locations get mapped, in the new coordinate system, as being attached at the same location on the cargo and the microtubule.

Under the above assumptions we have established that the maximum distance (expressed in number of locations on the microtubule) between the vanguard motor and rearguard motor is bounded by

$$n := \left\lceil \max\left\{ \frac{\overline{m}F_s - F_{load}}{k_{el}d_s} + 1, \frac{F_{load}}{k_{el}d_s} \right\} + \frac{2l_0}{ds} + \frac{6\sigma_{th}}{d_s} \right\rceil \tag{3.3}$$

where $\lceil \cdot \rceil$ represents the ceiling function. The main intuition on how the various factors in (3.3) contribute follows from the stall condition on the motors, where, a motor cannot step forward if it experiences a force greater than the stall force F_s. For example, $\frac{\overline{m}F_s - F_{load}}{k_{el}d_s} + 1$ is the maximum distance between the rearguard and vanguard motor possible, beyond which motors stall, $\frac{6\sigma_{th}}{d_s}$ accounts for the thermal noise contribution, whereas, $\frac{2\ell_0}{d_s}$ accounts for the possibility that motors are within a distance $2\ell_0$ where the motors are not stretched at all.

We will establish the above result precisely when there is at least one motor opposing the motion of the cargo in the absence of thermal noise (the other cases are less involved and are based on similar arguments). Without any loss of generality, let us consider the cargo equilibrium position $x_{eq} = 0$. Let positions of the motors that assist the motion be $x_v,\ x_{v-1}, \ldots, x_1$ with $x_v \geq x_{v-1} \geq \ldots \geq x_1 \geq \ell_0$ and the corresponding forces exerted by motors be $F_v^+,\ F_{v-1}^+, \ldots,\ F_1^+$. Similarly let the positions of motors opposing the motion be given by $-y_1,\ -y_2,\ \ldots - y_r$ with $y_r \geq y_{r-1} \geq \ldots \geq y_1 \geq \ell_0 > 0$ and the corresponding forces on the cargo be $F_1^-,\ F_2^-, \ldots,\ F_r^-$ (these forces oppose the motion of the cargo). Note that $F_j^+ = k_{el}(x_j - \ell_0)$ and $F_j^- = k_{el}(y_j - \ell_0)$ and the separation S (which we term *extent*) between the vanguard and rearguard motors is $x_v + y_r$. We also note that $F_r^- = k_{el}(y_r - \ell_0) = k_{el}(y_r + x_v - x_v - \ell_0) = k_{el}S - F_v^+ - 2k_{el}\ell_0$. Under equilibrium it follows that

$$\begin{aligned} F_{load} &= F_v^+ + \textstyle\sum_{i=1}^{v-1} F_i^+ - \sum_{j=1}^{r-1} F_j^- - F_r^- \\ &= F_v^+ + \textstyle\sum_{i=1}^{v-1} F_i^+ - \sum_{j=1}^{r-1} F_j^- - k_{el}S + F_v^+ + 2k_{el}\ell_0 \end{aligned}$$

and thus

$$k_{el}S = 2F_v^+ + \textstyle\sum_{i=1}^{v-1} F_i^+ - \sum_{j=1}^{r-1} F_j^- + 2k_{el}\ell_0 - F_{load}.$$

Now suppose that the vanguard motor (and therefore all motors) is not stalled (that is $F_v^+ \leq F_s$) then it follows that

$$\begin{aligned} & k_{el}S = 2F_v^+ + \textstyle\sum_{i=1}^{v-1} F_i^+ - \sum_{j=1}^{r-1} F_j^- + 2k_l\ell_0 - F_{load} \\ & \leq 2F_v^+ + \textstyle\sum_{i=1}^{v-1} F_i^+ + 2k_{el}\ell_0 - F_{load} \\ & \leq \bar{m}F_s + 2k_{el}\ell_0 - F_{load} \end{aligned}$$

Let $s^{(max)} := \frac{\bar{m}F_s - F_{load}}{k_{el}} + 2\ell_0 + d_s$. It follows that if none of the motors are stalled then the extent $S \leq s^{(max)} - d_s$.

Now we can assert that if the extent was less than or equal to $s^{(max)}$ then for any subsequent change in the configuration, the extent will still remain less than $s^{(max)}$.

Indeed, consider the case where the current configuration is such that the extent $S \leq s^{(max)}$. There are two possibilities for the current configuration (a) the vanguard motor is stalled in which case the extent can only decrease in any subsequent change in the configuration as the vanguard motor cannot step forward and the rearguard motor cannot step backwards (b) the vanguard motor in the current configuration is not under stall in which case the extent $S \leq s^{(max)} - d_s$. In any subsequent change the only means to increase the extent is when the vanguard motor takes a step with a step-size d_s where the extent still remains bounded by $s^{(max)}$. Thus we have shown that if the extent of an absolute configuration is smaller than a bound $s^{(max)}$ then for all future configurations this bound is respected.

Using combinatorial calculus, it follows that the number N of possible relative configurations is

$$N = 1 + \sum_{m=1}^{\overline{m}} \frac{(n+m-2)!}{(n-1)!(m-1)!}. \tag{3.4}$$

Each bi-infinte sequence Z that codes the absolute configuration, determines in a unique way a string representation that codes its relative configuration, and thus transitions $Z \to Z + R$ of the infinite dimensional model determine transitions from one string representation to another. In Figure 3.4 we provide an example of a graph representing the symbolic dynamics in the case of $\overline{m} = 2$ where the maximum distance between the vanguard motor and the rearguard motor is four locations. A red-dotted arrow is used to represent a detachment transition, a green-dashed arrow represents an attachment event, and a black-solid arrow represents a forward step of one of the two motors. Notice that physically different simple events can give rise to the same transition in the symbolic dynamics of the strings. For example, from the string $M|M$ it is possible to reach the string M because of a detachment of either the vanguard or the rearguard motor. What has been achieved so far is a projection of the model dynamics from the set of

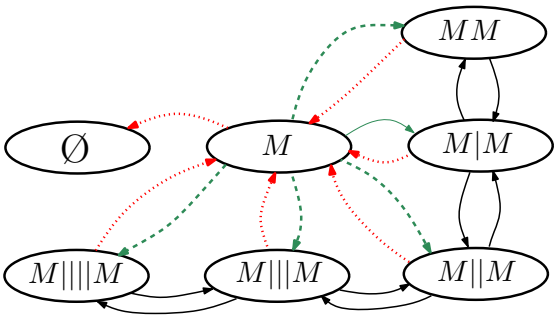

Figure 3.4: *The graph that represents the symbolic dynamics in the case of* $\overline{m} = 2$ *with the simplifying additional assumption that the two motors are never at a distance larger than four locations from each other. A red arrow represents a detachment, a green arrow represents an attachment and a black arrow represents a forward step of one of the two motors.*

absolute configurations (Z) with infinitely many elements to a space of relative configurations (σ) with finitely many configurations. We denote the projector operator as $\sigma = \Pi^{(e)}(Z)$ where the absolute configuration Z has a relative configuration σ. Also, we define the set $\mathcal{Z}(\sigma)$ of all absolute configurations with the same relative configuration σ.

$$\mathcal{Z}(\sigma) := \{Z | \Pi^{(e)}(Z) = \sigma\}$$

In general projections do not preserve the Markov property of a model. However, in this case, we can show that the dynamics on the string space still maintains the Markov property. More importantly, the transition rate $\lambda_{rel}(\sigma', \sigma)$ from one string σ to another string σ' can be meaningfully defined and can be computed from the knowledge of the rates $\lambda_{abs}(Z', Z)$ of the original Gillespie model. We now determine $\lambda_{rel}(\sigma', \sigma)$.

For small Δt, note that the probability that the absolute configuration is Z' at time $t + \Delta t$ given that it was at Z at time t is given by $P_{abs}(Z', t + \Delta t | Z, t) = \lambda_{abs}(Z', Z)\Delta t$.

Similarly, let $P_{rel}(\sigma', t+\Delta t|\sigma, t) = \lambda_{rel}(\sigma', \sigma, t)\Delta t$ denote the probability that the relative configuration is at σ' at time $t+\Delta t$ given that it was at σ at time t. We now derive the transition probabilities in the relative configuration space from the transition probabilities in the absolute configuration space. It is evident from Bayes' rule that

$$P_{rel}(\sigma', t+\Delta t|\sigma, t) = P_{rel}(\sigma', t+\Delta t, \sigma, t)/P_{rel}(\sigma(t)).$$

where $P_{rel}(\sigma', t+\Delta t, \sigma, t)$ is the probability that the relative configuration at time t is σ and is σ' at time $t+\Delta t$. $P_{rel}(\sigma', t+\Delta t, \sigma, t)$ can be obtained by summing over the probabilities $P_{abs}(K', t+\Delta t, K, t)$ of all pairs of absolute configurations K and K' that have relative configurations σ at time t and σ' at time $t+\Delta t$ respectively i.e.

$$P_{rel}(\sigma', t+\Delta t, \sigma, t) = \sum_{K\in\mathcal{Z}(\sigma)} \sum_{K'\in\mathcal{Z}(\sigma')} P_{abs}(K', t+\Delta t, K, t)$$

and similarly it follows that $P_{rel}(\sigma(t)) = \sum_{K\in\mathcal{Z}(\sigma)} P_{abs}(K, t)$. Now, arbitrarily choose Z' and Z such that $\Pi^{(e)}(Z') = \sigma'$ and $\Pi^{(e)}(Z) = \sigma$. From the translation invariance property it follows that $\mathcal{Z}(\sigma) = \{\rho^\alpha Z : \alpha \in \mathcal{I}\}$ and $\mathcal{Z}(\sigma') = \{\rho^\beta Z' : \beta \in \mathcal{I}\}$ where ρ^α denotes a shift by α positions along the microtubule and $\mathcal{I}$ denotes the set of integers. Thus, all absolute configurations with a relative configuration σ can be obtained by taking one absolute configuration Z with relative configuration σ and forming the set

of all possible shifts of the one absolute configuration Z. Thus, it follows that

$$\begin{aligned}
P_{rel}(\sigma', t+\Delta t|\sigma, t) &= P_{rel}(\sigma', t+\Delta t, \sigma, t)/P_{rel}(\sigma(t)) \\
&= \frac{\sum_{K\in\mathcal{Z}(\sigma)}\sum_{K'\in\mathcal{Z}(\sigma')} P_{abs}(K', t+\Delta t, K, t)}{\sum_{K\in\mathcal{Z}(\sigma)} P_{abs}(K,t)} \\
&= \frac{1}{\sum_\alpha P_{abs}(\rho^\alpha Z,t)} \sum_\alpha \sum_\beta P_{abs}(\rho^\beta Z', t+\Delta t, \rho^\alpha Z, t) \\
&= \frac{1}{\sum_\alpha P_{abs}(\rho^\alpha Z,t)} \sum_\alpha \sum_\beta P_{abs}(\rho^\beta Z', t+\Delta t|\rho^\alpha Z, t) P_{abs}(\rho^\alpha Z, t) \\
&= \frac{1}{\sum_\alpha P_{abs}(\rho^\alpha Z,t)} \sum_\alpha P_{abs}(\rho^\alpha Z, t) \sum_\beta P_{abs}(\rho^\beta Z', t+\Delta t|\rho^\alpha Z, t) \\
&= \frac{1}{\sum_\alpha P_{abs}(\rho^\alpha Z,t)} \sum_\alpha P_{abs}(\rho^\alpha Z, t) \sum_\beta P_{abs}(\rho^{(\beta-\alpha)} Z', t+\Delta t|Z, t) \\
&= \frac{1}{\sum_\alpha P_{abs}(\rho^\alpha Z,t)} \sum_\alpha P_{abs}(\rho^\alpha Z, t) \sum_\beta P_{abs}(\rho^\beta Z', t+\Delta t|Z, t) \\
&= \sum_\beta P_{abs}(\rho^\beta Z', t+\Delta t|Z, t) \\
&= \sum_\beta \lambda_{abs}(\rho^\beta Z', Z)\Delta t \\
&= \sum_{K'\in\mathcal{Z}(\sigma')} \lambda_{abs}(K', Z)\Delta t
\end{aligned} \tag{3.5}$$

where the first three equalities have been explained before, the fourth follows from Bayes'rule and the fifth is evident. The sixth equality uses translation invariance where the absolute configurations at t and $t+\Delta t$ are both shifted by $\rho^{-\alpha}$, the seventh follows from the fact that the set $\{\rho^{(\beta-\alpha)} : \beta \in \mathcal{I}\} = \{\rho^\beta : \beta \in \mathcal{I}\}$ where α is fixed and β is any integer (with $\mathcal{I}$ denoting the set of integers). Note that in Equation (3.5), Z was arbitrarily chosen such that $\Pi^{(e)}(Z) = \sigma$. Thus, the relation must hold for every $Z \in \mathcal{Z}(\sigma)$, yielding

$$P_{rel}(\sigma', t+\Delta t|\sigma, t) = \sum_{K'\in\mathcal{Z}(\sigma')} \lambda_{abs}(K', Z)\Delta t \qquad \text{for all } Z \in \mathcal{Z}(\sigma).$$

Thus, we can write

$$P_{rel}(\sigma', t+\Delta t|\sigma, t) = \min_{K\in\mathcal{Z}(\sigma)} \sum_{K'\in\mathcal{Z}(\sigma')} \lambda_{abs}(K', K)\Delta t$$

where the min operator has been introduced just to obtain a term that formally depends on σ and σ' only. We can define the rate of transition from the relative configuration σ

to a relative configuration σ' as $\lambda_\sigma(\sigma', \sigma)$ where $P_{rel}(\sigma', t + \Delta t|\sigma, t) = \lambda_{rel}(\sigma', \sigma)\Delta t$ with

$$\lambda_{rel}(\sigma', \sigma) := \min_{K \in \mathcal{Z}(\sigma)} \sum_{K' \in \mathcal{Z}(\sigma')} \lambda_{abs}(K', K). \tag{3.6}$$

The knowledge of the transition rates (3.6) can be exploited, using the Bayes' rule and the law of total probability, to obtain

$$\frac{\partial}{\partial t} P_{abs}(\sigma, t) = -P_{abs}(\sigma, t) \sum_{\sigma' \in \mathcal{Q}} \lambda_{abs}(\sigma', \sigma) + \sum_{\sigma' \in \mathcal{Q}} \lambda_{abs}(\sigma, \sigma') P_{abs}(\sigma', t) \tag{3.7}$$

where $\mathcal{Q}$ represents the set of all the possible N relative configurations of motor-proteins. Thus, the Master equation does hold in terms of the transition probabilities and this implies that the underlying model that governs the dynamics of relative configurations is indeed Markov.

By enumerating the strings $\sigma_1, ..., \sigma_N$ that represent relative configurations, we let $P_1(t), ..., P_N(t)$ represent the probabilities of having the system in each one of the string configurations and define, the probability vector $P(t) = (P_1(t), ..., P_N(t))^T$. Using the expressions of the transition rates $\lambda_{rel}(\sigma_j, \sigma_i)$ and Equation (3.7) it can be shown that the Markov model that describes the time dynamics of the probability vector $P(t)$ is given by

$$\frac{d}{dt} P(t) = \mathcal{A} P(t) \tag{3.8}$$

where $\mathcal{A} \in \Re^{N \times N}$ is a sparse stochastic matrix completely determined by the transition rates $\lambda_{abs}(\sigma_j, \sigma_i)$: if $i \neq j$ then $\mathcal{A}_{ji} = \lambda_{abs}(\sigma_j, \sigma_i)$, otherwise $\mathcal{A}_{ii} = 1 - \sum_{j \neq i} \lambda_{abs}(\sigma_j, \sigma_i)$. Starting from an initial probability vector $P(t_0)$, it holds that

$$P(t) = \exp(\mathcal{A}(t - t_0)) P(t_0) \tag{3.9}$$

where $\exp(\mathcal{A}t)$ is the matrix exponential. In the specific of kinesin motors, for realistic values of the system parameters and number of motors ($\overline{m} \leq 8$), the dimension of A is

in the order of $10^5 - 10^7$, making the problem of computing $\exp(\mathcal{A})$ manageable for a standard desktop computer. For more complex scenarios (i.e. multiple species of motor proteins or larger ensembles) the problem is still tractable using computer clusters or supercomputers

3.1.3 Determination of biologically relevant quantities

In the previous section, starting from an infinite dimensional model that describes the system dynamics, we have defined a finite dimensional model that keeps track of the relative distances among the motors of the ensemble. The effectiveness of this finite dimensional model is given by the fact that biologically relevant quantities of the system can be computed using explicit formulas without taking recourse to Monte Carlo simulations. Indeed, the probability distribution $P(t)$ of the different configurations provides detailed information about the system, since it provides the probability associated with every specific relative arrangement of motors on the microtubule. Once the probability of having a certain pattern of motors with all the associated relative distances is known, it is possible to determine many quantities of biological interest for the system. In the following, we provide the expressions of certain biologically relevant quantities, as obtained from our finite dimensional model. They will be considered for the validation of the methodology and in the discussion of novel results.

Average number of engaged motors

At any time t, the average of the number of engaged motors $m(t)$ is given by

$$E[m(t)] = \sum_{i=1}^{N} M(\sigma_i) P_i(t). \tag{3.10}$$

where $M(\sigma)$ represents the number of symbols 'M' in the string σ.

Average Velocity and Average Runlength

To arrive at the average run-length and average velocity, we will first determine the expected change in the cargo position in a time Δt given that the relative configuration changes from σ at time t to a relative configuration σ' at time $t + \Delta t$. This expected value can be obtained from the following steps (a) determining the change

$$d(Z', Z) = x_{eq}(Z') - x_{eq}(Z)$$

in the cargo equilibrium position for every possible transition from an initial absolute configuration Z at time t to the final absolute configuration Z' at time $t + \Delta t$, where, Z and Z' have relative configurations σ and σ'. (b) Determine, for every eligible (Z', Z) pair, the probability $P(Z', t + \Delta t, Z, t|\sigma', t + \Delta t, \sigma, t)$ of transitioning from $Z \to Z'$ conditioned on the specification that relative configuration transitions from σ to σ'. (c) Form a weighted sum of $d(Z', Z)$ with weights given by probabilities $P(Z', t + \Delta t, Z, t|\sigma', t + \Delta t, \sigma, t)$.

We first note that the change in the equilibrium position of the cargo is translation invariant. That is if the initial and the final absolute configurations are translated by the same amount then the change in the cargo position remains unaltered. Thus $d(Z', Z) = d(\rho^{\alpha} Z', \rho^{\alpha} Z)$ for any absolute configurations Z and Z'.

As in the determination of the transition rates λ_{rel}, fix two arbitrary absolute configurations Z and Z' such that $\Pi^{(e)}(Z) = \sigma$ and $\Pi^{(e)}(Z') = \sigma'$. The expected change in the cargo position when the relative initial and final configurations at t and $t + \Delta t$ are

restricted to be σ and σ' respectively is given by

$$\begin{aligned}
d_{av}(\sigma',\sigma) &:= \sum_{K'\in\mathcal{Z}(\sigma')}\sum_{K\in\mathcal{Z}(\sigma)} d(K',K)P(K',t+\Delta t,K,t|\sigma',t+\Delta t,\sigma,t)\\
&= \sum_{\alpha}\sum_{\beta} d(\rho^{\beta}Z',\rho^{\alpha}Z)P(\rho^{\beta}Z',t+\Delta t,\rho^{\alpha}Z,t|\sigma',t+\Delta t,\sigma,t)\\
&= \sum_{\alpha}\sum_{\beta} d(\rho^{\beta}Z',\rho^{\alpha}Z)\frac{P(\rho^{\beta}Z',t+\Delta t,\rho^{\alpha}Z,t,\sigma',t+\Delta t,\sigma,t)}{P_{rel}(\sigma',t+\Delta t,\sigma,t)}\\
&= \sum_{\alpha}\sum_{\beta} d(\rho^{\beta}Z',\rho^{\alpha}Z)\frac{P_{abs}(\rho^{\beta}Z',t+\Delta t,\rho^{\alpha}Z,t)}{P_{\sigma}(\sigma',t+\Delta t,\sigma,t)}\\
&= \sum_{\alpha}\sum_{\beta} d(\rho^{\beta}Z',\rho^{\alpha}Z)\frac{\lambda_{abs}(\rho^{\beta}Z',\rho^{\alpha}Z)P_{Z}(\rho^{\alpha}Z,t)}{\lambda_{rel}(\sigma',\sigma)P_{rel}(\sigma,t)}\\
&= \tfrac{1}{\lambda_{rel}(\sigma',\sigma)P_{rel}(\sigma,t)}\sum_{\alpha} P_{abs}(\rho^{\alpha}Z,t)\sum_{\beta} d(\rho^{\beta}Z',\rho^{\alpha}Z)\lambda_{abs}(\rho^{\beta}Z',\rho^{\alpha}Z)\\
&= \tfrac{1}{\lambda_{rel}(\sigma',\sigma)P_{rel}(\sigma,t)}\sum_{\alpha} P_{abs}(\rho^{\alpha}Z,t)\sum_{\beta} d(\rho^{\beta-\alpha}Z',Z)\lambda_{abs}(\rho^{\beta-\alpha}Z',Z)\\
&= \tfrac{1}{\lambda_{rel}(\sigma',\sigma)P_{rel}(\sigma,t)}\sum_{\alpha} P_{abs}(\rho^{\alpha}Z,t)\sum_{\beta} d(\rho^{\beta}Z',Z)\lambda_{abs}(\rho^{\beta}Z',Z)\\
&= \tfrac{1}{\lambda_{rel}(\sigma',\sigma)}\textstyle\sum_{\beta} d(\rho^{\beta}Z',Z)\lambda_{abs}(\rho^{\beta}Z',Z)\\
&= \tfrac{1}{\lambda_{rel}(\sigma',\sigma)}\displaystyle\sum_{K'\in\mathcal{Z}(\sigma')} d(K,Z)\lambda_{abs}(K',Z)
\end{aligned}$$

where the above equalities follow using similar arguments utilized in deriving relations in (3.5). We observe that the result is identical for all configurations Z such that $\Pi^{(e)}(Z)=\sigma$. Thus, we can write

$$d_{av}(\sigma',\sigma) = \min_{K\in\mathcal{Z}(\sigma)}\sum_{K'\in\mathcal{Z}(\sigma')} d(K,Z)\lambda_{abs}(K',K)$$

in order to obtain a right hand side that is formally a function of σ and σ' only. Once the expected value $d_{av}(\sigma',\sigma)$ of the change in cargo position in a time Δt when the transitions are restricted to have relative configuration σ at time t and σ' at $t+\Delta t$ respectively, is found, the expected change in cargo position in a time Δt can be determined via

$$\begin{aligned}
\Delta_{\Delta t} &:= \textstyle\sum_{\sigma\in\mathcal{Q}}\sum_{\sigma'\in\mathcal{Q}} d_{av}(\sigma',\sigma)P_{rel}(\sigma',t+\Delta t,\sigma,t)\\
&:= \textstyle\sum_{\sigma\in\mathcal{Q}}\sum_{\sigma'\in\mathcal{Q}} d_{av}(\sigma',\sigma)\lambda_{rel}(\sigma',\sigma)\Delta t P_{rel}(\sigma,t).
\end{aligned}$$

Thus the average velocity is found to be

$$v(t) = \Delta_{\Delta t}/\Delta t = \sum_{\sigma \in \mathcal{Q}} \sum_{\sigma' \in \mathcal{Q}} d_{av}(\sigma', \sigma) \lambda_{rel}(\sigma', \sigma) P_{rel}(\sigma, t).$$

An important quantity that can be experimentally measured in experiments is the expected run-length of the motors, that is the average length traveled by the cargo/motor complex before movement is arrested or the motor detaches from the microtubule lattice. The average run-length can be determined from the knowledge of the probability vector $P(t)$ on relative configurations. Then, the average length is given by

$$\textit{Average Runlength} = \int_0^{+\infty} v(t)dt = \int_0^{+\infty} \sum_{\sigma \in \mathcal{Q}} \sum_{\sigma' \in \mathcal{Q}} d_{av}(\sigma', \sigma) \lambda_{rel}(\sigma', \sigma) P_{rel}(\sigma, t) dt.$$

Distribution of step length

The knowledge of the probability of the relative configurations allows one to determine the distribution of the length of the steps observed in the cargo motion. Let $g(Z, l)$ be the set of all absolute configurations such that, if $Z' \in g(Z, l)$, $x_{eq}(Z') - x_{eq}(Z) = l$. Then, the probability rate $\mu^{(l,Z)}(l, Z)$ of having a step of length l given the absolute configuration Z is

$$\mu^{(l,Z)}(l, Z) = \sum_{Z' \in g(Z,l)} \lambda_{abs}(Z', Z) P_{abs}(Z, t). \tag{3.11}$$

By summing over all the shifted configurations of Z we obtain the probability rate $\mu^{(l,\sigma,t)}(l, \sigma, t)$ of having a step of length l given the relative configuration $\sigma = \Pi^{(e)}(Z)$ at

time t

$$\mu^{(l,\sigma,t)}(l,\sigma,t) = \sum_{\alpha=-\infty}^{+\infty} \sum_{Z' \in g(\rho^\alpha Z,l)} \lambda_{abs}(Z', \rho^\alpha Z) P_{abs}(\rho^\alpha Z, t) \tag{3.12}$$

$$= \sum_{\alpha=-\infty}^{+\infty} \sum_{\rho^\alpha Z' \in g(\rho^\alpha Z,l)} \lambda_{abs}(\rho^\alpha Z', \rho^\alpha Z) P_{abs}(\rho^\alpha Z, t) \tag{3.13}$$

$$= \sum_{\alpha=-\infty}^{+\infty} \sum_{Z' \in g(Z,l)} \lambda_{abs}(Z', Z) P_{abs}(\rho^\alpha Z, t) \tag{3.14}$$

$$= P_{rel}(\sigma, t) \sum_{Z' \in g(Z,l)} \lambda_{abs}(Z', Z). \tag{3.15}$$

As a consequence, summing over all the relative configurations $\sigma_1, ..., \sigma_N$ allows one to obtain the probability rate $\mu^{(l,t)}(l,t)$ of a step of length l at time t

$$\mu^{(l,t)}(l,t) = \sum_{i=1}^{N} P(\sigma_i, t) \sum_{Z' \in g(Z,l)} \lambda_{abs}(Z', Z). \tag{3.16}$$

Since the probability rate of the length of a step is proportional to its frequency, the probability $P^{(l,t)}(l,t)$ of a step of size l at time t is

$$P^{(l,t)}(l,t) = \frac{\mu^{(l,t)}(l,t)}{\sum_{x \in \chi} \mu^{(x,t)}(x,t)} \tag{3.17}$$

where $\chi = \{x : \mu^{(x,t)}(x,t) \neq 0\}$. This formula provides an exact computation of the distribution of the step size from the model parameters without relying on histograms obtained from Monte Carlo simulations.

3.2 Results and discussions

Methodology validation

While the methods developed in this article can be applied to study ensembles of motor proteins of any class, validation will be presented on kinesin motors. We first derive the transition rates λ_{abs} between absolute configurations for an ensemble of kinesin motors.

Obtaining transition rates on the absolute configuration space

The determination of transition rates are based on experimental data and theoretical considerations, where, rates from single-motor experiments are used to derive transition rates in the case where an ensemble of motors are involved in transport. Most of the modeling assumption are the same as made in [21] with minor differences which are described next.

Probability of stepping under a force F for kinesin

During a step a protein M converts ATP into kinetic energy and ADP

$$M + ATP \underset{k_{off}}{\overset{[}{}}] k_{on} \rightleftarrows M\ ATP \overset{k_{cat}}{\rightarrow} M + ADP + P_i + \texttt{energy}. \tag{3.18}$$

Following [25], Michaelis-Menten dynamics predicts a ATP hydrolysis rate equal to $k_{cat}[ATP]/([ATP] + k_m)$, where $k_m = (k_{cat} + k_{off})/k_{on}$. In addition, the free head of the motor is assumed to bind to the microtubule location with a defined probability (or efficiency) ε. In this scenario, the probability P_{step} of stepping for a single motor is given by

$$P_{step} = \frac{k_{cat}[ATP]}{[ATP] + k_m}\varepsilon. \tag{3.19}$$

The force F that the cargo exerts on the motor is assumed positive when it opposes the motor motion. When the force exceeds the stalling force F_s, it causes the motor to stall. Following [21], the force F is assumed to affect the motor dynamics by changing the probability ε of binding to the microtubule, following the relation

$$\varepsilon(F) = \begin{cases} 1 & \text{if } F \leq 0 \\ 1 - \left(\frac{F}{F_s}\right)^2 & \text{if } 0 < F < F_s \\ 0 & \text{otherwise.} \end{cases} \tag{3.20}$$

In [21] it is assumed that the force F also influences the kinetics of the ATP hydrolysis. In particular it is assumed that k_{off} increases with increasing F according to the relation

$k_{off} = k_{0off} e^{F d_l / K_b T}$, where k_{0off} is the backward reaction rate of the hydrolysis when $F = 0$, K_b is the Boltzmann constant, T is the temperature and d_l is a parameter that can be experimentally determined. Thus, the transition rate for a step under a constant force F is given by

$$P_{step}(F) = \frac{k_{cat}[ATP]}{[ATP] + \frac{k_{on} + k_{off}(F)}{k_{cat}}} \epsilon(F). \tag{3.21}$$

Under the assumption that the cargo position follows a truncated Gaussian distribution with probability density, for $|x| < 3\sigma_{th}$,

$$\phi(x) = \left(e^{-\frac{x^2}{2\sigma_{th}^2}} \right) / \left(2 \int_0^{3\sigma_{th}} e^{-\frac{x^2}{2\sigma_{th}^2}} dx \right), \tag{3.22}$$

the transition rate is determined averaging over the position of the cargo

$$\lambda_{abs}(Z, Z + R_k^{(step)}) = z_k \int_{x_{eq}(Z) - 3\sigma_{th}}^{x_{eq}(Z) + 3\sigma_{th}} P_{step}(F(x - a_k)) \phi(x - x_{eq}(Z)) dx \tag{3.23}$$

where the term z_k represents the number of motors in the k-th location (the transition rate is proportional to the number of motors in the location) and the term a_k is the position of the k-th location.

Probability of detachment

From [Schnitzer et al. 2000], the processivity L is

$$L = \frac{d_s [ATP] A e^{-F\delta_l / K_b T}}{[ATP] + B(1 + A) e^{-F\delta_l / K_b T}}, \tag{3.24}$$

where A, B and δ_l are again parameters that can be experimentally determined. Since the processivity represents how far a motor can move, on average, before detaching from the microtubule, we find a relation between the probability of stepping and the probability of detachment.

$$\frac{P_{step}(F)}{P_{detach}(F)} = \frac{L}{d_s} = \frac{[ATP] A e^{-F\delta_l / K_b T}}{[ATP] + B(1 + A) e^{-F\delta_l / K_b T}}. \tag{3.25}$$

Thus, so long as $F < F_s$,

$$P_{detach}(F) = \frac{[ATP] + B(1+A)e^{-F\delta_l/K_bT}}{[ATP]Ae^{-F\delta_l/K_bT}} P_{step}(F). \tag{3.26}$$

When $F \geq F_s$, in [21] a constant detachment rate is assumed $P_{detach}(F) = P_{back} = 2s^{-1}$. Analogously to the previous case, the transition rate associated to the detachment event is

$$\lambda_{abs}(Z, Z - R_k^{(att)}) = \tag{3.27}$$

$$z_k \int_{x_{eq}(Z)-3\sigma_{th}}^{x_{eq}(Z)+3\sigma_{th}} P_{detach}(F(x - a_k))\phi(x - x_{eq}(Z))dx. \tag{3.28}$$

Probability of attachment

Experimentally, it is found in [37, 38] that the probability of a kinesin motor attaching to the microtubule is $P_{att} \simeq 5s^{-1}$. If the motor is linked to the cargo, it is assumed that it attaches to the microtubule without stretching its linkage. Thus, the only admissible locations of attachment are the locations at a distance from the cargo that is less than l_0. They are also assumed all equally likely.

Numerical parameters

The numerical parameters that we have considered in our analysis of Kinesin-I ensembles, when not otherwise specified, are $k_{cat} = 105\ s^{-1}$, $k_{on} = 2 \cdot 10^6\ M^{-1}s^{-1}$, $k_{0off} = 55\ s^{-1}$, $[ATP] = 2 \cdot 10^{-3}\ M$, $F_s = 0.006\ nN$, $d_s = 8\ nm$, $d_l = 1.6\ nm$, $\delta_l = 1.3\ nm$, $A = 107$, $B = 0.029\ \mu M$, $T = 300K$ $k_{el} = 0.32 \cdot 10^{-3}\ nN/nm$. All these parameters are the same used in [21] and have been experimentally determined.

Using these parameters an upper-bound on $s^{(max)}$ (see Equation (3.3)) on the extent of any relative configuration is found to be $320nm$, for ensemble of at most 4 motors. This extent is rather large given that the length of a Kinesin molecule is in the hundreds of nanometer range. We remark that the $s^{(max)}$ is an upper bound on the possible extent. Thus there are avenues to be explored where a smaller extent can be assumed.

We enumerated the finite number of relative configurations as $\sigma_1, \ldots, \sigma_N$ and determined transition rates $\lambda_{rel}(\sigma_1, \sigma_2)$, from a relative configuration σ_1 to another relative configuration σ_2, using Equation (3.6).

As in [21], we have considered ensembles of at most four motors, and, we computed the probability vector $P(t)$ exactly. We remark that $P(t)$ depends on the initial probability $P(t_0)$, as shown in Equation (3.9). In all our computations for validation purposes we have assumed the same initial probability distribution $P(t_0)$ that is used in [21].

Validation of the average velocity and average run-length

Average Runlength: In [21], in one scenario (Model A) the authors neglect the effect of thermal noise, and in another scenario (Model B) they introduce a dynamic model for the Brownian motion of the cargo. We have performed the same kind of separated analysis following our approach. First, we have fixed the variance of the cargo position σ_{th} to zero, making our model analogous to "Model A" in [21].

For the initial distribution we consider that at time $t = -1$ *sec* exactly one motor is attached to the microtubule and that the cargo is not being lost before time $t = 0$. In the time interval $[-1\ sec, 0\ sec]$ the motors behave as usual. The probability distribution of their configurations at time $t = 0$ is the initial probability distribution for all our simulations. This initialization is similar to the one described in [21].

The results of this noiseless analysis are reported in Figure 3.5 using both a coarse grid (solid lines) and a fine grid (dashed lines) for the load force. The coarse grid has a resolution of 1 pN, exactly as for the run-length curves computed in [21], while for the finer grid we have chosen a resolution of 0.2 pN.

We find a practically exact quantitative agreement of our exact results and the one based on Monte Carlo simulations as presented in [21] which correspond to a coarse grid resolution of 1 pN, when there is no noise (compare Figure 3.5(a) with Figure 5(A) in

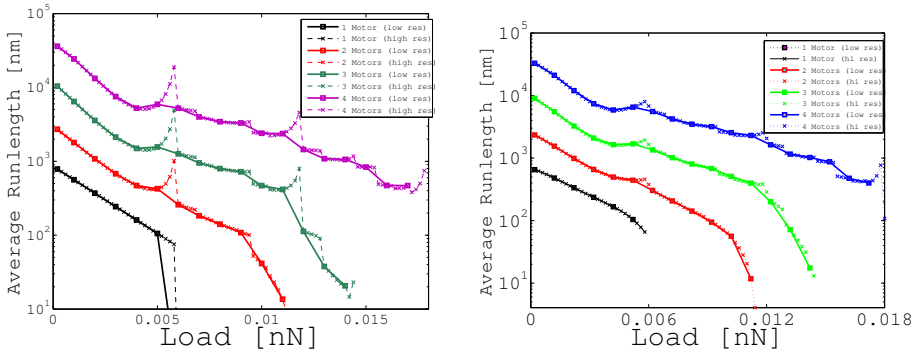

(a) (b)

Figure 3.5: Average run-length as a function of the load applied to the cargo neglecting the thermal noise component (a) and considering it (b).

[21]). In particular, for all possible sizes of the ensembles, we find run-length curves that are monotonically decreasing with higher loads. In a similar manner a near quantitative agreement is found when noise is present (compare Figure 3.5 with Figure 5(B) in [21]).

Average velocity: Under the condition that the cargo is not lost, a steady state probability distribution will be reached. The corresponding vector of probabilities Π can be used to determine the average velocity of the cargo when at least one motor is engaged on the microtubule. Results in Figure 3.6 (a) are based on the noiseless scenario equivalent to Model A in [21]. Analogous results are reported in Figure 3.6 (b) for the noisy scenario. Our results match with the results obtained in [21] using Monte Carlo simulations (see Figure 3(A) and Figure 3(B) in [21]). Indeed, one of the findings in [21] was that at low loads a cargo carried by one single motor moves faster than a cargo carried by more motors. The main difference is that the results obtained using our probabilistic method are exact and based on a precise definition of steady state. Conversely, in [21] certain approximations are required (i.e. a maximal duration for the transient is assumed) and

the accuracy depends on the number of simulations performed.

3.2.1 Discussion

The methodology developed in this article allows one to determine how the probabilities of different relative arrangements of molecular motors on a microtubule change over time. This information is contained in the probability vector $P(t)$ (see Equation 3.9). For physical values of the model, the number N of arrangements is limited and allows its direct computation. The knowledge of $P(t)$ offers, from a biological perspective, detailed information about the system. In fact, except for the absolute position of the motor ensemble on the microtubule (that is lost in the string representation), the information about the system is completely preserved. When $P(t)$ is known, it is possible to determine, via explicit formulas, many quantities of biological interest, such as the

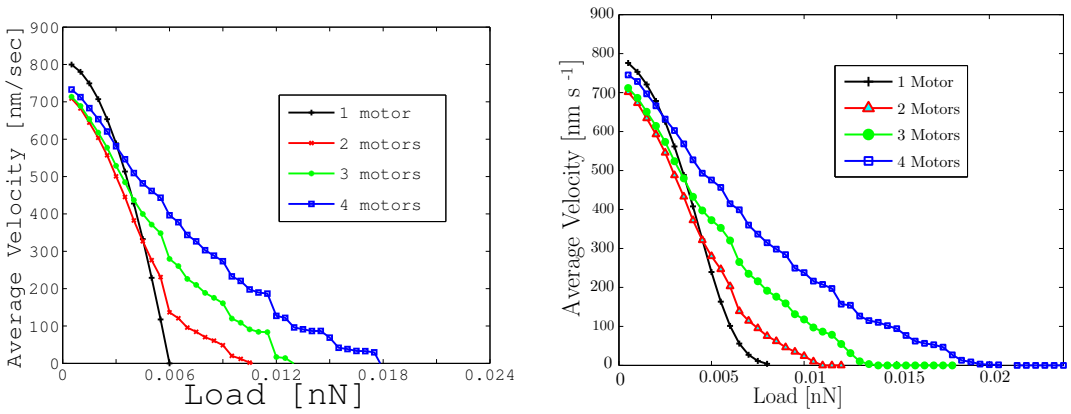

(a) (b)

Figure 3.6: Average velocity of the cargo as a function of the load in the case of ensemble of motors of different sizes (from one motor to four motors) in a case where thermal fluctuations are neglected (a) and where they are approximated with a truncated Gaussian (b).

average run-length of the ensemble, the average number of engaged or active motors, the average instantaneous velocity at which the cargo moves and the probability distribution of the step sizes observed in the cargo motion. Contrary to other methods, the final accuracy of the results does not depend on any specific simulation technique or on the number of stochastic simulations that are performed. Also, the method is extremely efficient: even for practically sized ensembles with ($\overline{m} \leq 8$), results can be computed on a standard desktop computer and general purpose software. For a large range of physically meaningful values of the parameters, the number N of possible string configurations is in the order of about $10^5 - 10^7$. Furthermore, the matrix $\mathcal{A}$, that defines the dynamics of the ordinary differential equation to be solved, is sparsely populated. The manageable dimension of the system state and the high sparsity of $\mathcal{A}$ make the computation of the exponential of $\mathcal{A}$ feasible even with a limited amount of memory. As evidence for this, all the results shown in this article have been obtained using a machine equipped with a quadcore processor and 4 Gb memory (the algorithm was implemented using MATLAB, TheMathWorks, Natick, MA). For the study of larger groups of motor proteins, the adoption of computer clusters or super-computers still remains a viable solution.

Presence of a steady state

The probability vector $P(t)$ for the different arrangements of motors of the ensemble depends on the initial probability $P(t_0)$, as shown in Equation (3.9). A fundamental question is whether starting from any arbitrary initial condition, after a transient period, the motor ensemble eventually behaves according to a fixed probability distribution which does not depend on the initial distribution of motors. A property of this kind would justify the experimentally observed robustness of the system. Furthermore, it would make it possible to determine the generality of certain observations, independent from the initial distribution $P(t_0)$.

In order to illustrate how to define a meaningful notion of steady state, it is useful to start considering how the probability distribution of the number of motors engaged on the microtubule changes over time. In Figure 3.7(a), the knowledge of $P(t)$ is used to determine the probability of having a given number of motors engaged on the microtubule at time t, assuming an ensemble of three motor proteins ($\overline{m} = 3$). The probability of having no engaged motors on the microtubule slowly converges to 1 as t goes to infinity. This corresponds to an intuitive fact: the loss of the cargo is an irreversible event for the system and, sooner or later, it is to be expected that all motors will detach from the microtubule. According to the model formulation, the loss of the cargo is always the final event and, as such, it trivially represents the only steady state condition of the system. However a non-trivial, and biologically more meaningful, notion of "steady state" can be introduced. Figure 3.7(b) shows the conditional probability distribution of the number of motors engaged on the microtubule at time t, *given that at least one motor is engaged*. This conditional probability distribution converges to a non-trivial distribution. Thus, under the assumption that the cargo has not been lost, the number of motors reaches a probability distribution that does not depend on its initial condition. This holds not only for the probability distribution of the number of engaged motors, but, more generally for the probability distribution of relative configurations, as we will show at the end of this section.

In other words, under the hypothesis that the cargo has not been lost, the relative arrangements of the motors on the microtubule reach a stable (conditional) probability distribution $\Pi \in \Re^{N-1}$. The determination of Π, once $P(t)$ is known, is quite straightforward and can be obtained directly from the definition of conditional probability. The knowledge of this steady state Π provides key insights into the behavior of a group of motors. For $\overline{m} = 3$, we have computed the steady state conditional probability Π of the motor arrangements in two different cases: cargo subject to low load

($F_{load} = 0.0002nN$) and cargo subject to high load ($F_{load} = 0.008nN$). The results are depicted in Figure 3.8(a) and in Figure 3.8(b), respectively. Data in Figure 3.8(a-b) provide the following insight. The rearguard motor is always assumed as a reference and the x-y axes represent the relative distances of the first and second motors of the ensemble from the rearguard one. Thus, each point x-y represents an arrangement of the ensemble. On the z axis we report the probability of that specific arrangement. The probabilities of configurations with less than three motors engaged are not reported in the two figures because that would make the visualization difficult. What is important to notice is how the presence of either a low load or a high load leads to two different steady state situations. Thus under a low load the motors tend to spread out almost uniformly, instead, under a high load, a certain pattern of configurations emerge as being more likely. The most likely configurations lie along the diagonal $x = y$, with a prominent peak around the origin $x = y = 0$. This means that, under a high load, eventually it is more likely to find all the three motors clustered together (represented by the peak at the origin). The high frequency of configurations along the $x = y$ diagonal suggests that it also likely to find two close leading motors with the third one lagging behind. Observations like this would be difficult to obtain using Monte Carlo simulations. Instead, an exact computation of the probabilities allows to infer these characteristics of the motion in a comprehensive manner.

Existence and uniqueness of the conditional stationary distribution

In this section we provide the proof that there is a unique non-trivial (conditional) stationary distribution for the relative configurations $\sigma_1, ..., \sigma_N$ under the assumption that there is at least one motot attached to the microtubule. Without any loss of generality assume that $\sigma_N = \emptyset$ is the state associated with the loss of the cargo and that $\sigma_1 =' M'$ is the state associated with exactly one motor attached to the microtubule. Observe that in graph associated with this Markov system all state $\sigma_2, ..., \sigma_{N-1}$ can

reach σ_1 via a sequence of detachments. Again without any loss of generality, let us reorder the states assuming that the first N_a, $\sigma_2, ..., \sigma_{N_a}$, can be reached from σ_1 in the graph associated with the Markov model and that the states $\sigma_{N_a+1}, ..., \sigma_{N-1}$ can not be reach from σ_1. The uniqueness of the stationary distribution is equivalent to showing that there is a unique vector $(\Pi_1, ..., \Pi_{N-1})^T$ such that $\sum_{j=1}^{N-1} \Pi_j = 1$ and

$$\left(\begin{array}{cccc|ccc} A_{1,1}+A_{N,1} & A_{1,2} & \dots & A_{1,N_a} & A_{1,N_a+1} & \dots & A_{1,N-1} \\ A_{2,1} & A_{2,2} & \dots & A_{2,N_a} & A_{2,N_a+1} & \dots & A_{2,N-1} \\ \vdots & \vdots & \ddots & \vdots & \ddots & \vdots & \\ A_{N_a,1} & A_{N_a,2} & \dots & A_{N_a,N_a} & A_{N_a,N_a+1} & \dots & A_{N_a,N-1} \\ \hline 0 & 0 & \dots & 0 & A_{N_a+1,N_a+1} & \dots & A_{N_a+1,N-1} \\ \vdots & & \ddots & \vdots & \vdots & \ddots & \vdots \\ 0 & 0 & \dots & 0 & A_{N-1,N_a+1} & \dots & A_{N-1,N-1} \end{array}\right)\left(\begin{array}{c} \Pi_1 \\ \Pi_2 \\ \vdots \\ \Pi_{N_a} \\ \Pi_{N_a+1} \\ \vdots \\ \Pi_{N-1} \end{array}\right) =$$

$$= \left(\begin{array}{c|c} A^{(11)} & A^{(12)} \\ \hline 0 & A^{(22)} \end{array}\right)\left(\begin{array}{c} \Pi_1 \\ \vdots \\ \Pi_{N-1} \end{array}\right) = 0.$$

where

- each column of the matrix sums up to zero
- the upper triangular structure of the matrix derives from the particular way we have reordered the states in accessible from σ_1 and not accessible from σ_1
- the top left entry $A_{1,1} + A_{N,1}$ derives from having removed the state $\sigma_N = \emptyset$ since we are looking for the conditional distribution of the relative configurations given that the cargo has not been lost.

The bottom right block $A^{(22)}$ is such that $(A^{(22)})^{N-1}$ is a strictly diagonally dominant matrix, since it is possible to reach σ_1 from each of the states $\sigma_{N_a+1}, ..., \sigma_{N-1}$. This implies necessarily that $\Pi_{N_a+1} = \Pi_{N_a+2} = ... = \Pi_{N-1} = 0$. Instead, the top left block of the matrix is an irreducible matrix (in the associated graph each state can reach

any other one passing through σ_1) implying that the elements $\Pi_1, \Pi_2, ..., \Pi_{N_a}$ and are uniquely determined and strictly positive. Thus, there is a unique stationary conditional distribution given that at least one protein is attached to the microtubule.

Enabling finer analysis

As our method yields an exact probability distribution, it facilitates a finer analysis. For example, the dependence of the average run length on the load, under the presence and absence of thermal noise, is of interest. In [21], Monte Carlo methods yield the dependence, where the average run-length is obtained with respect to load in steps of 1 pN. With our method it is straightforward to obtain the exact values at this force resolution. However, we can obtain this dependence at a finer force resolution of 0.2 pN. Using the finer scale, we noticed peaks in the run-length curves for $\overline{m} > 2$, that are not evident at the coarse resolution of 1 pN. These peaks correspond to loads that are multiples of the stalling force F_s. These peaks, ascertained by our method provides the following insight. Let us consider the curve corresponding to $\overline{m} = 2$ for simplicity. When only one motor is engaged and F_{load} is close to (but less than) the stalling force F_s, the probability of detachment becomes small, as evident from Equation (3.26). In this condition the loss of the cargo becomes unlikely. Thus, the disengaged motor, on average, has enough time to attach back to the microtubule, catch up with the leading motor and move the cargo a little further leading to a net increase in the run-length. For $\overline{m} > 2$, equivalent arguments can be provided and the peaks on the other curves can be similarly explained. This mechanism shows how, in the absence of the Brownian motion of the cargo, the expected run-length tends to increase while the load approaches values that are multiple of the stalling force. When the Brownian motion of the cargo is taken into account (see Figure 3.5 (b)) the peaks are smoothed down, but do not

disappear, thus they represent a robust characteristic of the model. This kind of non-monotonic behavior for the computed average run-length curve can be a drawback of the detachment rate model, when F is close to F_s. In such a case, our approach can be seen to identify specific inaccuracies of the model. However, it is also possible that the finer analysis indicates a behavior that is exhibited by an ensemble of motors carrying a cargo and the deviation from a monotonic behavior are not artifacts of the model. In such a case, the finer analysis identifies a mechanism of "coordination among the motors that optimizes the average run-length in situations close to a stalling scenario. Experiments can be designed and conducted in order to determine whether this mechanism is a model artifact or if it is actually occurring in the physical system. Related but different study on the relationship of velocities and run-length is reported in [39].

Detection of rare events

The exact determination of the probability distribution of the different configurations allows for the detection of rare events quantifying their probabilities. For example, from $P(t)$ it is possible to determine the probability of the different steps sizes for an ensemble of 2 motors as represented in Figure 3.9. We notice two prominent peaks corresponding to 8 nm and 4 nm. These peaks correspond to the case where there is one active motor before and after the step and to the case where there are two active motors before and after the step, respectively. There are also different predicted step sizes close to 2 nm, 6 nm and around 4 nm. They correspond to situations where there are different number of active motors before and after the step. We also find a small probability of steps larger than 8 nm which are closer to 11 nm. Since the probability distribution of steps is exactly calculated, there must be events leading to a change in the equilibrium position of the cargo with length longer than 8 nm. This is unexpected. Indeed, since each motor can advance only by 8 nm, the cargo

equilibrium itself can advance by, at most, 8 nm. In order to identify the possible causes of these anomalous steps, we have taken into account all the possible transitions from one absolute configuration to another and we have flagged those ones producing "11 nm steps". With these exhaustive analysis, we have determined that there are situations where the cargo equilibrium can advance by more than 8 nm steps. Indeed, all these situations corresponds to cases where the rearguard motor, which is actively pulling the cargo, detaches from the microtubule. This scenario is schematically represented in Figure 3.10. Thus, these "11 nm steps" are not associated to any actual stepping event of a motor, but exclusively to detachment events of the rearguard motor. This situation is rare in a bead-assay experiment, but it is known that two motors frequently pull the shared microtubule in two opposite directions in a gliding assay experiment (see [22]). Our analysis indicates that a cargo movement with step sizes larger than 8 nm is still viable in a bead assay, though infrequent. Our approach can identify the causes for such rarer modalities of transport. Thus, steps larger that $8nm$ as those described in [22] could well be originated by a mechanism of this kind. The probability distribution of the step size for an ensemble of 3 motors is reported in Figure 3.9 where the steps longer than 8 nm (at about 11 nm, 15 nm and 20 nm) have similar interpretation.

3.3 Summary

In conclusion, a framework and model for the study of the coordinated behavior of molecular motors has been introduced. The main novelty of the approach lies in the adoption of methods of analysis that obviate the need of Monte Carlo simulations. The methodology is applied to the analysis of ensembles of Kinesin-I motors. Results that had been previously found using Monte Carlo methods are accurately reproduced, validating the methodology. More importantly, under this novel probabilistic approach new

insights about the mechanisms of action of these proteins are found, suggesting hypothesis about their behavior and driving the design and realization of new experiments. For example, a possible mechanism under which motor proteins could coordinate together in order to increase their overall processivity is identified. Furthermore, the probabilistic framework allows the determination of steady state conditions for groups of molecular motors. The model predicts that, regardless of their initial configuration, the molecular motors will reach a situation where their relative distances on the microtubule will follow the same probability distribution. This provides an explanation for the robustness of the system with respect to the fluctuations of the surrounding environment.

The advantages provided in accuracy and efficiency make it possible to detect rare events in the motor protein dynamics, that could otherwise pass undetected using standard simulation methods. In this respect, the model has allowed to provide a possible explanation for infrequent steps of length longer that $8nm$ that had been observed in bead assay experiments [22].

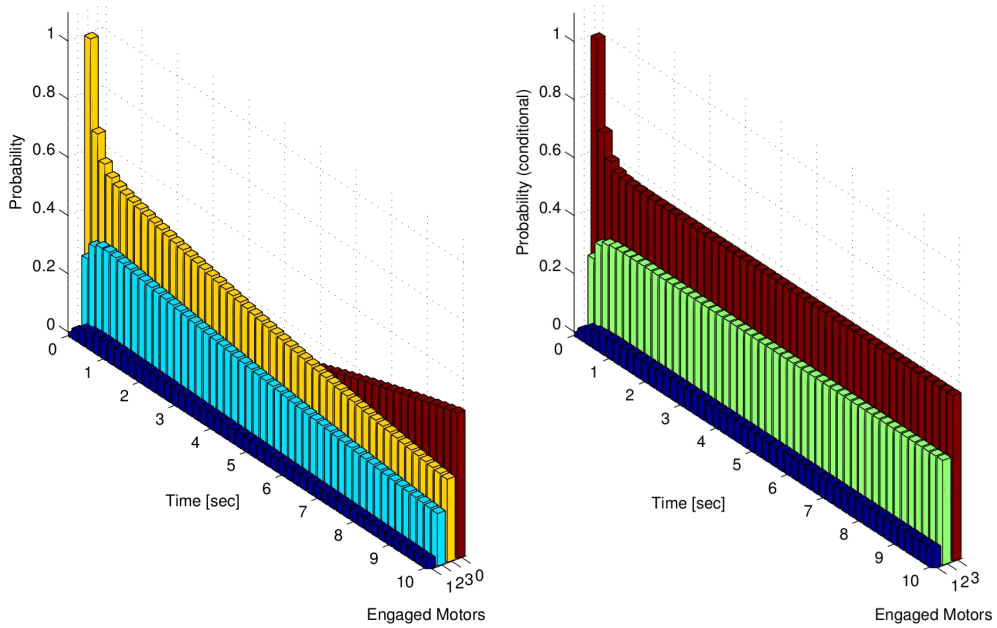

(a) (b)

Figure 3.7: Probability of having 1, 2, 3 or 0 motors engaged on the microtubule as a function of time t (a). Probability of having 1, 2, 3 motors engaged on the microtubule as a function of time t under the condition that there is at least one motor engaged (b). The probability of having no engaged motors converges to 1 as time goes to infinity. Observe, instead, that a constant probability distribution is reached in case (b) where it is assumed that at least one motor is engaged.

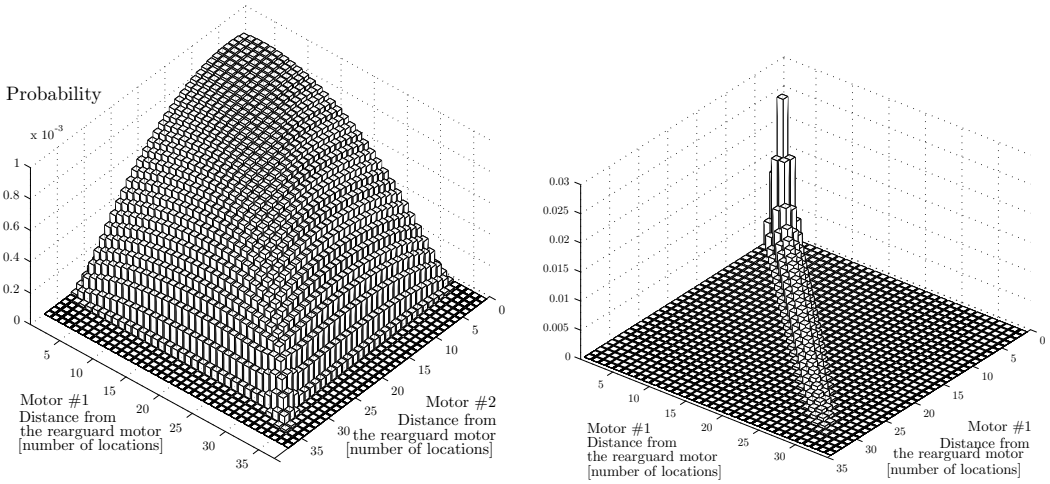

(a) (b)

Figure 3.8: A representation of the steady state probability distributions Π for an ensemble of three motors with low load (a) and high load on the cargo (b).

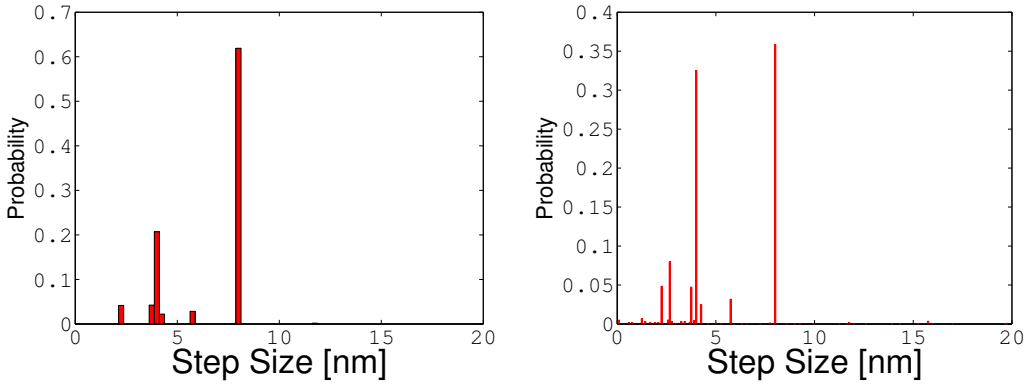

(a) (b)

Figure 3.9: Computed probabilities for different step sizes for an ensemble of two motors (a) and an ensemble of three motors (b).

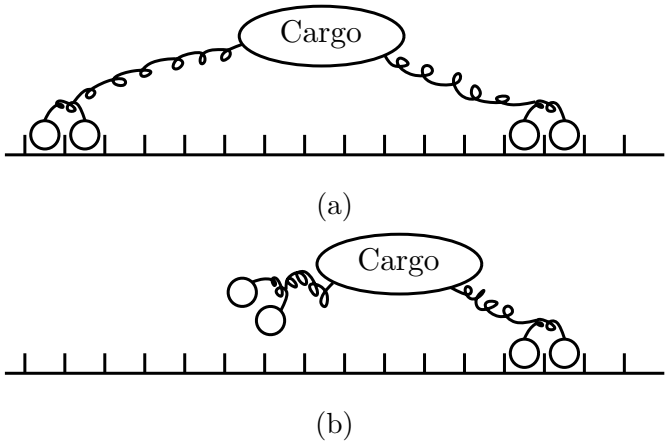

Figure 3.10: The mechanism under which steps longer than $8nm$ can be observed in the cargo motion. The rearguard motor on the left is actively pulling back the cargo (a). When it detaches from the microtubule, the cargo equilibrium position can advance by more than $8nm$ (b).

Chapter 4

Control of Transport in Brownian Rectifier mechanisms

Engineered nanoscale systems are posed to enable high efficiency and unparalleled precision in specificity in fabrication and manufacturing of materials and structures. Such a capability can result in new materials and devices with a vast range of applications in diverse areas such as medicine, electronics, and bio-materials [40, 41, 42, 43, 44]. The success of such a paradigm critically rests on the quality of transport of micro/nanoscale components from sources to destinations. An associated goal is the differentiation of components into separate groups based on different properties. Key insights on engineering transport mechanisms can be obtained from how biology utilizes micro/nano scale objects to achieve macro scale functionality. For example, in eucaryotic cells, material is transported on microtubular networks by motor proteins (kinesin and dynein) [45, 46]; a detailed understanding of the underlying transport mechanisms can play a significant role in realizing productive engineered transport systems at the molecular scale. Use of biological constructs to realize such systems has found recent focus [47, 48, 49]. However, considerable challenges remain on both the fundamental understanding of

transport mechanisms at the molecular scale and related engineering tasks.

A significant challenge for realizing efficient transport at the nano/molecular scale is posed by noise. Unlike in macroscale systems, *thermal noise* that causes Brownian motion often determines the limits of performance of molecular scale systems. For example, a kinesin motor protein (which together with dynein carry cargo inside a cell) moves on microtubules (MTs) with a characteristic step length of 8 nm; the motion caused by thermal noise has similar magnitude of standard deviations and thus a kinesin molecule has to achieve robust transport under a significant source of noise.

Remarkably, there are mechanisms that take advantage of Brownian motion to achieve directed motion. In the presence of Brownian motion, *Brownian ratchet* mechanisms use spatially periodic potential that are alternately turned on and off, to realize transport in preferred directions. For achieving the preferential bias in the motion, it is essential that the potential be asymmetric within the period; similar to the potential in a ratchet-and-pawl mechanism [50]. Moreover, in *Brownian ratchet* mechanisms, without the Brownian motion, no mean movement of particles is possible [40, 51]; thus here Brownian motion is indeed an enabling factor. In many naturally occurring systems the potential is realized only at the vicinity of the moving entity, thus being more efficient [52].

In many engineered realizations where noise is marshaled for enabling motion in a desired direction, a spatially periodic potential is realized over the whole extent of the transport regime. The resulting mechanisms are also used to separate different constituents of a mixture by exploiting the dependence of diffusion constants on physical properties (such as size) which results in different transport velocities. A flashing ratchet potential can also be realized, for example, using periodically asymmetric and transversely interleaved geometric patterns etched on surfaces and using electric fields in the transverse direction of motion (see geometric ratchets in [41, 44]). In many applications

only open-loop strategies are viable; for example, in geometric ratchets, the patterns are fixed and cannot be altered in real-time. Also, open-loop strategies have significant relevance when transport of many dispersed particles is involved. In open loop strategies a key design issue is to determine the on-and-off time schedule for the potential which optimizes transport efficiency and time to destination. Results in this article enable determination of optimal open-loop schedules that yield maximum efficiency/velocity for a given physical system without resorting to exhaustive Monte Carlo methods. In particular, the *stalling force* that prohibits appreciable forward transport, schedules that severely limit forward transport and schedules that result in non-negligible forward transport are determined. The viable range of on-off schedules are used to obtain bounds on forward and backward transport that can occur in a single on-off cycle, which are used to obtain an analytical estimate of the probability density function of the particle position. Error bounds on the estimated pdf of the position from the true pdf are obtained. The analysis and results above provide critical guidance in the design of ratchet mechanisms, which will lead to better transport mechanisms in applications, for example, in colloidal self-assembly [41, 44] and separation of mixtures [40].

Closed-loop strategies hold significant promise of increasing transport efficiency in Brownian ratchet based mechansms. As alluded to earlier, motor-proteins, such as kinesin and dynein carry cargo inside a cell over MT networks (see Figure 4.1). Each MT is formed by dimer units, which can be modeled as dipoles. Motor-proteins acquire ATP and ADP molecules that have different charge densities and thus by conversion between these molecules (via hydrolysis) the effective interaction potential between the motor complex and the microtubule is changed. The electrostatic force felt by the motor depends on where the ATP/ADP molecule is in relation to the dimer unit, providing a natural feedback mechanism; and thermal forcing provides the noise component. Thus all the ingredients that constitute a Brownian ratchet, with feedback, are present in the

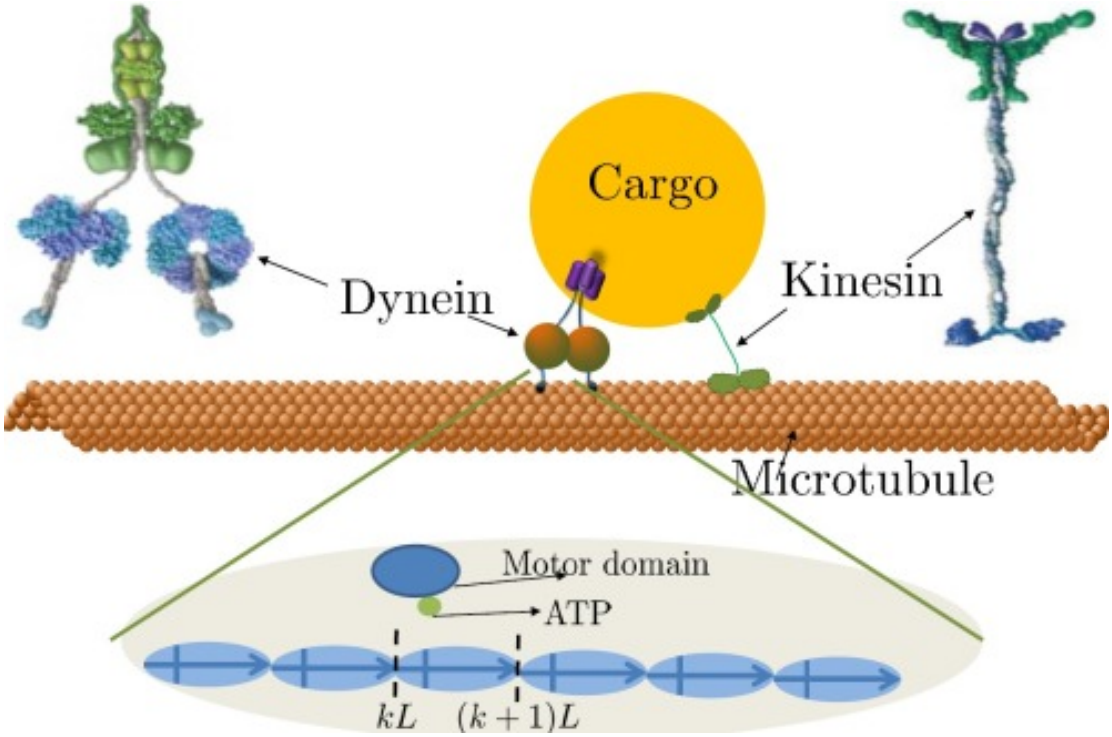

Figure 4.1: The top schematic shows the transport of a cargo by motor proteins Kinesin and Dynein that *walk* on linear lattice provided by microtubules (MT). A simple model of MT is a linear arrangement of dipole moments (which is shown in the bottom figure). When an ATP/ADP molecule (which has a charge) is attached to the motor domain, the motor protein will feel the electrostatic force due to the dipole moments which depends on whether an ATP or an ADP is attached. The string of dipole moments provides the periodic asymmetric potential and the acquisition and loss of ATP/ADP switches the ratchet potential. It is possible that the rate of switching between the ADP and ATP molecules is dependent on where the motor domain is with respect to the MT unit that is modeled as a dipole. It is postulated that due to conformational changes in the motor protein structure, ATP/ADP exchange rate is different in the first α fraction of the dipole length in comparison to the case when the motor domain is anywhere in the rest of the $1-\alpha$ fraction.

molecular motor based transport[53, 54]. Engineered systems can be synthesized and used to study the effect of feedback mechanisms that govern changes in the potential. These studies can be used to develop *efficient* feedback strategies in the transport of a single particle. Although closed-loop strategies are considered in the literature, most focus on maximizing velocity of transport (for example, [55]) and do not consider efficiency ([56] does emphasize importance of transport efficiency). In this article, the trade-off between the average velocity of the particle and the energy required are obtained by solving a multiobjective stochastic optimization problem. It is shown that optimal feedback control strategies can be obtained using a dynamic programming formulation in a tractable manner. Similar approach have been adopted for a flashing ratchet system in [57], although the objective there was limited to maximization of velocity under certain conditions. A key insight obtained is that optimizing average velocity may compromise efficiency. For a given set of physical parameters the study provides guidelines on the choice of velocities to target maximum efficiency. Apart from providing guidance on engineered systems, the study of feedback mechanisms will enable the study of molecular motors, where analytical results can be used to decipher experimental data to assess whether feedback is essential (or the extent to which feedback is needed) to explain the data. Since often for many particle systems, the objectives are cast in terms of the center of mass of the particle positions [56, 58], efficient single-particle feedback strategies can prove helpful when applied to a virtual particle at the center of mass of the particle ensemble. The closed-loop performance also provides bound on the limits-of-performance of many particle systems[59].

4.1 Mathematical Modeling

Brownian rectifiers constitute a class of mechanisms that realize transport in a preferential direction via 'rectification' of thermal noise. To understand how a Brownian ratchet

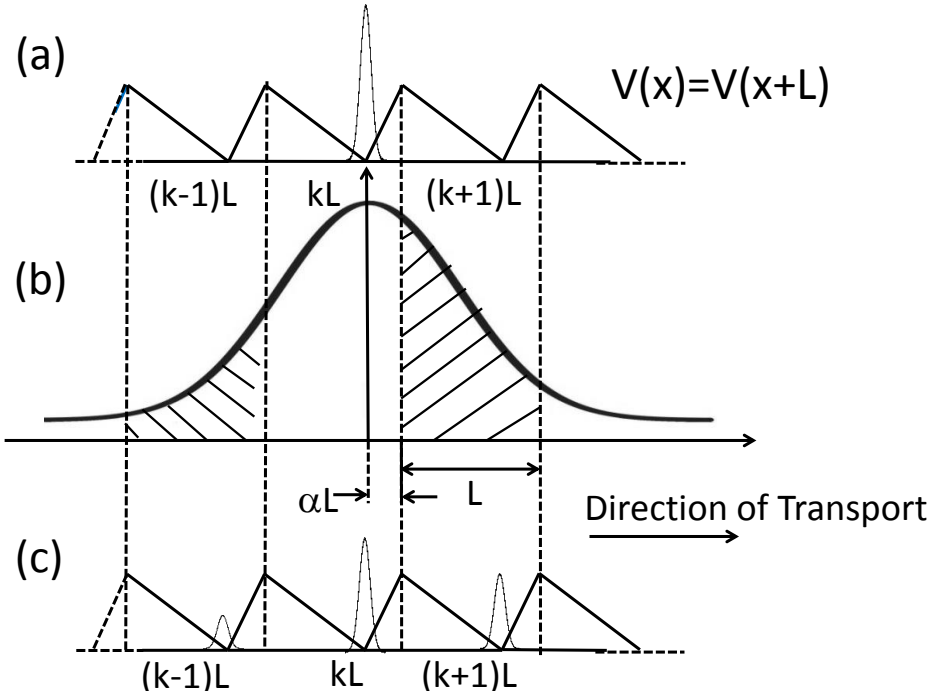

Figure 4.2: (a) describes a periodic potential with spatial period L. (b) shows a Gaussian pdf with mean kL and variance t_{off}. Consider a particle which initially at time $t = 0$ is at the well $x = kL$. The corresponding pdf at time $t = 0$ is shown in (a). The potential is absent for time $[0, t_{off}]$. The probability of finding the particle in the region $x > (k + \alpha)L$ is much higher than finding the particle in the region $x < (k - 1 + \alpha L)L$ after a time t_{off}. If the potential is turned on at time t_{off} probability of having the particle move in the well at $(k + 1)L$ is much higher than having the particle move to the well at $(k - 1)L$ thus achieving transport to the right. (c) illustrates the evolved pdf of the particle after one flash.

rectifies noise to obtain preferential movement of particles, consider a simple version of a ratchet shaped potential (see Figure 4.2(a)) that remains on and off in an alternating manner for time intervals t_{on} and t_{off} respectively[1] . Here the potential is periodic with a period L and has positive slope (the corresponding force, $-\frac{\partial V}{\partial x}$, is negative) in the interval $(kL, (k+\alpha)L)$ and a negative slope (the corresponding force is positive) in the interval $((k-1+\alpha)L, kL)$ of the k^{th} spatial period. Consider a particle located at the k^{th} valley at time $t = 0$. We represent the dynamics of the particle in terms of the time evolution of the probability density function $p(x, t|x_0 = kL, 0)$, which is the probability of the particle being at position x at time t given that it was at $x = kL$ at time $t = 0$. Thus, $p(x, 0|kL, 0) = \delta(x - kL)$, where $\delta(x)$ is the Dirac-delta function. Suppose the potential is off in the time interval $[0, t_{off}]$; then the motion of the particle is governed by Brownian motion and the pdf is given by (see Figure 4.2(b))

$$p(x, t|kL, 0) = \frac{1}{\sqrt{4\pi Dt}} exp\left(-\frac{(x - kL)^2}{4Dt}\right). \tag{4.1}$$

Note that the mean position of the particle remains unchanged at $x = kL$, while the variance increases linearly with time t. Thus at the end of the off-time the probability of finding the particle in the region $x > (k+\alpha)L$ and $x < (k-1+\alpha)L$ are given by $I_f = \int_{(k+\alpha)L}^{\infty} p(x, t = t_{off}|kL, 0)dx$ and $I_b = \int_{-\infty}^{(k-1+\alpha)L} p(x, t = t_{off}|kL, 0)dx$ respectively. Typically α is chosen such that the length αL is smaller than the length $(1-\alpha)L$, and therefore $I_f > I_b$. Thus upon turning the potential back on, the probability of finding the particle (using (4.1)) in the region $x > (k+\alpha)L$ is greater than finding it in the region $x < (k-1+\alpha)L$. The on-time t_{on} is chosen large enough to allow the particle to settle at the bottom of the well in which it is located. With these conditions, after a duration $t_{off} + t_{on}$ the particle has a higher probability of settling in the well whose minimum is at $x = (k+1)L$ or stay at the current well (at $x = kL$) than going backwards and settling in the well corresponding to $x = (k-1)L$ (the pdf of the particle's position

[1] and hence the name 'flashing ratchet'

after the potential is turned back *on* is shown in Figure 4.2(c)). Thus on average, the particle moves to the right after many flashes. The above description provide the main principle exploited by Brownian Ratchets.

A specific potential that serves the requirement of Brownian Ratchets is shown in Figure 4.2, which can be mathematically expressed as

$$V(x) = \begin{cases} V_0 \dfrac{\mathrm{mod}(x, L)}{\alpha L} & \text{for } \mathrm{mod}(x, L) < \alpha L \\ V_0 \left(1 - \dfrac{1}{(1-\alpha)} \left(\dfrac{\mathrm{mod}(x, L)}{L} - \alpha\right)\right) & \text{for } \mathrm{mod}(x, L) \geq \alpha L. \end{cases} \tag{4.2}$$

This form of potential is easily realized experimentally (see [60, 61]). Combination of all forces opposing the motion of the particle is modeled by a constant *load force* F. In biological systems, such forces may originate from intracellular mechanism [53] or sometimes from measurement devices such as optical traps [54]. In engineered systems, the load force typically is an external force [62].

The equation of motion of a particle in a thermal bath which is under the influence of a switched potential and a load force is given by the stochastic differential equation [56, 63, 54]

$$\gamma dx = -F dt - \theta(t) V'(x) dt + \sqrt{D} dW(t), \tag{4.3}$$

where γ is the viscous coefficient of the medium, $D = \frac{K_B T}{\gamma}$ [62] is the diffusion constant and $W(t)$ is the Wiener process. Here K_B is the Boltzman's constant and T is the absolute temperature of the thermal bath. The switching parameter $\theta(t)$ is 0 when the ratchet is *off* and 1 when it is *on*.

For further analysis, we employ normalized units (n.u.) for different variables, that will make the analysis in the article applicable to a wide array of practical situations. The normalized units of different quantities are summarized in the following table. .

Length	Energy	Force	Viscous coeff.	Velocity	Time
L	$k_B T$	$\dfrac{k_B T}{L}$	γ	$\dfrac{k_B T}{\gamma L}$	$\dfrac{\gamma L^2}{k_B T}$

Note that L above is the period of the ratchet potential (see Figure 4.2).

4.2 Open Loop Performance

In this section, we derive a closed form pdf of the position of the particle under the influence of a flashing ratchet with assumptions that $V_0 \gg k_B T$ and $\alpha \ll 1$ which ensure that when the potential is on, thermal noise alone can not make a particle jump from one valley (the interval $[k\alpha L, (k+1)\alpha L]$ is referred to as the kth valley) to another and at the end of the on-time, the particle is localized at the bottom of its resident valley. From the pdf, we then derive closed form expression of the mean and the variance of the transport velocity and the efficiency of transport. We also derive the conditions under which the probability of back propagation of the particle beyond a certain valley can be neglected.

Consider a particle located initially at valley 0 (see Figure 4.3). The valleys to the left of valley 0 are numbered as $-1, -2, \ldots$. Similarly, to the right they are numbered as $1, 2, \ldots$. The probability of the particle jumping forward by i valleys in a single flash is denoted by s_i and that of jumping backward by j valleys is denoted by s_{-j}. Note that these probabilities are independent of the initial location of the particle.

Under the assumption of perfect localization at the resident valley during on-time, it follows that

$$s_i = P(il + \alpha L \leq x(t_{off}) \leq (i+1)L + \alpha L) \tag{4.4}$$

and

$$s_{-j} = P(-(j+1)L - (1-\alpha)L \leq x(t_{off}) \leq -jL - (1-\alpha)L) \tag{4.5}$$

where $P(a \leq x \leq b) = \int_a^b p(x(t_{off}), t_{off}|0,0)dx$ and in presence of load force F, $p(x(t_{off}), t_{off}|0,0)$ is given by,

$$p(x(t_{off}), t_{off}|0,0) = \frac{1}{\sqrt{4\pi D t_{off}}} exp\left(-\frac{(x - \frac{F}{\gamma}t_{off})^2}{4Dt_{off}}\right). \tag{4.6}$$

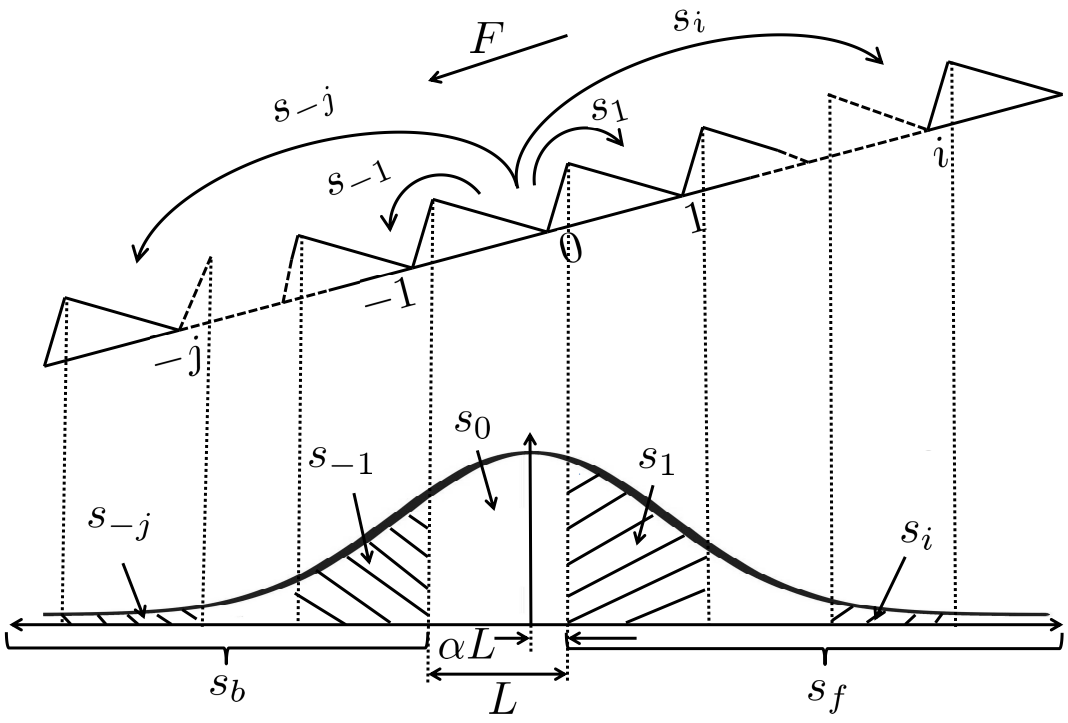

Figure 4.3: Flashing ratchet showing the numbering of valleys and different transition probabilities. The valley where the particle(s) initially reside is marked as the zeroth valley. Valleys towards its right are numbered with positive integers and to the left with negative ones. The probability of jumping forward by i valleys is denoted by s_i, whereas that of jumping backwards by j valleys is denoted by s_{-j}. s_0 denotes the probability of remaining in the initial valley, while s_f and s_b denote the total probability of transportation to the front and to the back respectively.

Here, during the on-time, the particle displacements due to diffusion are neglected.

We also define the quantities $s_b = \sum_{j=1}^{\infty} s_{-j}$ and $s_f = \sum_{i=1}^{\infty} s_i$, where s_f and s_b denote the total probability of forward and backward transportation in a single flash respectively. $s_0 = 1 - s_f - s_b$, denotes the probability of the particle remaining in the initial valley. The probability $P_k[n]$ of finding the particle in the k^{th} valley after the n^{th} flash is given by the master equation,

$$P_k[n] = P_k[n-1]s_0 + \sum_{i=1}^{\infty} P_{k+i}[n-1]s_{-i} + \sum_{i=1}^{\infty} P_{k-i}[n-1]s_i. \tag{4.7}$$

Here the first term in (4.7) is the probability that the particle remains in the k^{th} valley, the second term represents the probability of the particle coming into the k^{th} valley from valleys in front and the third term represents the probability of the particle coming into the k^{th} valley from the valleys behind in the n^{th} flash. As the problem is translation invariant we will assume that the particle is initially located at the zeroth valley; results hold for the initial location to be at any of the other valleys. Thus assuming $P_k[0] = \delta[k]$ (note that we have represented the dirac-delta function by $\delta(x)$ earlier; $\delta[k]$ represents the kronecker delta with $\delta[0] = 1$ and $\delta[k] = 0$ if $k \neq 0$) for all k, it follows that if we can determine s_i and s_{-i} for all i, then we can determine the probability distribution of the particle in space after any number of flashes by propagating (4.7).

4.2.1 Derivation of closed form pdf

In this section, we present a few results that quantify bounds on backward propagation beyond a certain valley for the load force and off-time parameters that ensure forward propagation. We derive a closed form pdf for the particle propagation which are near exact solutions to (4.7), where the bounds obtained on forward and backward propagation significantly simplify the computation.

First we derive a bound F_{stall} on the load force that severely limits forward motion.

Theorem 1 *Let* $F_{stall} := \dfrac{\gamma n^2 D}{2\alpha L}$. *If load force* $F > F_{stall}$, *then* $\sum_{i>0} s_i \leq \dfrac{1}{2}\mathrm{erfc}(\dfrac{n}{\sqrt{2}})$ *for any choice of off-time, where* $\mathrm{erfc}(x) = \dfrac{2}{\sqrt{\pi}} \int_x^\infty e^{-y^2} dy$.

Proof: Let $F > F_{stall}$. Suppose there exists some $t_{\text{off}} = t$ such that $\sum_{i>0} s_i > \dfrac{1}{2}\mathrm{erfc}(\dfrac{n}{\sqrt{2}})$, then we have $\int_{\alpha L}^\infty \dfrac{1}{\sqrt{4Dt}} e^{-\frac{(x+Ft/\gamma)^2}{4Dt}} dx > \dfrac{1}{\sqrt{\pi}} \int_{\frac{n}{\sqrt{2}}}^\infty e^{-y^2} dy$.

Defining the variables $z = \frac{x+Ft/\gamma}{\sqrt{2Dt}}$ and $w = \sqrt{2}y$ we obtain

$$\int_{\frac{\alpha L + Ft/\gamma}{\sqrt{2Dt}}}^\infty e^{-z^2/2} dz > \int_n^\infty e^{-w^2/2} dw$$

which implies $\alpha L + \dfrac{F}{\gamma} t - n\sqrt{2Dt} \leq 0$. Let $g(t) := \alpha L + \dfrac{F}{\gamma} t - n\sqrt{2Dt}$. Note that $g(0) = \alpha L > 0$. Thus to satisfy $g(t) < 0$, we must have some $\tilde{t}$ satisfying $g(\tilde{t}) = 0$. This in turn requires that the determinant of the quadratic $\tilde{t}^2 \left(\dfrac{F}{\gamma}\right)^2 + 2\tilde{t}\left(\dfrac{\alpha LF}{\gamma} - n^2 D\right) + (\alpha L)^2 = 0$ must be greater than or equal to zero. Thus $4\left(\dfrac{\alpha LF}{\gamma} - n^2 D\right)^2 - 4\left(\dfrac{\alpha LF}{\gamma}\right)^2 \geq 0$ which results in the inequality $F \leq \dfrac{\gamma n^2 D}{2\alpha L} = F_{stall}$. Thus we have a contradiction to the assumptions in the theorem statement. Hence the proof follows. ■

The theorem above provides an estimate of the *stalling force*. In physical systems, such as molecular motor based transport networks, that mimic Brownian ratchet mechanisms, ([52, 64, 62]), stalling force is defined as the minimum value of load force beyond which no forward transport occurs for any choice of on-time and off-time.

Here n is a parameter that determines the error bound of forward propagation. For example, if $n \geq 3$, $\dfrac{1}{2}\mathrm{erfc}(\dfrac{n}{\sqrt{2}}) \leq 0.00135$, which essentially is the mass contained beyond the 3σ tail of the Gaussian pdf. We can have a more general estimate of the stalling force if we want the forward propagation error to be less than the mass contained beyond the $n\sigma$ tail of the Gaussian distribution by choosing n to be any positive number.

Below we present conditions on t_{off} which limit forward motion.

Theorem 2 *Let load force $F < F_{stall}$ and off-time $t_{off} \notin (T_l, T_u)$, where*

$$T_l = \left(\frac{\sqrt{2Dn^2} - \sqrt{2Dn^2 - \frac{4\alpha LF}{\gamma}}}{2\frac{F}{\gamma}} \right)^2 \text{ and } T_u = \left(\frac{\sqrt{2Dn^2} + \sqrt{2Dn^2 - \frac{4\alpha LF}{\gamma}}}{2\frac{F}{\gamma}} \right)^2.$$

Then $\sum_{i>0} s_i \leq \frac{1}{2}\text{erfc}(\frac{n}{\sqrt{2}})$, *where* $\text{erfc}(x) = \frac{2}{\sqrt{\pi}} \int_x^\infty e^{-y^2} dy$.

Proof: Let $F < F_{stall}$ and $t_{off} = t > T_u$. If $\sum_{i>0} s_i > \frac{1}{2}\text{erfc}(\frac{n}{\sqrt{2}})$, then following the proof of Theorem 1, we have $\alpha L + \frac{F}{\gamma}t - n\sqrt{2Dt} \leq 0$. Let $\beta := \sqrt{t}$ and $f(\beta) := \frac{F}{\gamma}\beta^2 - \sqrt{2Dn^2}\beta + \alpha L$ with roots $\beta_l = \frac{\sqrt{2Dn^2} - \sqrt{2Dn^2 - \frac{4\alpha LF}{\gamma}}}{2\frac{F}{\gamma}}$ and $\beta_u = \frac{\sqrt{2Dn^2} + \sqrt{2Dn^2 - \frac{4\alpha LF}{\gamma}}}{2\frac{F}{\gamma}}$. Thus, $f(\beta) \leq 0$, which implies that $(\beta - \beta_l)(\beta - \beta_u) \leq 0$, or $\beta \in [\beta_l, \beta_u]$. It follows that $t \in [T_l, T_u]$ which is a contradiction to the assumptions of the theorem. Similarly we can arrive at a contradiction by starting with the assumption $t_{off} = t < T_l$. Hence the proof follows. ■

Definition 3 *If the condition* $\sum_{i>0} s_i > \frac{1}{2}\text{erfc}(\frac{p}{\sqrt{2}})$ *is satisfied for any* $0 < p < 3$, *then we say that the condition for* **non-negligible forward transport** *is met.*

Corollary 4 *If load force $F < F_{stall}$ and off-time $t_{off} \in (T_l, \hat{T}_{off})$, where $\hat{T}_{off} = \frac{\alpha L}{\frac{F}{\gamma}}$, then the condition for non-negligible forward transport is met.*

Proof: Note that $\hat{T}_{off} < T_u$ by the inequality $\sqrt{a-b} < \sqrt{a} + \sqrt{b}$ for $a > b > 0$, and using Theorem 2. Also, $\hat{T}_{off} > T_l$ by the inequality $\sqrt{a-b} > \sqrt{a} - \sqrt{b}$ for $a > b > 0$ and using Theorem 2. The rest of the proof follows from the proof of Theorem 2. ■

The theorem above together with the corollary gives us upper and lower bounds on off-time to ensure non-negligible forward transport. The lower bound on off-time in

Theorem 2 is explained since the probability of the particle diffusing to the next valley is small when the off time t_{off} is small. The upper bound on off-time in Theorem 2 exists since a sufficiently large t_{off} will make the the downhill drift term $\frac{F}{\gamma}t_{off}$ large enough to overwhelm the diffusion term that causes the forward transport. In either case, forward transport will be negligible. It can also be readily seen that for zero load force, we require $t_{off} > \frac{\alpha^2 L^2}{2Dp^2}$ for $0 < p < 3$ to ensure non-negligible forward transport.

Theorem 5 *If* $F \in (F_m, F_{stall})$, *where* $F_m = \dfrac{2n^2 D\gamma\alpha}{(m+1-2\alpha)^2 L}$, *and we ensure non-negligible forward transport, by* $\sum_{i>0} s_i > \dfrac{1}{2}\text{erfc}(\dfrac{p}{\sqrt{2}})$ *for* $0 \leq p < 3$, *by selecting off-time* t *such that* $t \in [T_l, \hat{T}_{off}]$, *then* $\sum_{i<-m} s_i \leq \dfrac{1}{2}\text{erfc}(\dfrac{n}{\sqrt{2}})$, *where* $\text{erfc}(x) = \dfrac{2}{\sqrt{\pi}}\displaystyle\int_x^\infty e^{-y^2}dy$.

Proof: Assume $F > F_m$ and $t \in [T_l, \hat{T}_off]$. If $\sum_{i<-m} s_i > \dfrac{1}{2}\text{erfc}(\dfrac{n}{\sqrt{2}})$, then following the same arguments as in previous theorems and using symmetry of normal distribution, we have $n\sqrt{2Dt} > (m+1-\alpha)L - \frac{F}{\gamma}t$. As $\hat{T}_{off} > t$, substituting $\hat{T}_{off}$ for t on both sides of the above inequality will give us $n\sqrt{\dfrac{2D\alpha L}{\frac{F}{\gamma}}} > (m+1-2\alpha)L$. It follows that $F < \dfrac{2n^2 D\gamma\alpha}{(m+1-2\alpha)^2 L} = F_m$ which violates our initial assumption that $F > F_m$. Hence the proof follows. ■

Theorem 5 states that if the condition of non-negligible forward transport is met, a lower bound on the value of load force would limit back propagation beyond a certain valley for all off-times that ensure non-negligible forward transport. This might seem non-intuitive at a first glance, as increasing load force is supposed to increase back propagation. The key thing to note here is, we are only interested in cases where a non-negligible forward transport takes place. A non-negligible forward transport is ensured in the form of $\hat{T}_{off}$, a maximum limit on the off-time. From Corollary 4 we can see that the maximum allowable off-time $\hat{T}_{off}$ to ensure non-negligible forward transport is a decreasing function of F. Thus, for smaller load forces, it is possible to choose a

high enough off-time and still get a non-negligible forward transport. However, as this would increase the variance $2D\hat{T}_{off}$, back propagation will also be more. For higher load forces (but smaller than F_{stall}), $\hat{T}_{off}$ being small, the distribution of particles about its mean during the off-time becomes sharper, and hence back propagation beyond a certain valley can be neglected.

Theorem 6 *Let $F \in (0, F_{stall})$ and $t_{off} < min(T_m, \hat{T}_{off})$, where*

$$T_m = \left(\frac{-\sqrt{2Dn^2} + \sqrt{2Dn^2 + \frac{4(m+1-\alpha)LF}{\gamma}}}{2\frac{F}{\gamma}} \right)^2$$

If non-negligible forward transport is ensured, that is, $\sum_{i>0} s_i > \frac{1}{2}\text{erfc}(\frac{p}{\sqrt{2}})$ for any $0 \leq p < 3$, then $\sum_{i<-m} s_i \leq \frac{1}{2}\text{erfc}(\frac{n}{\sqrt{2}})$, where $\text{erfc}(x) = \frac{2}{\sqrt{\pi}} \int_x^\infty e^{-y^2} dy$. For the case when $F = 0$, the above result holds with

$$T_m = \frac{(m+1-\alpha)L}{\sqrt{2Dn^2}}.$$

Proof: For $0 < \alpha \ll 1$, it can be shown that $T_m > T_l$ using Theorem 2. Assume $t < min(T_m, T_u)$. If $\sum_{i<-m} s_i > \frac{1}{2}\text{erfc}(\frac{n}{\sqrt{2}})$, then following the same arguments as in previous theorems and using symmetry of the normal distribution, we have $\frac{F}{\gamma}t + n\sqrt{2Dt} - (m+1-\alpha)L > 0$.

Let $\beta := \sqrt{t}$ and $g(\beta) := \frac{F}{\gamma}\beta^2 + \sqrt{2Dn^2}\beta - (m+1-\alpha)L$. Thus, $g(\beta) > 0$ implies that $(\beta - \beta_l)(\beta - \beta_u) > 0$ where $\beta_l = \frac{-\sqrt{2Dn^2} - \sqrt{2Dn^2 - \frac{4(m+1-\alpha)LF}{\gamma}}}{2\frac{F}{\gamma}}$ and $\beta_u = \frac{-\sqrt{2Dn^2} + \sqrt{2Dn^2 - \frac{4(m+1-\alpha)LF}{\gamma}}}{2\frac{F}{\gamma}}$. Thus it follows that $\beta \notin [\beta_l, \beta_u]$. Now if $\beta \leq \beta_l$ then $\beta^2 > \beta_u^2 \geq min(T_m, T_u)$, which contradicts the condition $t < min(T_m, T_u)$. Hence the proof follows. ■

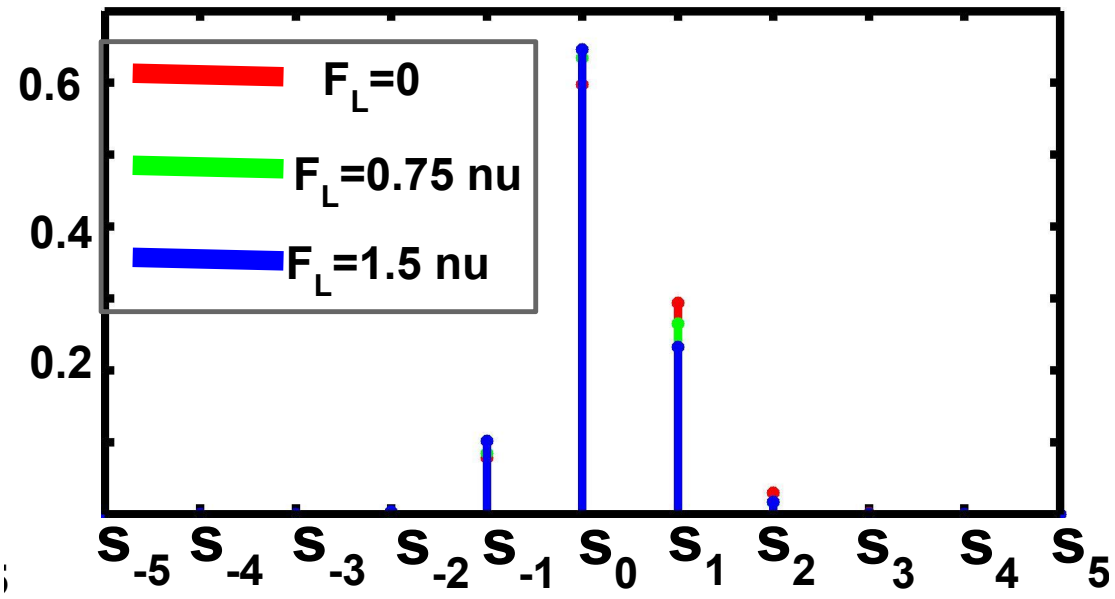

Figure 4.4: The figure shows the probability distribution of (forward and backward) jumping s_i of the particle in a single flash. s_i with i positive is the probability of jumping i valleys forward and with i negative is the probability of jumping i valleys backward in a single flash. s_i to different valleys in a single flash for different load forces All simulations are done with $V_0 = 10k_BT, L = 1, \alpha = 0.1, \gamma = 0.1$, with different load forces and off-times that satisfy the limits of Theorems 2-5. Here all variables are presented in normalized units (n.u.).

The theorem above gives us a way to limit back propagation beyond a certain valley by controlling the off-time if the condition in Theorem 5 is not met. The condition $t_{off} < min(T_m, \hat{T}_{off})$ ensures non-negligible forward transport in case $T_m > \hat{T}_{off}$.

From the results of Monte-Carlo Simulations presented in Figure 4.4, it can be seen that both forward and back propagation beyond the adjacent valley can be neglected for load forces less than the stalling force. We thus define probability of jumping one valley forward by $s_f = s_1$, probability of jumping one valley backward by $s_b = s_{-1}$ and the probability of staying in the same valley by $s_0 = 1 - s_f - s_b$. From (4.7), the propagation equation becomes

$$P_k[n] = s_0 P_k[n-1] + s_b P_{k+1}[n-1] + s_f P_{k-1}[n-1] \tag{4.8}$$

Taking $\mathfrak{Z}$ transform over space, we obtain,

$$P_z[n] = s_0 P_z[n-1] + z s_b P_z[n-1] + z^{-1} s_f P_z[n-1] \tag{4.9}$$

which implies that $P_z[n] = (s_0 + z s_b + z^{-1} s_f)^n P_z[0]$.

Now, suppose initially the particle is in the zeroth well, that is, $P_k[0] = \delta[k]$, then $P_z[0] = 1$ and

$$P_z[n] = (s_0 + z s_b + z^{-1} s_f)^n \tag{4.10}$$

By expanding the trinomial and collecting similar terms, we can write the coefficient of z^{-i} in the expansion to be $\sum_{\substack{p,q,r \geq 0 \\ p+q+r=n \\ r-q=i}} \binom{n}{p,q,r} s_0^p s_b^q s_f^r$, where $-n \leq i \leq n$.

Noting that, $\mathfrak{Z}^{-1}[z^{-i}] = \delta[k-i]$ for all $i \in \mathbb{Z}$, inverse $\mathfrak{Z}$ transform of the expansion of (4.10) results in,

$$P_k[n] = \sum_{\substack{p,q,r \geq 0 \\ p+q+r=n \\ r-q=k}} \binom{n}{p,q,r} s_0^p s_b^q s_f^r \tag{4.11}$$

where $-n \leq k \leq n$ and $\binom{n}{p,q,r} = \dfrac{n!}{p!q!r!}$.

Theorem 7 *Suppose $s_b < \epsilon$, where $\epsilon > 0$ is a small parameter. Then the probability of finding the particle in the k^{th} valley after the n^{th} flash satisfies*

$$\binom{n}{k} s^k (1-s)^{n-k} - \gamma_1 \epsilon \leq P_k[n] \leq \binom{n}{k} s^k (1-s)^{n-k} + \gamma_2 \epsilon,$$

where $s_f = s$, and γ_1 and γ_2 are positive constants.

Proof: Note that (4.11) can be rewritten as

$$\begin{aligned} P_k[n] &= \sum_{\substack{p,r\geq 0, q=0 \\ p+r=n \\ r=k}} \binom{n}{p,r,q} s_0^p s_f^r + \sum_{\substack{p,r\geq 0, q>0 \\ p+q+r=n \\ r-q=k}} \binom{n}{p,r,q} s_0^p s_f^r s_b^q \\ &= \binom{n}{n-k,k} s_0^{n-k} s_f^k + s_b \sum_{\substack{p,r\geq 0, q>0 \\ p+q+r=n \\ r-q=k}} \binom{n}{p,r,q} s_0^p s_f^r s_b^{q-1} \\ &= \tbinom{n}{k}(1-s-s_b)^{n-k} s^k + s_b M \\ &\leq \tbinom{n}{k}(1-s)^{n-k} s^k + \epsilon\gamma_2 \end{aligned}$$

where $M = \sum_{\substack{p,r\geq 0, q>0 \\ p+q+r=n \\ r-q=k}} \binom{n}{p,r,q} s_0^p s_f^r s_b^{q-1}$. Note that $\gamma_2 \leq P_k[n] \leq 1$ since γ_2 constitutes only a part the positive elements that sum to $P_k[n]$ in (4.11). This provides the upper-bound.

Now, since $M \geq 0$ (all the constituent terms of M are non-negative),

$$P_k[n] \geq \binom{n}{k}(1-s)^{n-k} \left(1 + \left(-\frac{s_b}{1-s}\right)\right)^{n-k} s^k. \tag{4.12}$$

Since $\frac{s_b}{1-s} \leq 1$ and $n-k \geq 0$, applying Bernoulli's inequality [65] to (4.12), we obtain,

$$\begin{aligned} P_k[n] &\geq \tbinom{n}{k}(1-s)^{n-k}\left(1-(n-k)\frac{s_b}{1-s}\right)s^k \\ &= \tbinom{n}{k}(1-s)^{n-k}s^k - \tbinom{n}{k}\left((n-k)\frac{s_b}{1-s}\right)s^k(1-s)^{n-k} \\ &= \tbinom{n}{k}(1-s)^{n-k}s^k - s_b Q, \end{aligned}$$

where $Q = \binom{n}{k}(n-k)s^k(1-s)^{n-k-1}$. Note that $Q \geq 0$ and bounded as $s \in [0,1]$ and $n-k \geq 0$. Thus, assuming $s_b \leq \epsilon$, we have,

$$P_k[n] \geq \binom{n}{k}(1-s)^{n-k}s^k - \gamma_2\epsilon. \tag{4.13}$$

where $\gamma_2 = Q$. This completes the proof. ■

4.2.2 Derivation of velocity and efficiency

It can be seen from Figure 4.4 that for low load forces, s_f is $3-4$ times greater than s_b. Thus, in such cases, motivated by Theorem 7 if the probability of being in the k^{th} valley after n flashes is approximated as

$$P_k[n] \approx \binom{n}{k} s^k (1-s)^{n-k}$$

then the mean position of a particle after n^{th} flash is given by $< x_n >= L\sum_{k=0}^{n} kP_k[n] = nLs$. Here $s = \frac{1}{\sqrt{4\pi D t_{off}}} \int_{\alpha L}^{\infty} exp\left(-\frac{\left(x-\frac{F}{\gamma}t_{off}\right)^2}{4Dt_{off}}\right) dx$, which evaluates to $s = 2\,\mathrm{erfc}\left(\frac{\alpha L - \frac{F}{\gamma}t_{off}}{\sqrt{4Dt_{off}}}\right)$. Therefore the average velocity is given by

$$< v_n >=< v >= \frac{nLs}{n(T_{on}+T_{off})} = \frac{Ls}{T_{on}+T_{off}}. \tag{4.14}$$

The variance Δv_n^2 in the velocity of the particle can be obtained as, $< \Delta v_n^2 >= \frac{L^2 s}{n(T_{on}+T_{off})^2}(1-s)$ where in the long time limit, we have, $< \Delta v_\infty^2 >=< \Delta v^2 >= 0$. We view efficiency η from an operational point of view (in contrast to the microscopic efficiency described in [62, 66]), *i.e.,* $\eta = \frac{P_{out}}{P_{in}}$. Let P_{out} be the average rate of work done against the load force, *i.e.,* $P_{out} = Fn_p < v_{cm} >$, where $< v_{cm} >$ is the mean transport velocity of the center of mass of n_p particles. Clearly, for one particle, $< v_{cm} >=< v >$. If e_f is the fraction of total run-time during which the ratchet was on, then $P_{in} = k_E e_f$, where k_E is a constant of proportionality. Thus for n_p particles, we have

$$\eta_{n_p} = \frac{P_{out}}{P_{in}} = \frac{Fn_p < v_{cm} >}{k_E e_f}. \tag{4.15}$$

To avoid complications arising due to the evaluation of k_E and to normalize the efficiency irrespective of the number of particles (otherwise higher number of particles may give

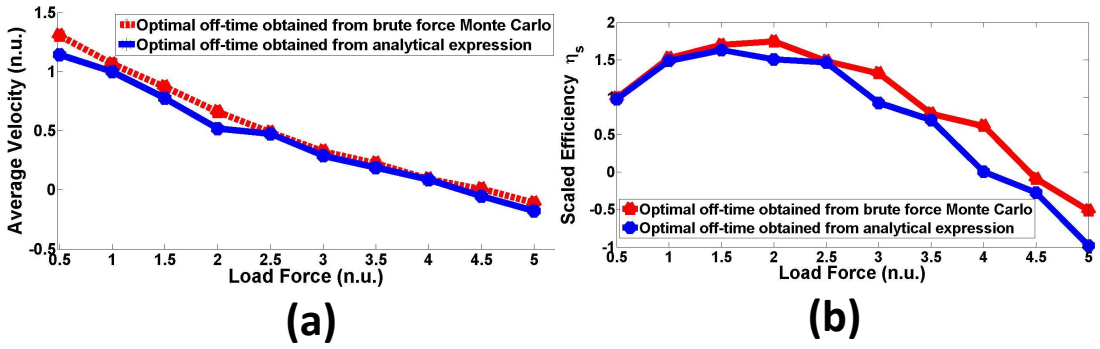

Figure 4.5: (a)Maximum velocity and (b) maximum efficiency obtained in open loop for different load forces. The off-times in the red curve are obtained by brute force Monte-Carlo simulations to find out which off-time gives maximum velocity and efficiency for different load forces. The off-times for maximum velocity and efficiency in the blue curve are obtained from the analytical expressions of velocity and efficiency. All simulations are done with $V_0 = 10k_BT, L = 1, \alpha = 0.1, \gamma = 0.1$, where all variables are presented in normalized units (n.u.).

higher efficiency for a strategy which may not truly reflect its performance), a reference efficiency η_{ref,n_p} for n_p particles is defined and all other efficiencies with the same number of particles are scaled with respect to η_{ref,n_p}. We define η_{ref,n_p} as the efficiency achieved when an average transport velocity for the center of mass of n particles is $< v_{cm} >= 1$ n.u. is achieved when the load force $F = 1$ n.u. and the input energy is k_E. Let the scaled efficiency be defined by

$$\eta_s = \frac{\eta_{n_p}}{\eta_{\text{ref},n_p}} = \frac{F_L < v_{cm} >}{e_f}, \tag{4.16}$$

where all quantities are expressed in normalized units. Clearly, η_s does not depend on the number of particles and thus is suitable for comparing the performance of different strategies.

4.2.3 Results and discussions

Note that the results in the previous section provide guidance on the design of flashing ratchet mechanisms. Theorems 1-5 establish bounds on experimental design parameters such as load force and off-time that result in non-negligible forward propagation. Furthermore, analytical expressions (4.14) and (4.15) can be used to guide the design of the Brownian ratchet mechanism to result in high average velocity and/or efficiency with Theorem 7 providing quantitative estimates on the accuracy of the analytical expressions obtained. We validate our analysis by comparing them against exhaustive Monte Carlo simulations. Figure 4.5 depicts these results for flashing ratchet with $V_0 = 10k_BT, L = 1, \alpha = 0.1$ and $\gamma = 0.1$. The maximum average velocities plotted in red in Figure 4.5(a) are obtained by running Monte Carlo simulations for 500 runs based on (4.3) for each load force F and each off-time $t_{\text{off}} \in [T_l, min(T_{m=0}, \hat{T}_{off})]$. For each load force F, the maximum average velocity (in blue) is then obtained by taking maximum among all the average velocities obtained over the set of off-times. In contrast the maximum average velocity (in red) for a given load force F is obtained by running Monte Carlo simulations for only *one* off-time t_{off}, which maximizes the expression for average velocity in (4.14). We note that there is a close agreement in the red and blue plots, which validates designing t_{off} from (4.14) in order to effect high-velocity transport.

Figure 4.5(b) shows results for maximum efficiency, analogous to the maximum velocity case, that compares results from Monte Carlo simulations run for each off-time in an interval to the simulations done for *one* t_{off} that maximizes efficiency in (4.16). Thus, if a search for optimal off-time is done over a m_p point grid of off-times and n_p point grid of load force, and Monte Carlo simulation for each off-time takes t_p seconds, then using (4.14) and (4.16) would save $m_p t_p n_p$ seconds. In the simulation results

presented, $m_p = 50$, $n_p = 10$ and $t_p \approx 50$ seconds, and thus obtaining the optimal off-time from the analytical expressions saved approximately 2.5×10^4 seconds. Also, the bounds on off-times from Theorems 1-6 helps limit the search space of off-times. The advantage of obtaining the optimal off-time that yields maximum velocity or efficiency in a systematic manner is important in cases where transport of large number of particles are involved (for example, colloidal self assembly[41, 44]).

It should be remarked that the maximum velocity and efficiency computed using (4.14,4.16) shows a similar qualitative trend (not shown in the figures) as the red and blue plots; however there is no quantitative match. The reason is that (4.14) ignores the back propagation term s_b and therefore average velocity (and hence efficiency) computed from (4.14) is higher than the case when back propagation is accounted for. However the t_{off} giving rise to maximum velocity (and efficiency) is relatively insensitive to neglecting s_b, as variation of s_b is very small around this t_{off}; thus the maximum velocity is primarily determined by the off-time that gives maximum forward transport. This is also corroborated by the results of Monte Carlo Simulations presented in Figure 4.5(a) and (b) where the optimal off-times obtained from analytical results are validated by exhaustive Monte Carlo Simulations.

4.3 Closed Loop Performance

Under a constant load force, higher efficiency can be attempted by increasing mean velocity and/or decreasing e_f (where e_f represents the fraction of the time the ratchet potential is on). However increasing $< v >$ and decreasing e_f can be opposing objectives since too low a e_f requires the potential to be off for most of the time which would impede achieving a high $< v >$. Thus design of an off-time determines a trade-off between efficiency and velocity. In view of this trade-off, we pose an optimization problem that seeks the on-off time schedule to minimize a cost function that reflects both velocity and

efficiency objectives. Before posing the optimization problem precisely, it is important to realize that the continuous time dynamics described by (4.3) will render the problem near intractable. We will now present modelling assumptions which retain the essential physics of the problem while making an optimal feedback solution determinable.

4.3.1 State update equation

We first obtain a discrete time version of the continuous time dynamics (4.3). Here we assume a finite time horizon T which is divided into N stages and that a decision whether to switch the ratchet potential on or off has to be made every $T_s = T/N$ seconds. We denote the position $x(kT_s)$ by x_k; from (4.3) we have

$$\begin{aligned} x_{k+1} &= x_k - \frac{1}{\gamma}\int_{kT_s}^{(k+1)T_s} (F_L + \theta(k)V'(x))dt + w(k) \\ &= x_k - \frac{1}{\gamma}\int_{kT_s}^{(k+1)T_s} F_L dt - \int_{kT_s}^{(k+1)T_s} \theta(k)V'(x)dt + w(k) \\ &= x_k - \frac{F_L}{\gamma}T_s - \int_{kT_s}^{(k+1)T_s} \theta(k)V'(x)dt + w(k), \end{aligned} \tag{4.17}$$

where $\theta(k) = 1$ when potential is turned on and zero otherwise, and $w(k) \sim \mathcal{N}(0, \sqrt{2DT_s})$ is a random variable capturing the effect of thermal noise. If we represent $u_k \in \{\text{on}, \text{off}\}$ to represent the control action of turning the potential on or off at kth stage, for $u_k = \text{off}$

$$x_{k+1} = x_k - \frac{F_L}{\gamma}T_s + w(k), \tag{4.18}$$

and for $u_k = \text{on}$, after neglecting the effect of thermal noise (given that $V_0 \gg k_B T$),

$$x_{k+1} = x_k - \frac{F_L}{\gamma}T_s - \frac{1}{\gamma}\int_{kT_s}^{(k+1)T_s} V'(x)dt. \tag{4.19}$$

Note that for any t such that $\text{mod}(x(t), L) < \alpha L$, the force acting on the particle is negative and $V'(x(t)) = \dfrac{V_0}{\alpha L}$. Therefore if $mod(x(kTs), L) < \alpha L$ and T_s is small

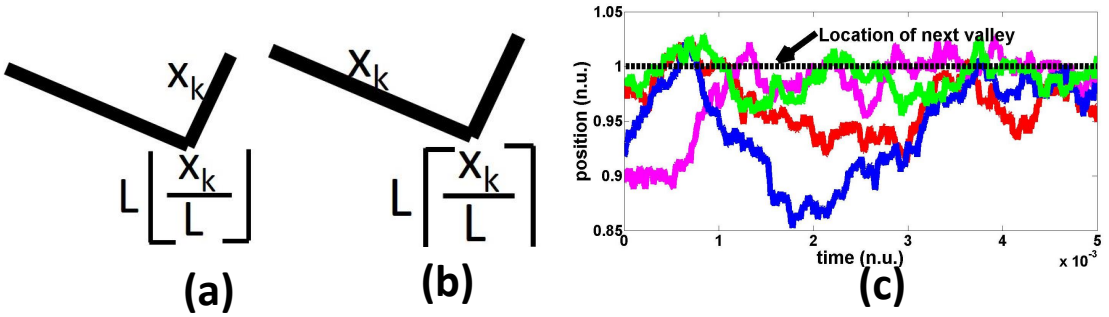

Figure 4.6: The position of x_k and the valley it localizes to with the potential on when x_k is very close to the valley and is (a) on the steeper slope (b) on the gentler slope. (c) Monte Carlo simulations confirming that the particle localizes to its nearest valley with the potential on if it is located very close to it. In the simulation $T_s = 0.5$ n.u. is used and the initial position (x_k) of the particle is on the gentler slope. The black dashed line denotes the location of the next valley.

enough such that $\text{mod}(x(kT_s) - \frac{F_L}{\gamma}T_s - \frac{V_0}{\gamma\alpha L}T_s, L) < \alpha L$ with $\frac{F_L}{\gamma}T_s + \frac{V_0}{\gamma\alpha L}T_s < \alpha L$, then under the assumptions that there are negligible transient effects due to the control action at kT_s, we have $\text{mod}(x(t), L) < \alpha L$ for all $t \in [kT_s, (k+1)T_s]$. Therefore under these conditions (4.19) simplifies to

$$x_{k+1} = x_k - \frac{F_L}{\gamma} - \frac{V_0}{\gamma\alpha L}T_s. \tag{4.20}$$

Now suppose $\text{mod}(x(kTs), L) < \alpha L$ and $\text{mod}(x(kT_s) - \frac{F_L}{\gamma}T_s - \frac{V_0}{\gamma\alpha L}T_s, L) > \alpha L$ with $\frac{F_L}{\gamma}T_s + \frac{V_0}{\gamma\alpha L}T_s < \alpha L$. Then the particle will cross the valley at $L\left\lfloor \frac{x_k}{L} \right\rfloor$. In this case we make the approximation that at the end of time T_s, the particle is settled at $L\left\lfloor \frac{x_k}{L} \right\rfloor$. This assumption is justified as subsequent to the particle crossing the valley, the ratchet potential opposes its velocity and the velocity is small due to high damping. This assumption is further justified by Monte Carlo simulations (see Fig. 4.6(c)). Therefore,

if $\text{mod}(x_k, L) < \alpha L$ and $u_k = on$,

$$x_{k+1} = \max\left(-\frac{1}{\gamma}\left(\frac{V_0}{\alpha L} + F_L\right) T_s, L\left\lfloor \frac{x_k}{L} \right\rfloor\right). \tag{4.21}$$

Similar approximations can be made for the case when $\text{mod}(x_k, L) > \alpha L$ and $u_k = \text{on}$. Thus, consolidating all the cases, we have the state update equation as,

$$x_{k+1} = \begin{cases} x_k - \dfrac{F_L}{\gamma} T_s + w_k & u_k = \text{off} \\ \max\left(x_k - \dfrac{1}{\gamma}\left(\dfrac{V_0}{\alpha L} + F_L\right) T_s, L\left\lfloor \dfrac{x_k}{L} \right\rfloor\right) & u_k = \text{on and } \text{mod}(x_k, L) < \alpha L \\ \min\left(x_k + \dfrac{1}{\gamma}\left(\dfrac{V_0}{1 - \alpha L} - F_L\right) T_s, L\left\lceil \dfrac{x_k}{L} \right\rceil\right) & u_k = \text{on and } \text{mod}(x_k, L) \geq \alpha L. \end{cases} \tag{4.22}$$

The above model was reached under a series of assumptions which render the dynamics tractable.

4.3.2 Problem statement and cost assignment

We now pose the optimization problem. Here we do not restrict the on-off time schedule to be periodic; more importantly we assume that the realized *past* trajectory of the position of the particle is measured and available for determining whether to turn on or off the potential at the current time of interest. At every time instant k, the optimization problem seeks a control action $u_k \in U = \{\text{on}, \text{off}\}$, where the past positions $\{x_j\},\ j \leq k-1$ of the particle are known, that minimizes a weighted sum of input energy $\sum_{i=k}^{N-1} e_i$ to go and deviation of the *average velocity* v from v_d where $v = x_N/T$ with x_N being the final position reached when the time horizon T is reached. Here $e(k) = e$ if the potential is on at the k^{th} instant and zero otherwise. Consider the problem of minimizing a cost function of the form

$$c_v|v_d - v| + c_e \sum_{i=k}^{N-1} e_i. \tag{4.23}$$

Note that a higher value of c_v/c_e emphasizes the objective of achieving the desired velocity v_d at the expense of increasing the input energy. The above objective leads to the following optimization problem

$$\underset{u_0,\ldots,u_{N-1}}{\arg\min} \underset{w_0,\ldots,w_{N-1}}{E} \left[c_v|v_d - v| + c_e \sum_{i=k}^{N-1} e_i \right]. \tag{4.24}$$

Here, $(w_k)_{k=0}^{N-1}$ captures the effect of thermal noise at different sampling instants and thus we minimize the expected value of the cost. We cast problem (4.24) into a dynamic programming problem. Let the cost function $g_k(s_k, u_k, w_k)$ for stage k be,

$$g_k(x_k, u_k, w_k) = \begin{cases} c_e e & \text{for } u_k = \text{ On and } k < N \\ 0 & \text{for } u_k = \text{ Off and } k < N \\ \dfrac{1}{T} c_v |x_d - x_N| & \text{for } k = N, \end{cases} \tag{4.25}$$

where $x_d = v_d T$, $x_N = vT$, and $g_N(x_N)$ is the terminal cost. Thus for a initial state x_0 and a particular sequence of actions $\pi = (u_k)_{k=0}^{N-1}$, the cost of a realization with the noise sequence $(w_k)_{k=0}^{N-1}$ is

$$J_0(x_0) = g_N(x_N) + \sum_{i=0}^{N-1} g_i(x_i, u_i, w_i). \tag{4.26}$$

To achieve objective (4.24), the sequence $\pi^* = (u_k)_{k=0}^{N-1}$ that minimizes the expectation of $J_0(x_0)$ over all possible realizations of the disturbance sequence $(w_k)_{k=0}^{N-1}$ needs to be determined. Thus the following optimization problem is of interest:

$$\begin{aligned} \pi^* &= \arg\min_{\pi} \underset{w_0,\ldots,w_{N-1}}{E} \left[J_0(x_0) \right] \\ &= \arg\min_{\pi} \underset{w_0,\ldots,w_{N-1}}{E} \left[g_N(x_N) + \sum_{i=0}^{N-1} g_i(x_i, u_i, w_i) \right]. \\ &= \arg\min_{\pi} \underset{w_0,\ldots,w_{N-1}}{E} \left[c_v|v_d - v| + c_e \sum_{i=0}^{N-1} e_i \right]. \end{aligned} \tag{4.27}$$

We now analyze the dynamic programming approach [67] and the associated computational complexity to evaluate the feasibility of the method. To find a solution to the

problem posed in (4.27), we define the cost to go $J_k^*(x_k)$ for stage k as

$$J_k^*(x_k) = \min_{u_k,\ldots,u_{N-1}} \underset{w_k,\ldots,w_{N-1}}{E} [g_N(x_N) + \sum_{i=k}^{N-1} g_i(x_i, u_i, w_i)] \tag{4.28}$$

with $J_N^*(x_N) = g_N(x_N) = \frac{1}{T} c_v |x_d - x_N|$. It can be proved that [67],

$$J_k^*(x_k) = \min_{u_k \in U} \underset{w_k}{E} [g_k(x_k, u_k, w_k) + J_{k+1}^*(x_{k+1})]. \tag{4.29}$$

Thus propagating the recursion relation in (4.29) backwards, given $J_{k+1}^*(x_{k+1})$, we determine $J_k^*(x_k)$ for every feasible x_k using (4.22) and (4.25). This way, when we finally have $J_0^*(x_0)$, we obtain our solution π^* for optimization problem in (4.27).

4.3.3 Analysis of computational complexity

We now provide an analysis for the computational cost. Since x_k is a real variable, the problem of computing u_k over the entire range of x_k for every stage ($1 \leq k \leq N-1$) is infinite dimensional. We avoid the problem of infinite dimensionality by restricting x_k to lie in a bounded set where the particle dynamics constrains the probability of x_k being outside this set to be low. Note that by using the fact that w_k follows a normal distribution with variance σ^2 in particle dynamics given in (22), we can obtain bounds d_B and d_F such that $P(d_B \leq x_{k+1} - x_k < d_F) < \eta$ for any given η (also from (22) these bounds are independent of k). More specifically for $\eta = 0.95$ (that is, 95% confidence), the bounds on forward and backward travels are given by $d_F = (\frac{V_0}{\gamma(1-\alpha)L} - \frac{F_L}{\gamma})T_s + 2\sigma$ and $d_B = -(\frac{V_0}{\gamma\alpha L} + \frac{F_L}{\gamma})T_s - 2\sigma$, respectively. Thus for the stage k, $x_k \in I_k = [kd_B, kd_F]$. Also, we grid x_k with a finite resolution $\Delta = \frac{(d_F + d_B)}{m}$, where m is a suitably chosen integer to control the resolution Δ. The steps above result in computing J_k^* only at a finite number of values of x_k.

For the k^{th} stage, we need to determine $J_k^*(x_k)$ at all the km grid values of x_k. For a given x_k, two computations need to be performed to solve (4.29) corresponding to two

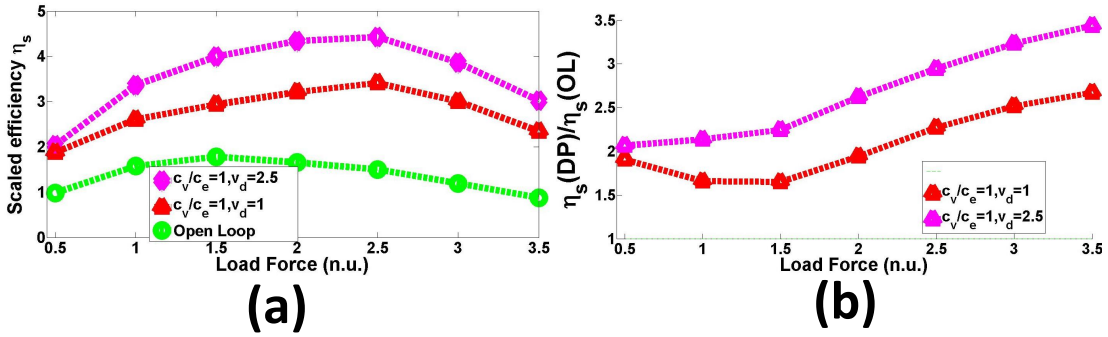

Figure 4.7: Comparison of efficiency achieved at different load forces for open loop and dynamic programming. (a) shows the actual efficiencies achieved for different strategies while (b) shows the ratio of efficiency achieved of open loop strategy and dynamic programming for different optimization parameters. In (a), the green curve corresponds to open loop, red curve corresponds to dynamic programming with $c_v/c_e = 1, v_d = 1$ and magenta curve corresponds to dynamic programming with $c_v/c_e = 1, v_d = 2.5$. In (b), the red curve corresponds to the ratio $\frac{\eta_s(DP)}{\eta_s(OL)}$ with $c_v/c_e = 1, v_d = 1$ for dynamic programming and the magenta curve corresponds to $\frac{\eta_s(DP)}{\eta_s(OL)}$ with $c_v/c_e = 1, v_d = 2.5$ for dynamic programming.

actions of $u_k =$ on and $u_k =$ off and the one yielding the lower cost is chosen. There are thus $2km$ computations to be performed in evaluating (4.29) for the k^{th} stage. However, as all these computations can be done independent of each other, if we have p processing units, each processing unit can perform $\frac{2km}{p}$ computations for the k^{th} stage. The total number of evaluations for all the stages becomes $2\sum_{k=1}^{N} \frac{km}{p} = m\frac{N(N+1)}{p}$. For modern supercomputing clusters, p and N are of the same order of magnitude and thus the computational complexity scales as N for practical conditions and hence is tractable.

4.3.4 Results

In this section we present the results from Monte Carlo simulations using closed-loop dynamic programming to compare its performance with open-loop approach and 'maximization of velocity' (MIV) protocol [56]. We used the same physical parameters as described in Sec. 4.2.3 for the open-loop approach. From Fig. 4.5 we can see that in open-loop method the maximum velocity achieved at $F_L = 3.5$ n.u. approaches zero, and thus $F_L = 3.5$n.u. can be taken as a practical estimate of stalling force F_{stall}. Real systems are typically operated much below stalling force and hence we evaluate the performances of our strategy till F_{stall} to demonstrate its effectiveness in real scenarios.

Fig. 4.7 (a) and (b) show the comparison of the open-loop and closed-loop strategies. Note that using closed-loop strategy, we can double the efficiency at low load forces while increase the efficiency more than three folds near stalling force conditions. A reason for this gain in performance is that the velocity achieved in the closed-loop, near open-loop stalling force is much greater than the open-loop strategy based velocity. It can also be seen that choosing a higher value of v_d yields better efficiency, specially at high load forces.

Fig. 4.8(a) and (b) compares the the efficiency achieved by the MIV strategy vs that of the dynamic programming (DP) based closed-loop strategy. We can see that for low load forces DP yields approximately 35% improvement over the MIV strategy, but the effectiveness of DP decreases when load forces are increased; for high load forces, MIV outperforms DP. This may seem contradictory as DP is supposed to be optimal. However, errors introduced by finite spatial gridding and assumption of perfect localization at nearest valleys become higher for higher load forces (discussed in detail in the next section). It should also be noted that DP outperforms MIV for all load forces less than $\frac{F_{stall}}{2}$ which may be considered as a practical range for most realizations of Brownian ratchets.

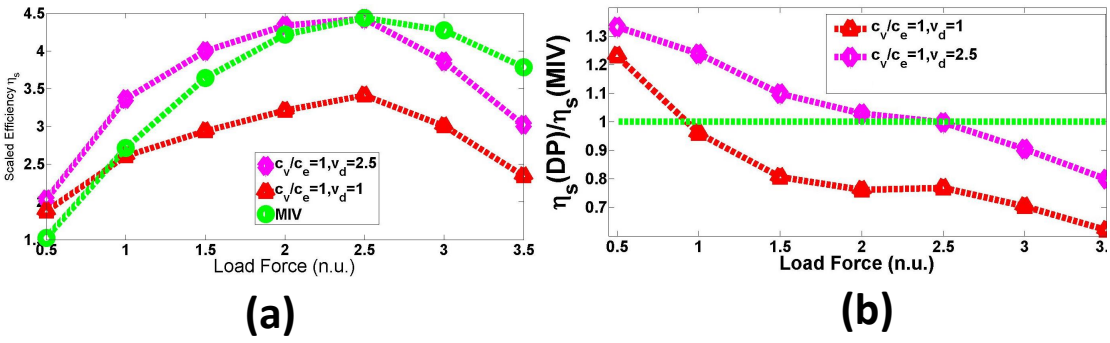

Figure 4.8: Comparison of efficiency achieved at different load forces for MIV strategy and dynamic programming. (a) shows the actual efficiencies achieved for different strategies while (b) shows the ratio of efficiency achieved of MIV strategy and dynamic programming for different optimization parameters.In (a), the green curve corresponds to open loop, red curve corresponds to dynamic programming with $c_v/c_e = 1, v_d = 1$ and magenta curve corresponds to dynamic programming with $c_v/c_e = 1, v_d = 2.5$. In (b), the red curve corresponds to the ratio $\frac{\eta_s(DP)}{\eta_s(MIV)}$ with $c_v/c_e = 1, v_d = 1$ for dynamic programming, the magenta curve corresponds to $\frac{\eta_s(DP)}{\eta_s(MIV)}$ with $c_v/c_e = 1, v_d = 2.5$ for dynamic programming and the green curve corresponds to $\frac{\eta_s(DP)}{\eta_s(MIV)} = 1$.

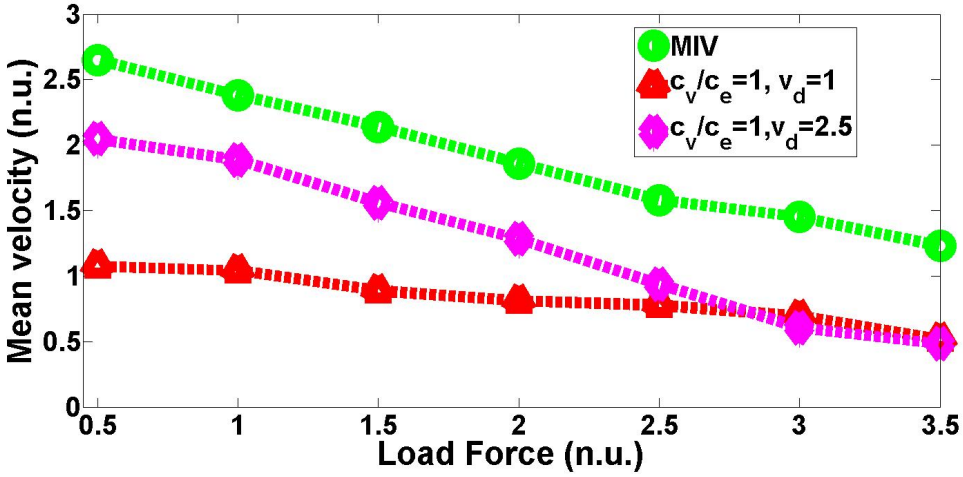

Figure 4.9: Comparison of velocity achieved at different load forces for MIV strategy and dynamic programming.(green: MIV strategy, red:$c_v/c_e = 1, v_d = 1$, magenta:$c_v/c_e = 1, v_d = 2.5$)

Finally, we compare the velocity yielded by MIV and DP. From Fig. 4.9 we can see that for low load conditions, the velocity achieved by DP is close to the specified optimization parameter v_d. Note that the velocity achieved by MIV strategy is more than that achieved by DP. As DP yields better efficiency till $F_{stall}/2$, it corroborates our assumption that maximizing velocity does not necessarily maximize efficiency, although that seems to be the case at higher load forces.

4.3.5 Analysis and discussion

From the results presented in the previous section, for lower load forces DP performs significantly better in terms of efficiency, whereas for higher load forces the performance of the MIV strategy is very close or even outperforms DP. To understand the reason behind this, let us consider Fig. 4.10, where the zones are so divided that, with the potential on, if a particle starts at zone 1, it will move forward and at the end of

the sampling interval it will end in zone 1 or zone 2, if a particle starts at zone 2, it will move forward and at the end of the sampling interval it will end in the adjacent valley and if a particle starts at zone 3, it will move backwards. The extent of zone 2 depends on the forward driving force $F_f = \frac{V_0}{(1-\alpha)L} - F_L$ and sampling time T_s as $\text{mod}(x_{Z2}, L) = F_f T_s$, where x_{Z2} is the starting point of zone 2. The extent of of zone 1 and zone 3 then becomes clear from Fig. 4.10.

In the MIV strategy, if the particle is located in zone 3 at the beginning of the sampling time, the potential is turned off and if it is in either zone 1 or zone 2, it is kept on. Thus, for the instances when the particle starts at zone 2, the input energy is not fully utilized to move the particle forward, as the particle may spend considerable amount of time being stuck at the valley depending on its starting position. The dynamic programming minimizes the idle time spent at the valleys with potential turned on by looking at the global solution and scheduling when to turn on (or off) the potential with the particle at zone 2 (and also for which fraction of zone 2) and thus achieves better efficiency than the MIV strategy. It should, however, be noted that the extent of zone 2 decreases with increase in the load force F_L, which in turn decreases F_f, and thus the advantage of dynamic programming over MIV is expected to go down with increase in load force.

Since with increase in load force F_L, the backward drift during a sampling interval with potential off $x_{bw} = -\frac{F_L}{\gamma} T_s$ increases, while the forward drift with potential on $x_{fw} = \frac{F_f}{\gamma} T_s$ decreases, to achieve same forward transport, we need more on intervals or less off intervals or both. In any case, this would decrease $< v > / e_f$ with increase in load force for same $< v >$. If $< v >$ is close to the maximum achievable limit, then for high enough load forces the advantage gained by keeping potential off with the particle in zone 2 may be more than offset by the negative drift suffered during that interval. Thus it can be seen from the results presented in the previous section that as the load

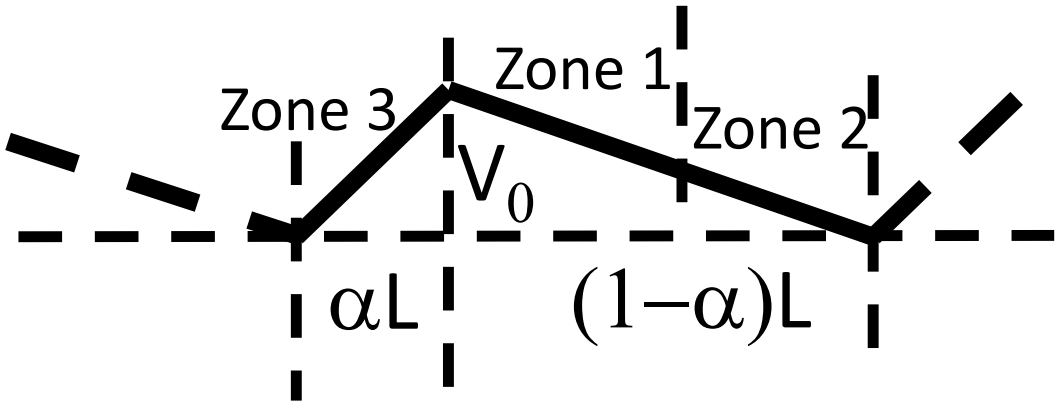

Figure 4.10: Different zones on the ratchet potential based on the starting and finishing position of the particles with the potential on.

force increases, the velocity at which maximum efficiency is achieved becomes closer to the velocity given by maximum achievable velocity. This also explains why the peak efficiency in open loop occurs at higher duty cycles for higher load forces. From the discussions in [56], it can be derived that in the limit maximum velocity is achieved for $e_{fl} := 1 - \frac{1}{\alpha}$. As discussed, higher load forces requires increase in e_f and thus our optimal strategy and MIV becomes similar in performance as $e_f \to e_{fl}$ for higher F_L.

It should also be noted that the assumptions that a particle located close enough to a valley would perfectly settle in the valley with the potential on and that thermal noise can be neglected with potential on is contingent upon the fact that the barrier height V_0 is much higher than $k_B T$. However, with increase in load force, the barrier height decreases as $-F_L(1-\alpha)L$ and thus error is introduced by the state update equation (4.22).

Another limitation of DP stems from its implementation via spatial gridding, which in turn may be limited by the computational power available or the resolution of the

position sensor. As the actions are computed recursively in dynamic programming, the error introduced due to finite spatial resolution at an early stage may be propagated among all the stages. Evidently, the penalty of such errors would be higher for higher load forces due to the increase in the negative drift term x_{bw}. The MIV strategy being a greedy strategy, the error introduced in a stage is not propagated and thus it is more robust towards spatial gridding at higher load forces. Thus, depending on the grid size Δ, coupled with the previously mentioned factors (decrease in span of zone 2, decrease in x_{fw} and increase in x_{bw} with increase in F_L), it may be possible for MIV strategy to perform better at significantly higher load forces. It should, however, be noted that this is a limitation of the implementation. Dynamic programming being an optimal strategy, if it was possible to choose an infinitesimally small grid size Δ, there would have always existed a combination of c_v, c_e and v_d that would have performed at least as good as MIV strategy for any load force.

4.4 Summary

This article provides important guidelines for the design of Brownian ratchets operated in the open-loop mode. Specifically, this article provides bounds on the load force which if exceeded result in negligible forward transport leading to stalling of the transport for any choice of on-time and off-time schedule for the ratchet potential. In the case that the load force does not cause stalling, the viable set of on-time and off-time schedules is determined that lead to appreciable transport in the desired forward direction. Assuming a viable choice of the schedule, it is shown that backward transport of particles will be small (with quantitative estimates provided) and furthermore transport of particles beyond a certain specified distance will be small. The results above are used to estimate an approximate form of the pdf of the particle position with the error in the estimation quantified. The approximate pdf is used to devise strategies that determine the optimal

schedules which maximize velocity and efficiency. Extensive Monte-Carlo simulations are presented to assess the analysis which corroborate the accuracy and effectiveness of analysis.

This article also develops an optimal strategy based on dynamic programming for maximization of efficiency of transport in closed-loop. To the best of our knowledge, this is the first such strategy that maximizes efficiency in closed-loop. In comparison to open-loop methods, this strategy has shown more than 2-3 times improvement in terms of efficiency. Also, for lower load forces, which includes the range of the load force in majority of applications, the strategy results in 35% improvement over other closed-loop strategies that focus on velocity maximization. Thus it is demonstrated that maximizing velocity may compromise efficiency. For many particle systems assuming the particles can be sensed, the developed closed-loop strategy can be used to maximize $\frac{< v_{cm} >}{e_f}$ for a particular load force; $< v_{cm} >$ being the average velocity of the center of mass. Methods based on approximate dynamic programming or reinforcement learning to circumvent the roadblock presented by the dimensionality of the problem are also worth considering, which constitutes our future work.

Chapter 5

Modeling and Role of Feedback Controlled Stochastic Ratchets in Cellular Transport

This work develops a model for Brownian ratchets to analyze the cases where the transport characteristics are affected by feedback mechanisms. One main application of this approach is to gain insights on the intracellular transport of motor proteins (such as Kinesin and Dynein) on a microtubular track, and on the role of feedback control on their transport. The model comprises of a stochastic system where the system switches between two stochastic differential systems, where the switching criteria is a state-dependent stochastic variable. Simulations demonstrate that the feedback mechanism helps achieve an increased average velocity of transport and corroborates the hypothesis that a motor protein can achieve higher speeds of transport by restricting or enabling attachment/detachment of ATP/ADP like molecules depending on conformational changes in the motor-protein.

5.1 Model

In the following we model a flashing ratchet, where the particle is under the influence of white noise, that switches between two potentials, such that the corresponding drift (forces) exerted on the particle are different. We describe the position $x(t)$ of an inertia-less particle under such a ratchet by the following two stochastic differential equations (SDE)

$$dx = f(x, \theta)dt + \sqrt{D}dW \tag{5.1}$$

where $\theta \in \{0, 1\}$, D is the Diffusion constant, and $W(t)$ is the Wiener process. The nondimesionalized potential $V(x, \theta)$, and therefore the corresponding force $f(x, \theta) = -\frac{\partial}{\partial x}V(x, \theta)$, acting on the particle switches (or flashes) between two functions, one defined for each θ ($\theta = 0$ or $\theta = 1$). The evolution of the switch-trigger parameter can be modeled to be deterministic with $\theta = 0$ for a duration t_{off} and on for a subsequent duration t_{on}, or can be modeled as a stochastic parameter. In this work, we assume a stochastic model for dynamics of θ where it has a certain switching rate. Thus the flashing ratchet model can be viewed as a stochastic hybrid system, where *both* the switch-trigger dynamics as well as individual system dynamics are stochastic.

In this paper we use the differential Chapman-Kolmogorov (DCK) equation [68] for modeling the transport of a particle under a flashing ratchet. In the DCK formulation, a partial differential equation is sought that describes the evolution of the probability density function $p(x, \theta, t|x_0, \theta_0, t_0)$, that is, it seeks the pdf of the random state (x, θ) at time t given that the state was (x_0, θ_0) at time t_0. Under fairly mild assumptions [68], this pde is completely determined by three functions - the drift $A(x, \theta, t)$, the diffusion $B(x, \theta, t)$, and the jump rates $Q(x, \theta|x_0, \theta_0, t)$ that we describe next.

5.1.1 Jump rate terms

The jump-rate from state (z, θ_0) to (x, θ) at time t is defined by (see [68])

$$Q(x, \theta|z, \theta_0, t) := \lim_{\Delta t \to 0} \frac{p(x, \theta, t + \Delta t|z, \theta_0, t)}{\Delta t} \tag{5.2}$$

under the assumptions that $|(x, \theta) - (z, \theta_0)| \geq \epsilon > 0$ and that the limit exists uniformly for all $x,\ z,\ t$ and $\epsilon > 0$. Intuitively $Q(x, \theta|z, \theta_0, t)\Delta t$ is the probability of finding the state to be at (x, θ) at time $t + \Delta t$ given that the state was at z, θ_0 at time t where Δt is vanishingly small. Evidently for processes with continuous sample paths $Q \equiv 0$. Suppose $\theta = \theta_0 = 0$ then $Q(x, \theta|z, \theta_0, t)$ is given by

$$\begin{aligned}
&\lim_{\Delta t \to 0} \frac{1}{\Delta t}[\frac{p(x, \theta, t + \Delta t|z, \theta_0, t)}{\Delta t}] \\
&= \lim_{\Delta t \to 0} p(x, t + \Delta t|z, t, \theta(t) = \theta(t + \Delta t) = 0) \\
&\times p(\theta(t + \Delta t) = 0|z, t, \theta(t) = 0).
\end{aligned}$$

When $\theta = \theta_0 = 0$ the particle is governed by the SDE $dx = f(x, 0)dt + \sqrt{D}dW$, which in turn can be interpreted as $x(t+\Delta t) - x(t) = f(x(t), 0)\Delta t + \sqrt{D}\Delta W$, where ΔW is a zero-mean Gaussian random variable with variance equal to Δt. Thus given that $x(t) = z$, the stochastic state at time $t + \Delta t$ is described by $x(t + \Delta t) = z + f(z, 0)\Delta t + \sqrt{D}\Delta W$, and its pdf is given by $p(x, 0, t+\Delta t|z, 0, t_0) = \frac{1}{\sqrt{2\pi D \Delta t}} e^{-(x-z-f(z,0)\Delta t)^2/(2D\Delta t)}$. Therefore $Q(x, 0|z, 0)$ is given by

$$\begin{aligned}
\lim_{\Delta t \to 0} \quad &[\frac{1}{\sqrt{2D(\Delta t)^3}} e^{-(x-z-f(z,0)\Delta t)^2/(2D\Delta t)}] \\
&\times [p(\theta(t + \Delta t) = 0|z, t, \theta(t) = 0)],
\end{aligned}$$

which evaluates to zero, since the above limit is zero for bounded $p(\theta(t + \Delta t) = 0|z, t, \theta(t) = 0)$, which will be satisfied by any reasonable model of switching dynamics. Similarly, we can show that when $\theta = \theta_0 = 1$ then $Q(x, \theta|z, \theta_0, t) = 0$.

Also, the jump-rate function $Q(x, \theta = 1|z, \theta_0 = 0, t)$ is given by

$$\begin{aligned}
&\lim_{\Delta t \to 0} \frac{1}{\Delta t}[\frac{p(x, \theta = 1, t + \Delta t|z, \theta_0, t)}{\Delta t}] \\
&= \lim_{\Delta t \to 0} p(x, t + \Delta t|z, t, \theta(t) = 0, \theta(t + \Delta t) = 1) \\
&\times p(\theta(t + \Delta t) = 1|z, t, \theta(t) = 0) \\
&= \lim_{\Delta t \to 0} p(x, t + \Delta t|z, t, \theta(t) = 0, \theta(t + \Delta t) = 1) \\
&\times \lim_{\Delta t \to 0} \frac{1}{\Delta t} p(\theta(t + \Delta t) = 1|z, t, \theta(t) = 0).
\end{aligned}$$

We assume that the position x of the particle is well behaved, that is, there is no instantaneous jump in the displacement of the particle when the ratchet flashes between two potentials. More specifically, we assume that as θ switches from 0 to 1,

$$\lim_{\Delta t \to 0} p(x, t + \Delta t|z, t, \theta(t) = 0, \theta(t + \Delta t) = 1) = \delta(x - z).$$

Furthermore we assume a model for switching dynamics from $\theta = 0$ to 1 given by

$$\lim_{\Delta t \to 0} \frac{1}{\Delta t} p(\theta(t + \Delta t) = 1|z, t, \theta(t) = 0) =: \lambda(z, 0).$$

Accordingly we have

$$Q(x, \theta = 1|z, \theta_0 = 0, t) = \delta(x - z)\lambda(z, 0).$$

Making analogous assumptions on the switching dynamics from $\theta = 1$ to $\theta = 0$, we get

$$Q(x, \theta = 0|z, \theta_0 = 1, t) = \delta(x - z)\lambda(z, 1).$$

5.1.2 Drift terms

The drift terms given by $A_z(z, \theta, t)$ and $A_\theta(z, \theta, t)$ (see [68]) are respectively defined by

$$\lim_{\Delta t \to 0} \frac{1}{\Delta t} \int_{\Omega_\epsilon} (x - z) p(x, \theta_0, t + \Delta t|z, \theta, t) dx d\theta_0$$

and

$$\lim_{\Delta t \to 0} \frac{1}{\Delta t} \int_{\Omega_\epsilon} (\theta_0 - \theta) p(x, \theta_0, t + \Delta t|z, \theta, t) dx d\theta_0,$$

where

$$\Omega_\epsilon = \{(x,\theta) \text{ such that} |(x,\theta_0) - (z,\theta)| \leq \epsilon\}.$$

Within the domain of integration, it is not possible for $\theta \neq \theta_0$ and thus $A_\theta = 0$ and $A_z(z,\theta,t)$ is given by

$$\begin{aligned}
&\lim_{\Delta t\to 0} \frac{1}{\Delta t} \int_{\Omega_\epsilon} (x-z) p(x,\theta_0, t+\Delta t|z,\theta,t) dx d\theta_0 \\
&= \lim_{\Delta t\to 0} \frac{1}{\Delta t} \int_{\Omega_\epsilon} (x-z) \times \\
&p(x,t+\Delta t|z,\theta,t;\theta_0,t+\Delta t) p(\theta_0,t+\Delta t|z,\theta,t) dx d\theta_0.
\end{aligned}$$

Since $(x,\theta) \in \Omega_\epsilon$, for all $\epsilon > 0$, it is not possible to have $\theta_0 \neq \theta$ in the region of integration and therefore

$$\begin{aligned}
A_z(z,\theta,t) &= \lim_{\Delta t\to 0} \frac{1}{\Delta t} \int_{|x-z|\leq\epsilon} (x-z) \\
&\quad \times p(x,t+\Delta t|z,\theta,t;\theta,t+\Delta t) dx.
\end{aligned}$$

Note that $p(x,t+\Delta t|z,\theta,t;\theta,t+\Delta t)$ is the pdf when the parameter dynamics is governed by the ratchet potential $f(z,\theta)$ which is a Gaussian with mean $z+f(z,\theta)\Delta t$ and variance $D\Delta t$. Thus $A_z(z,\theta,t)$

$$\begin{aligned}
&\lim_{\Delta t\to 0} \frac{1}{\Delta t} \int_{|x-z|\leq\epsilon} \frac{(x-z)}{\sqrt{2\pi D\Delta t}} e^{(x-z-f(z,\theta)\Delta t)^2/(2D\Delta t)} dx \\
&= \lim_{\Delta t\to 0} \frac{1}{\Delta t} \int_{|\xi|\leq\epsilon} \frac{\xi}{\sqrt{2\pi D\Delta t}} e^{(\xi-f(z,\theta)\Delta t))^2/(2D\Delta t)} d\xi \\
&= f(z,\theta).
\end{aligned}$$

5.1.3 Diffusion terms

The diffusion term are defined by $B_{zz}(z,\theta,t)$, $B_{\theta,z}(z,\theta,t)$ and $B_{\theta,\theta}(z,\theta,t)$, (see [68]) given by

$$\lim_{\Delta t\to 0} \frac{1}{\Delta t} \int_{\Omega_\epsilon} (x-z)^2 p(x,\theta_0,t+\Delta t|z,\theta,t) dx d\theta_0,$$

$$\lim_{\Delta t\to 0}\frac{1}{\Delta t}\int_{\Omega_\epsilon}(x-z)(\theta_0-\theta)$$
$$\times p(x,\theta_0,t+\Delta t|z,\theta,t)dxd\theta_0,$$

and

$$\lim_{\Delta t\to 0}\frac{1}{\Delta t}\int_{\Omega_\epsilon}(\theta_0-\theta)^2 p(x,\theta_0,t+\Delta t|z,\theta,t)dxd\theta_0$$

respectively. As was the case for the drift term, it is not possible for $\theta\neq\theta_0$ within the domain of integration and thus $B_{\theta,\theta}=B_{\theta,z}=0$ and $B_{zz}(z,\theta,t)$ is given by

$$\lim_{\Delta t\to 0}\int_{|(x-z|\leq\epsilon}\frac{(x-z)^2}{\Delta t}p(x,t+\Delta t|z,\theta,t;\theta,t+\Delta t)dx$$

which evaluates to the constant D.

5.1.4 The differential Chapman-Kolmogorov Equation for Brownian ratchets

The DCK equation is given by

$$\begin{aligned}
&\dot{p}(z,\theta,t|y,\theta_0,t_0)=-[f(z,\theta)p(z,\theta,t|y,\theta_0,t_0)]'\\
&+\frac{1}{2}Dp''(z,\theta,t|y,\theta_0,t_0)\\
&+\sum_{\overline{\theta}=0,1}\int[Q(z,\theta|x,\overline{\theta},t)p((x,\overline{\theta},t|y,\theta_0,t_0)\\
&-Q(x,\overline{\theta}|z,\theta,t)p(z,\theta,t|y,\theta_0,t_0)]dx,
\end{aligned}$$

which simplifies as

$$\begin{aligned}
&\dot{p}(z,\theta,t|y,\theta_0,t_0)=-[f(z,\theta)p(z,\theta,t|y,\theta_0,t_0)]'\\
&+\frac{1}{2}Dp''(z,\theta,t|y,\theta_0,t_0)\\
&+\lambda(z,1-\theta)p((z,1-\theta,t|y,\theta_0,t_0)\\
&-\lambda(z,\theta)p(z,\theta,t|y,\theta_0,t_0).
\end{aligned}\tag{5.3}$$

Here $\dot{(\cdot)}$ represents the partial derivative with respect to time, and $(\cdot)'$ and $(\cdot)''$ represent the first and second order partial derivatives with respect to the spatial variable.

5.2 Feedback-based switching

In this work, force terms $f(x,\theta)$ are derived from a sawtooth potential $V(x)$ (we assume $L = 1$ without any loss of generality). More specifically, $f(x,1) = -V'(x) + b$ and $f(x,0) = -V'(x) - a$, where $V(x)$ is given by

$$V(x) = \begin{cases} \frac{1}{1+2\alpha}(2x+1) \text{for } x \bmod 1 \in [-\frac{1}{2}, \alpha] \\ -\frac{1}{1+2\alpha}(2x-1) \text{for } x \bmod 1 \in [\alpha, \frac{1}{2}] \end{cases}, \tag{5.4}$$

and $\alpha \in (-\frac{1}{2}, \frac{1}{2})\backslash\{0\}$ to ensure *asymmetry*. The periodicity condition is satisfied as $V(x+1) = V(x)$, which makes the force $f(x)$ periodic as well. This choice of potential is motivated by the simplicity in its practical implementation (need to just change the force bias to enable flashing) as well as that it allows for a closed-form steady-state solution of the associated DCK (5.3). We incorporate state feedback by treating the switching rates as control parameters and designing the feedback laws $\lambda(x,0) =: \mu(x)$ and $\lambda(x,1) =: \nu(x)$ to be explicit functions of the realized (or measured) state x. In this work, for simplicity in analysis we assume that $\mu(x)$ and $\nu(x)$ are periodic with the same spatial period 1 as the potential $V(x)$. For a given initial condition (y, θ_0) at time t_0, if we represent $p(x,1,t|y,\theta_0,t_0)$ and $p(x,0,t|y,\theta_0,t_0)$ by $P^+(x,t)$ and $P^-(x,t)$ respectively, then the DCK (5.3) becomes

$$\begin{aligned} \dot{P}^+ &= -[(f(x)+b)P^+]' + DP^{+''} + \mu(x)P^- - \nu(x)P^+ \\ \dot{P}^- &= -[(f(x)-a)P^-]' + DP^{-''} - \mu(x)P^- + \nu(x)P^+. \end{aligned} \tag{5.5}$$

If we represent the total probability $P^+(x,t) + P^-(x,t)$ by $\hat{P}(x,t)$ and the average bias $bP^+(x,t) - aP^-(x,t)$ by $\hat{\Pi}(x,t)$, then (5.5) in these variables becomes

$$\dot{\hat{P}} \;=\; -[f(x)\hat{P} + \hat{\Pi} - D\hat{P}']' := \hat{J}'(x,t)$$

$$\begin{aligned}\dot{\hat{\Pi}} &= -[ba\hat{P} + (f(x)+\beta)\hat{\Pi}]' + D\hat{\Pi}'' \\ &\quad +\eta(x)\hat{P} - \tau^{-1}(x)\hat{\Pi}, \end{aligned} \tag{5.6}$$

where $\beta = b-a$, $\eta(x) = a\nu(x) - b\mu(x)$, and $\tau^{-1}(x) = \mu(x)+\nu(x)$. After noting that the above pde has spatially periodic coefficients, it is easy to verify that if $(\hat{P}(x,t), \hat{\Pi}(x,t))$ is a solution, then so is $(P(x,t), \Pi(x,t))$ where $P(x,t) = \sum_{n=-\infty}^{\infty} \hat{P}(x+n,t)$ and $\Pi(x,t) = \sum_{n=-\infty}^{\infty} bP^+(x+n,t) - aP^-(x+n,t)$. Thus $(P(x,t), \Pi(x,t))$ satisfies the pde (5.6). Also, note that the above definition implies periodicity in $P(x,t) = P(x+1,t)$ and also that $\int_0^1 P(x,t)dx = 1$ for all t (Note similarly $J(x,t) = \sum_{n=-\infty}^{\infty} \hat{J}(x+n,t)$ is also periodic). This change of variables is useful since it has periodic boundary conditions, for which it is easy to obtain the steady-state (stationary) solution (On the other hand, for $\hat{P}(x,t)$ we do not expect a stationary solution, since we expect the mean of the particle position to drift incessantly to the right with time). The stationary state $P(x) = \lim_{t\to\infty} P(x,t)$ and $\Pi(x) = \lim_{t\to\infty} \Pi(x,t)$ are given by substituting $\dot{P} = 0$ and $\dot{\Pi} = 0$) in (5.6), that is,

$$\begin{aligned}[f(x)P(x) + \Pi - DP'(x)]' := J'(x) = 0, \\ -[baP(x) + (f(x)+\beta)\Pi(x)]' + D\Pi''(x) \\ +\eta(x)P(x) - \tau^{-1}\Pi(x) = 0, \end{aligned} \tag{5.7}$$

and since $J'(x) = 0$, therefore the probability current $J(x) \equiv J^{st}$ is a constant. Hence we have,

$$\Pi(x) = J^{st} + D\partial_x P(x) - f(x)P(x). \tag{5.8}$$

We use (5.8) to eliminate $\Pi(x)$ from (5.7), and obtain the following ordinary differential equation:

$$\begin{aligned} D^2P'''(x) - D[\beta P''(x) + [f(x)P(x)]'' + [f(x)P'(x)]'] \\ +\beta[f(x)P(x)]' + [f^2(x)P(x)]' - \tau^{-1}(D+ba)P'(x) \\ +(\eta + \tau^{-1}f(x))P(x) = (f'(x) + \tau^{-1})J^{st}. \end{aligned} \tag{5.9}$$

Since $P(x)$ is periodic, it suffices to solve (5.9) in $[x_0, x_0+1]$ $\forall x_0 \in [-\frac{1}{2}, \alpha]$. Note that force $f(x)$ is piecewise constant of the form $f(x) = \sum_{j=1}^{3} f_j \Theta_j$, where $f_1 = f_3$,

$\Theta_1 = \Theta(\alpha - x)$, $\Theta_2 = \Theta(x - \alpha) - \Theta(x - \frac{1}{2})$, $\Theta_3 = \Theta(x - \frac{1}{2})$, and $\Theta(x)$ is the spatial-domain step function. If we choose the feedback laws to have the same structure, that is, $\mu(x) = \sum_{j=1}^{3} \mu_j \Theta_j$ and $\nu(x) = \sum_{j=1}^{3} \nu_j \Theta_j$ with $\mu_1 = \mu_3$ and $\nu_1 = \nu_3$, then it can be expected that the solution will be of the form given by $P(x) = \sum_{j=1}^{3} p_j(x)\Theta_j$ where $p_1(x) = p_3(x)$. On substituting these structures of $f(x), \mu(x), \nu(x)$, and $p(x)$ in (5.9), we obtain the following two third-order linear odes

$$\begin{aligned} & D^2 p_i'''(x) - D(\beta + 2f_i)p_i''(x) \\ & +(\beta f_i + f_i^2 - (ab + D\tau_i^{-1}))p_i'(x) \\ & +(\eta_i + f_i\tau_i^{-1})p_i(x) - J^{st}\tau_i^{-1} = 0 \end{aligned} \tag{5.10}$$

where $i \in \{1, 2\}$ and $\tau_i^{-1} = \mu_i + \nu_i$, and the following six conditions (see appendix for details)

$$\begin{aligned} & p_2(\alpha) = p_1(\alpha), p_1(-\frac{1}{2}) = p_2(\frac{1}{2}), \\ & D(p_2'(\alpha) - p_1'(\alpha)) = f_2 p_2(\alpha) - f_1 p_1(\alpha) \\ & D(p_2'(\frac{1}{2}) - p_1'(-\frac{1}{2})) = f_2 p_2(\frac{1}{2}) - f_1 p_1(-\frac{1}{2}) \\ & D^2(p_2''(\alpha) - p_1''(\alpha)) = 2D(f_2 p_2'(\alpha) - f_1 p_1'(\alpha)) \\ & -(f_2^2 p_2(\alpha) - f_1^2 p_1(\alpha)) + J^{st}(f_2 - f_1), \\ & D^2(p_2''(\frac{1}{2}) - p_1''(-\frac{1}{2})) = 2D(f_2 p_2'(\frac{1}{2}) - f_1 p_1'(-\frac{1}{2})) \\ & -(f_2^2 p_2(\frac{1}{2}) - f_1^2 p_1(-\frac{1}{2})) + J^{st}(f_2 - f_1). \end{aligned} \tag{5.11}$$

Note that we require six conditions for the sixth order ode in (5.10); however one more condition is needed to evaluate the constant J^{st}. This is obtained by requiring $\int_0^1 p(x)dx = 1$ which results in the following condition

$$\begin{aligned} 1 = & \left[\frac{(\alpha + \frac{1}{2})\tau_1^{-1}}{\eta_1 + f_1\tau_1^{-1}} + \frac{(\frac{1}{2} - \alpha)\tau_2^{-1}}{\eta_2 + f_2\tau_2^{-1}} \right] J^{st} \\ & -D^2 \left[\frac{(p_1''(\alpha) - p_1''(-\frac{1}{2}))}{\eta_1 + f_1\tau_1^{-1}} + \frac{p_2''(\frac{1}{2}) - p_2''(\alpha)}{\eta_2 + f_2\tau_2^{-1}} \right] \\ & +D \left[\frac{2f_1 + \beta}{\eta_1 + f_1\tau_1^{-1}}(p_1'(\alpha) - p_1'(-\frac{1}{2})) \right. \\ & \left. + \frac{2f_2 + \beta}{\eta_2 + f_2\tau_2^{-1}}(p_2'(\frac{1}{2}) - p_2'(\alpha)) \right] \end{aligned}$$

$$-\frac{f_1^2+\beta f_1-(ab+D\tau_1^{-1})}{\eta_1+f_1\tau_1^{-1}}((p_1(\alpha)-p_1(-\frac{1}{2}))$$
$$-\frac{f_2^2+\beta f_2-(ab+D\tau_2^{-1})}{\eta_2+f_2\tau_2^{-1}}((p_1(\alpha)-p_1(-\frac{1}{2})). \quad (5.12)$$

The solution of the linear odes (5.10) are of the form

$$p_i(x)=\Gamma_{i1}e^{\lambda_{i1}x}+\Gamma_{i2}e^{\lambda_{i2}x}+\Gamma_{i3}e^{\lambda_{i3}x}+\frac{J^{st}\tau_i^{-1}}{\eta_i+f_i\tau_i^{-1}}, \quad (5.13)$$

where the modes $\lambda_{ij}, j\in\{1,2,3\}$ are the three roots of the characteristic equations

$$D^2\lambda_i^3-D(\beta+2f_i)\lambda_i^2+(\beta f_i+f_i^2-(ab+D\tau_i^{-1}))\lambda_i$$
$$+(\eta_i+f_i\tau_i^{-1})=0, \quad (5.14)$$

and the constants Γ_{ij} ($i\in\{1,2\}$ and $j\in\{1,2,3\}$) and J^{st} can be determined by substituting the conditions (5.11) and (5.12) in (5.13). Note that the design parameters are the feedback laws $\mu(x)$ and $\nu(x)$; and therefore by designing parameters μ_i and ν_i ($i\in\{1,2\}$), one can change the solution of (5.10) and thereby effecting a change in the transport characteristics of the flashing ratchet.

5.3 Simulation Results

In this section, we demonstrate the advantage of the feedback control by designing the control parameters such that the average steady-state velocity of the particle is increased. The average velocity at time t is defined as $<v(t)>=\frac{d}{dt}\int_{-\infty}^{\infty}x\hat{P}(x,t)dx$; which is given by

$$\begin{aligned}<v(t)> &= \int_{-\infty}^{\infty}x\dot{\hat{P}}(x,t)dx=-\int_{-\infty}^{\infty}x\hat{J}'(x,t)dx\\ &= \underbrace{[x\hat{J}(x,t)]_{-\infty}^{\infty}}_{=0}+\int_{-\infty}^{\infty}\hat{J}(x,t)dx\\ &= \sum_{n=-\infty}^{\infty}\int_0^1\hat{J}(x,t)dx=\int_0^1 J(x,t)dx, \quad (5.15)\end{aligned}$$

where we have used (5.6) to obtain the second equality in the first line, integration-by-parts identity in the second line, and the definition of $J(x,t)$ for the last equality. Thus

as $t \to \infty$ (steady-state), $< v_\infty >= J^{st}$, the steady-state value for $J(x,t)$. This implies that design parameters μ_i and ν_i that result in higher values of J^{st} determined by (5.10)-(5.13) lead to higher average steady-state velocities of the particle. Figure 5.1 shows that with feedback, the average steady-state velocities are significantly higher than those obtained without feedback. In this simulation, all parameters for feedback and no-feedback case were kept identical except for the design variables. For state-feedback case, the switching rates depended on the state locations ($\mu_2 = \rho\mu_1$, $\nu_2 = \rho\nu_1$) (where ρ was incremented from 1.1-2 at steps of 0.1); while for the no-feedback case the switching rates were independent of the state-locations ($\mu_2 = \mu_1$, $\nu_2 = \nu_1$). The parameters μ_1 for the two cases were chosen the same (and likewise for the ν_1 parameters). This feedback scheme increases the switching rate, whenever it finds the state-location at the steep part of the potential (i.e. during opposing force); and thus achieves higher average velocities.

The motor-protein based transport can realize this feedback scheme whereby the rate of switching depends on the position of the motor domain (see Figure 4.1) where the microtubule dimer unit is viewed as a dipole moment. Indeed it is possible that the motor protein is so designed that space where the ATP/ADP molecule can attach to the motor-domain is closed when the motor-domain is in the later $(1-\alpha)$ fraction of the dipole length and the space is accessible when the motor-domain is in the first α fraction of the dipole length. Thus in the first α fraction, the rate of attachment and detachment will be higher when compared to the latter $(1-\alpha)$ fraction. Thus with this natural feedback in place the motor protein may enable faster transport of cargo along the MT tracks.

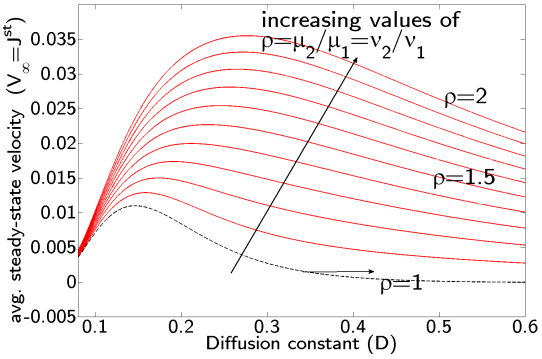

Figure 5.1: Improvement in average steady-state velocity of the particle under flashing Brownian ratchet by applying state-feedback control. For both feedback (solid, $\rho > 1$) and no-feedback (dashed, $\rho = 1$) cases, the following parameters were assumed: asymmetry $\alpha = 0.25$, up-bias $b = 0.693$, down-bias $a = 1.443$, up-switching rate $\mu_1 = 0.7506$, and down-switching rate $\nu_1 = 0.3605$. For the feedback case $(\mu_2, \nu_2) = \rho(\mu_1, \nu_1)$, while for the no-feedback case $(\mu_2, \nu_2) = (\mu_1, \nu_1)$.

5.4 Discussion and Conclusions

As discussed earlier, the study in this article yields an interesting hypothesis on how motor proteins can enhance the speed of transport of cargo by using an intrinsic feedback scheme that alters the rate of switching between two ratchet potentials. Note that if we set $\eta(x) = 0$ in (5.7), the rates $\mu(x)$ and $\nu(x)$ do not appear separately but only their sum $\tau^{-1}(x) = \mu(x) + \nu(x)$ determines the equation. The function $\eta(x) = b\mu(x) - a\nu(x)$ is indicative of the average bias value over the underlying sawtooth potential $V(x)$. Therefore, typically for constant switching rates strategies, η is typically chosen to be zero since this bias value can be absorbed into the potential $V(x)$. In such a case, since the model does not distinguish between the up and down rates (μ and ν), this provides a good implementation insight - that choose μ and ν such that $\frac{\mu}{\nu} = \frac{a}{b}$. The above arguments hold even when the switching rates are state dependent; however the effects are not as clear as the potential $V(x)$ gets augmented by another function $\eta(x)$

and not a constant. In the simulations presented above we chose parameters such that $\eta(x) = 0$, and therefore the results herein demonstrates the increase in velocity due to feedback even when there is no modification of the underlying potential. This is in agreement with the fact that a motor protein can achieve higher speeds of transport simply by restricting or enabling attachment/detachment of ATP/ADP like molecules depending on conformational changes (and hence affecting the switching rates) in the motor-protein, while leaving the underlying potential unaltered. This hypothesis has to be supported by experiments as well as more detailed model of the motor-protein based transport which is a part of the future work.

Chapter 6

Conclusion and Discussion

A key contribution of my research is a novel disturbance estimation paradigm that is applicable to a wide class of systems where one needs to regulate a certain system variable against an external disturbance while simultaneously providing a real-time estimate of the disturbance. In general this disturbance is corrupted by process noise (which for nano-scale systems is primarily thermal noise) and the disturbance estimation scheme has to mitigate the effect of such noise. Here I have invoked and extended advanced control system tools and techniques. The main concepts are based on LMI based mixed objective synthesis and modern robust control paradigm. Examples of such systems include but not limited to optical probing of motor proteins and DNA, in situ measurements of fluid flow and viscosity in microfluidic channels, topography imaging based on scanning probe microscopy and high density data storage systems. The paradigm developed is applied to yield state-of-the art method for maintaining femto-Newton force on micro-scale particles and measuring nanometer scale motions at an order of magnitude higher temporal scales in scientific instruments which employ optical fields based probing and manipulations.

Prior to my research on disturbance estimation with simultaneous regulation of other

system variables, in particular for force regulation based on optical fields, a constrained framework was used that did not leverage the benefits of modern control paradigm. Most of the other force-regulation schemes were single-input single-output strategies which are not suitable for the multi-objective criteria imposed by the problem specifications. Ad hoc controllers are utilized for control and estimation is done off-line separately. With modern control framework, it is possible to address problems where different system measures can be posed on different transfer function (for example, minimizing the H2 norm of a transfer function while constraining the Hinfity norm of another). Furthermore I have demonstrated that the strategies developed are implementable in an embedded platform. In the particular context of the optical field based probing and manipulation, I have demonstrated more than an order of magnitude improvement in performance. This optimal force clamp will enable biologists to study motor proteins at in-vivo speeds which is not currently possible.

Another contribution of my research are systems that switch between different stochastic and deterministic subsystems in the presence of noise. In particular I have studied Brownian ratchet based transport mechanisms where I have used physical insights to reduce the model complexity to analytically derive the approximate evolution of the probability density function of the system state. Here I have demonstrated that judicious insights of the physical system can be used to obtain lower and upper bounds on the error between the approximation and the true pdf. I used extensive Monte-Carlo simulations to demonstrate the effectiveness of my approach. In another related effort, I have shown the advantages of using closed-loop strategies over open-loop strategies using dynamic programming methodology. Here a key insight obtained is the maximizing velocity of transport can significantly compromise efficiency of transport; an aspect not realized/emphasized by researchers in the area. Also, the developed strategy being optimal would serve as the benchmark for other heuristic/sub-optimal strategies

based on approximate dynamic programming or model predictive control (required to tackle computational complexity for high number of particles) for their performance evaluation.

Appendix A

Experimental Setup

The compact optical tweezer system used for experimentation developed in house (see Fig. A.1(c)) mainly consists of four parts: the trapping system (the main plant), the actuation system, the detection (or sensing) system and the control hardware, which is briefly discussed next.

The trapping system: A 1064 nm wavelength trapping laser source (Laser Quantum, Model Ventus IR 4W s-polarized) is expanded through appropriate optics to fill the back aperture of a high NA objective (Nikon 100x, 1.4 NA, oil immersion). Thus the laser forms a focal point in the sample plane immediately after the objective (see Fig. A.1(a)) where the beads can be trapped.

The actuation system: The trapping laser is passed through a 2-axis acousto-optic-deflector (AOD, IntraAction Corp., DTD-274HA6) (see Fig. A.1(a)) that is capable of steering the beam precisely when subject to appropraite commands. A conjugate lens system ensures that the deflection imparted to the beam via AOD is carried out on the sample plane which is far apart from the AOD (see Fig. A.1(b)), thereby allowing precise manipulation of the trapped particles.

The detection system: Detection laser (Point Source Inc., iFLEX 2000, 50 mW,

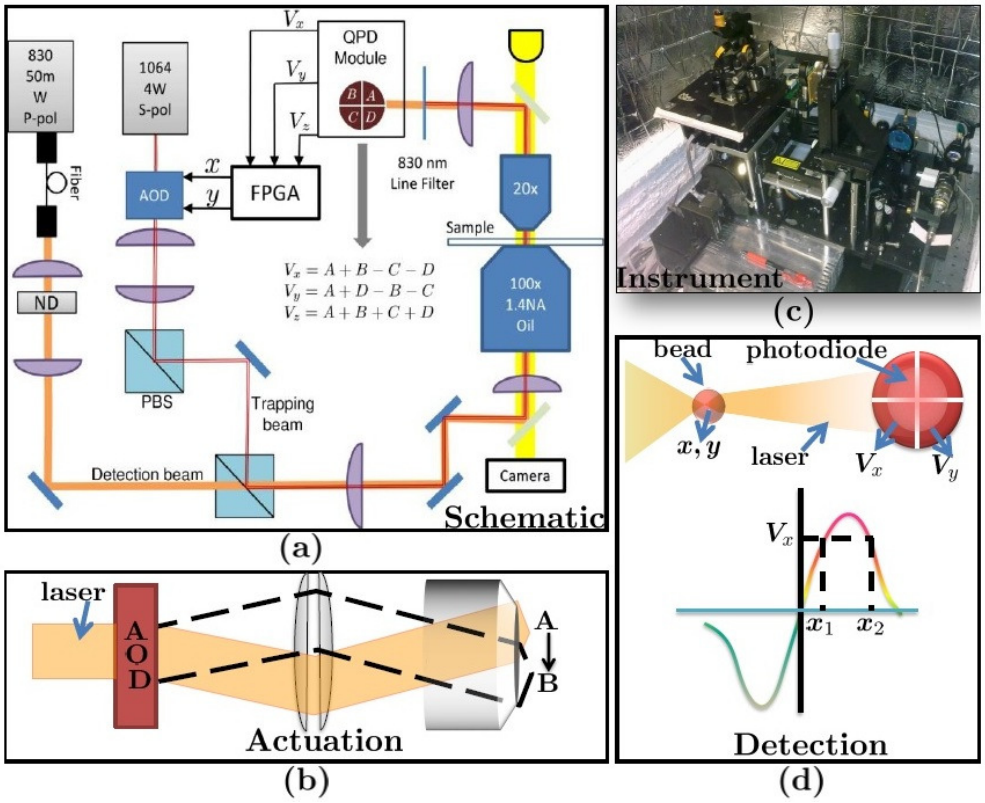

Figure A.1: (a) The schematics of an optical tweezer setup: The trapping laser with 1064 nm passes through a AOD (that can actuate the laser direction at high bandwidth) and fills the back aperture of the high NA objective. The trap is formed on the sample plane. A detection laser (830 nm wavelength) detects the beads position via a quadrant photodiode QPD. (b) The principle of actuation via AOD: The translation of laser by the AOD is carried out in the sample plane with the help of the pair of conjugate lenses. (c) A compact setup developed in-house to minimize effects of external disturbances. (d) The detection scheme: The bead acts as a lens for the laser passing through and the nonlinear relationship of the output voltage V of the photodiode with respect to bead position x_b. All operations are carried out in the linear region only.

830 nm, p-polarized) is added collinear to the trapping laser using a polarizing beam splitter cube (PBS). Intensity of the detection beam is reduced by placing a neutral density filter (ND) in its path to avoid trapping. After passing through the sample, the beams are collected by a condenser (40x objective). The trapping laser is blocked using a laser line filter (Thorlabs, FL830-10) and the back-focal-plane image of the detection laser is imaged onto a quadrant photodiode (Pacific Silicon Sensors, QP50-6SD2) with integrated amplifier circuit. The photodiode module provides three signals V_x, V_y and V_z that represent asymmetry of light distribution on the photodiode along x coordinate, along y coordinate and the total intensity of light respectively (see Fig. A.1(d)).

The control hardware: The detection signals are captured by a FPGA (Field Programmable Gate Array) based data acquisition card (National Instruments, 7833R, 200kHz sampling rate possible). It then processes the signals according to the control algorithms written in it and generates appropriate control signals for the AOD.

Appendix B

Protocol for Kinesin Bead Assay

B.1 Preparation

B.1.1 Saline treatment of coverslip

1. Wash coverslip with detergent, then with ultrapure H_2O
2. After drying, soak coverslip in 20 % solution of 3-aminoprophyl-triethoxysaline in acetone for 15 minutes
3. Rinse briefly with acetone
4. Rince with H_2O
5. Soak coverslip in water for 15 minutes, 3x shake and air dry

B.1.2 Oxygen Scavenging (OS) system

1. Thaw glucose oxidase, catalase and glucose solution on ice. Prepare 1xBRB80 solution
2. Take 36μl of 1xBRB80

3. Add 6μl glucose oxidase
4. Add 6μl catalase
5. Add 6μl of 50% 2-mercaptoethanol
6. Add 6μl glucose

B.2 Bead preparation and motor binding

B.2.1 Bead Casein solution

1. Take 12.5μl of beads (1 micron diameter, Spherotech, carboxylated beads)
2. Add 20μl of 10 mg/ml casein
3. Add 17.5μl of 1xBRB80
4. Place this solution in an ice bath and sonicate for 1-2 hours

B.2.2 Bead Motor stock

1. Thaw 20nM stock of DmKHC
2. Add 10μl casein coated beads, obtained form sonication
3. Add 36μl of BRB80CA (179μl 1xBRB + 1μl of 1mM ATP + 20μl of 10 mg/ml casein)
4. Add 4μl of DmKHC
5. Place this bead-motor stock on ice for 1 hour

B.2.3 Bead Motility buffer

1. Take 92.25μl of 1xBRB80
2. Add 5μl of 10 mg/ml casein
3. Add 2.5μl of 0.1M ATP
4. Add 0.25μl of 10mM Taxol

B.2.4 Blocking buffer

1. Take 440μl of MTB buffer
2. Add 10μl of 100 mg/ml BSA
3. Add 50μl of oxygen scavenging solution, prepared earlier

B.3 Performing the Assay

B.3.1 Mictotubule buffer (MTB)

1. Take 984μl of 1xBRB80
2. Add 1μl of 10mM Taxol
3. Add 10μl of 0.1M GTP
4. Add 5μl of 0.2M DTT

B.3.2 Bind microtubules and block chamber

- Prepare bead motility chamber. Use previously prepared saline coated coverslips and a cut slide to prepare motility chamber of volume approximately 3μl

- Dilute rhodamine labelled microtubules 1:20 in MTB
- Flush 10μl of dilute MT into the motility chamber for 10 minutes. Incubate in moist chamber
- Flow 10μl of blocking buffer and incubate in moist chamber for 10 minutes

B.3.3 Make up and introduce Final Motility Solution

- Dilute bead motor stock 1:10 in BRB80CA
- Take 11.5μl of 1xBRB80
- Add 10μl of Bead motility buffer
- Add 2.5μl of OS solution
- Add 1μl of the diluted bead motor stock
- Flow 15μl of final motility solution into the chamber

References

[1] Matthew J Lang, Charles L Asbury, Joshua W Shaevitz, and Steven M Block. An automated two-dimensional optical force clamp for single molecule studies. *Biophysical journal*, 83(1):491–501, 2002.

[2] Nobutaka Hirokawa, Yasuko Noda, Yosuke Tanaka, and Shinsuke Niwa. Kinesin superfamily motor proteins and intracellular transport. *Nature reviews Molecular cell biology*, 10(10):682–696, 2009.

[3] Gorazd B Stokin, Concepción Lillo, Tomás L Falzone, Richard G Brusch, Edward Rockenstein, Stephanie L Mount, Rema Raman, Peter Davies, Eliezer Masliah, David S Williams, et al. Axonopathy and transport deficits early in the pathogenesis of alzheimer's disease. *Science*, 307(5713):1282–1288, 2005.

[4] William J Greenleaf, Michael T Woodside, and Steven M Block. High-resolution, single-molecule measurements of biomolecular motion. *Annual review of biophysics and biomolecular structure*, 36:171, 2007.

[5] Koen Visscher and Steven M Block. [38] versatile optical traps with feedback control. *Methods in enzymology*, 298:460–489, 1998.

[6] Rajalakshmi Nambiar, Arivalagan Gajraj, and Jens-Christian Meiners. All-optical constant-force laser tweezers. *Biophysical journal*, 87(3):1972–1980, 2004.

[7] William J Greenleaf, Michael T Woodside, Elio A Abbondanzieri, and Steven M Block. Passive all-optical force clamp for high-resolution laser trapping. *Physical review letters*, 95(20):208102, 2005.

[8] Subhrajit Roychowdhury, Tanuj Aggarwal, Srinivasa Salapaka, and Murti V Salapaka. High bandwidth optical force clamp for investigation of molecular motor motion. *Applied Physics Letters*, 103(15):153703, 2013.

[9] Subhrajit Roychowdhury, Shreyas Bhaban, Srinivasa Salapaka, and Murti Salapaka. Design of a constant force clamp and estimation of molecular motor motion using modern control approach. pages 1525–1530, 2013.

[10] Hullas Sehgal, Tanuj Aggarwal, and Murti V Salapaka. High bandwidth force estimation for optical tweezers. *Applied Physics Letters*, 94(15):153114–153114, 2009.

[11] Tanuj Aggarwal, Hullas Sehgal, and Murti Salapaka. Robust control approach to force estimation in a constant position optical tweezers. *Review of Scientific Instruments*, 82(11):115108–115108, 2011.

[12] AlexE. Knight, Gregory Mashanov, and JustinE. Molloy. Single molecule measurements and biological motors. *European Biophysics Journal*, 35(1):89–89, 2005.

[13] Katsuhiko Ogata. *Modern control engineering (3rd ed.)*, 1997.

[14] Carsten Scherer, Pascal Gahinet, and Mahmoud Chilali. Multiobjective output-feedback control via lmi optimization. *Automatic Control, IEEE Transactions on*, 42(7):896–911, 1997.

[15] K. Svoboda, C.F. Schmidt, B.J. Schnapp, and S.M. Block. Direct observation of kinesin stepping by optical trapping interferometry. *Nature*, 365(6448):721–727, 1993.

[16] L.S. Milescu, A. Yildiz, P.R. Selvin, and F. Sachs. Maximum likelihood estimation of molecular motor kinetics from staircase dwell-time sequences. *Biophysical journal*, 91(4):1156–1168, 2006.

[17] B.C. Carter, M. Vershinin, and S.P. Gross. A Comparison of Step-Detection Methods: How Well Can You Do? *Biophysical Journal*, 94(1):306–319, 2008.

[18] S. Liepelt and R. Lipowsky. Operation modes of the molecular motor kinesin. *Phys. Rev. E*, 79:011917, 2009.

[19] DB Hill, MJ Plaza, K. Bonin, and G. Holzwarth. Fast vesicle transport in pc12 neurites: velocities and forces. *European Biophysics Journal*, 33(7):623–632, 2004.

[20] C. Kural, H. Kim, S. Syed, G. Goshima, V. I. Gelfand, and P. R. Selvin. Kinesin and dynein move a peroxisome in vivo: a tug-of-war or coordinated movement? *Science*, 308(5727):1469–1472, 2005.

[21] Ambarish Kunwar, Michael Vershinin, Jing Xu, and Steven P. Gross. Stepping, strain gating, and an unexpected force-velocity curve for multiple-motor-based transport. *Current biology*, 18:1173, 2008.

[22] C. Leduc, F. Ruhnow, J. Howard, and S. Diez. Detection of fractional steps in cargo movement by the collective operation of kinesin-1 motors. *Proceedings of the National Academy of Sciences*, 104(26):10847, 2007.

[23] Virupakshi Soppina, Arpan Kumar Rai, Avin Jayesh Ramaiya, Pradeep Barak, and Roop Mallik. Tug-of-war between dissimilar teams of microtubule motors regulates transport and fission of endosomes. *PNAS*, 106(46):19381–19386, 2009.

[24] T. Aggarwal and M. Salapaka. Real-time nonlinear correction of back-focal-plane detection in optical tweezers. *Review of Scientific Instruments*, 81(12):123105–123105, 2010.

[25] E. Meyhöfer and J. Howard. The force generated by a single kinesin molecule against an elastic load. *Proceedings of the National Academy of Sciences of the United States of America*, 92(2):574, 1995.

[26] M.E. Fisher and A.B. Kolomeisky. Simple mechanochemistry describes the dynamics of kinesin molecules. *Proceedings of the National Academy of Sciences of the United States of America*, 98(14):7748, 2001.

[27] R. E. Lee DeVille and Eric Vanden-Eijnden. Regularity and synchrony in motor proteins. *Bulletin of Mathematical Biology*, 70(2):484–516, 2008.

[28] S. Klumpp and R. Lipowsky. Cooperative cargo transport by several molecular motors. *Proceedings of the National Academy of Sciences of the United States of America*, 102(48):17284, 2005.

[29] Filippo Posta, Maria R. D'Orsogna, and Tom Chou. Enhancement of cargo processivity by cooperating molecular motors. *PCCP*, 11:4851 – 4860, 2009.

[30] A. Kunwar and A. Mogilner. Robust transport by multiple motors with nonlinear force–velocity relations and stochastic load sharing. *Physical biology*, 7(1):016012, 2010.

[31] F. Berger, C. Keller, S. Klumpp, and R. Lipowsky. Distinct transport regimes for two elastically coupled molecular motors. *Physical Review Letters*, 108(20):208101, 2012.

[32] Donatello Materassi, Subhrajit Roychowdhury, Thomas Hays, and Murti Salapaka. An exact approach for studying cargo transport by an ensemble of molecular motors. *BMC biophysics*, 6(1):14, 2013.

[33] Donatello Materassi, Subhrajit Roychowdhury, and Murti V Salapaka. A stochastic markov model for coordinated molecular motors. *arXiv preprint arXiv:1012.4191*, 2010.

[34] J.W. Driver, A.R. Rogers, D.K. Jamison, R.K. Das, A.B. Kolomeisky, and M.R. Diehl. Coupling between motor proteins determines dynamic behaviors of motor protein assemblies. *Phys. Chem. Chem. Phys.*, 12(35):10398–10405, 2010.

[35] J. L. Doob. Markoff chains - Denumerable case. *Transactions of the American Mathematical Society*, 58:455–473, 1945.

[36] D.T. Gillespie. Exact stochastic simulation of coupled chemical reactions. *The journal of physical chemistry*, 81(25):2340–2361, 1977.

[37] C. Leduc, O. Campàs, K.B. Zeldovich, A. Roux, P. Jolimaitre, L. Bourel-Bonnet, B. Goud, J.F. Joanny, P. Bassereau, and J. Prost. Cooperative extraction of membrane nanotubes by molecular motors. *Proceedings of the National Academy of Sciences of the United States of America*, 101(49):17096–17101, 2004.

[38] J. Beeg, S. Klumpp, R. Dimova, R.S. Gracia, E. Unger, and R. Lipowsky. Transport of beads by several kinesin motors. *Biophysical journal*, 94(2):532–541, 2008.

[39] Jing Xu, Zhanyong Shu, Stephen J King, and Steven P Gross. Tuning multiple motor travel via single motor velocity. *Traffic*, 13(9):1198–1205, 2012.

[40] R.D. Astumian. Thermodynamics and kinetics of a brownian motor. *Science*, 276(5314):917, 1997.

[41] Toshinori Motegi, Hideki Nabika, and Kei Murakoshi. Enhanced brownian ratchet molecular separation using a self-spreading lipid bilayer. *Langmuir*, 28(16):6656–6661, 2012.

[42] Hidenori Otsuka, Yukio Nagasaki, and Kazunori Kataoka. Self-assembly of poly (ethylene glycol)-based block copolymers for biomedical applications. *Current Opinion in Colloid & Interface Science*, 6(1):3–10, 2001.

[43] Erik M Roeling, Wijnand Chr Germs, Barry Smalbrugge, Erik Jan Geluk, Tjibbe de Vries, René AJ Janssen, and Martijn Kemerink. Organic electronic ratchets doing work. *Nature materials*, 10(1):51–55, 2011.

[44] Alexander Van Oudenaarden and Steven G Boxer. Brownian ratchets: molecular separations in lipid bilayers supported on patterned arrays. *Science*, 285(5430):1046–1048, 1999.

[45] Lawrence SB Goldstein and Zhaohuai Yang. Microtubule-based transport systems in neurons: the roles of kinesins and dyneins. *Annual review of neuroscience*, 23(1):39–71, 2000.

[46] Kristen J Verhey, Neha Kaul, and Virupakshi Soppina. Kinesin assembly and movement in cells. *Annual review of biophysics*, 40:267–288, 2011.

[47] ND Derr, BS Goodman, R Jungmann, AE Leschziner, WM Shih, and SL Reck-Peterson. Tug-of-war in motor protein ensembles revealed with a programmable dna origami scaffold. *Science*, 338(6107):662–665, 2012.

[48] Nicholas Stephanopoulos, Earl OP Solis, and George Stephanopoulos. Nanoscale process systems engineering: Toward molecular factories, synthetic cells, and adaptive devices. *AIChE journal*, 51(7):1858–1869, 2005.

[49] Adam JM Wollman, Carlos Sanchez-Cano, Helen MJ Carstairs, Robert A Cross, and Andrew J Turberfield. Transport and self-organization across different length scales powered by motor proteins and programmed by dna. *Nature nanotechnology*, 2013.

[50] R.P. Feynman, R.B. Leighton, M. Sands, et al. *The Feynman lectures on physics*, volume 2. Addison-Wesley Reading, MA, 1964.

[51] P. Reimann and P. Hanggi. Introduction to the physics of brownian motors. *Applied Physics A: Materials Science and Processing*, 75:169–178, 2002. 10.1007/s003390201331.

[52] R. Dean Astumian and Martin Bier. Fluctuation driven ratchets: Molecular motors. *Phys. Rev. Lett.*, 72:1766–1769, Mar 1994.

[53] Martin Bier. Processive motor protein as an overdamped brownian stepper. *Physical review letters*, 91(14):148104, 2003.

[54] Srinivasa Salapaka, Subhrajit Roychowdhury, and Murti Salapaka. Modeling and role of feedback controlled stochastic ratchets in cellular transport. In *Decision and Control (CDC), 2012 IEEE 51st Annual Conference on*, pages 374–379. IEEE, 2012.

[55] M. Feito and F. J. Cao. Time-delayed feedback control of a flashing ratchet. *Phys. Rev. E*, 76:061113, Dec 2007.

[56] F. J. Cao, L. Dinis, and J. M. R. Parrondo. Feedback control in a collective flashing ratchet. *PHYS.REV.LETT.*, 93:040603, 2004.

[57] Subhrajit Roychowdhury, Govind Saraswat, and Murti V Salapaka. Dynamic programming based approach for optimal transport by flashing ratchet against a load force. In *Control Applications (CCA), 2013 IEEE International Conference on*, pages 1105–1110. IEEE, 2013.

[58] E.M. Craig, N.J. Kuwada, B.J. Lopez, and H. Linke. Feedback control in flashing ratchets. *Annalen der Physik*, 17(2-3):115–129, 2008.

[59] Subhrajit Roychowdhury, Govind Saraswat, Srinivasa Salapaka, and Murti Salapaka. On control of transport in brownian ratchet mechanisms. *Journal of Process Control*, 2014.

[60] LP Faucheux, LS Bourdieu, PD Kaplan, and AJ Libchaber. Optical thermal ratchet. *Physical review letters*, 74(9):1504, 1995.

[61] Benjamin J Lopez, Nathan J Kuwada, Erin M Craig, Brian R Long, and Heiner Linke. Realization of a feedback controlled flashing ratchet. *Physical review letters*, 101(22):220601, 2008.

[62] H. Linke, M.T. Downton, and M.J. Zuckermann. Performance characteristics of brownian motors. *Chaos*, 15(2):26111, 2005.

[63] Subhrajit Roychowdhury, Srinivasa Salapaka, and Murti Salapaka. Maximizing transport in open loop for flashing ratchets. In *American Control Conference (ACC), 2012*, pages 3210–3215. IEEE, 2012.

[64] D. Lacoste and K. Mallick. Fluctuation theorem for the flashing ratchet model of molecular motors. *Phys. Rev. E*, 80:021923, Aug 2009.

[65] Dragoslav S Mitrinović, Josip E Pečarić, and AM Fink. Bernoullis inequality. In *Classical and New Inequalities in Analysis*, pages 65–81. Springer, 1993.

[66] Daisuke Suzuki and Toyonori Munakata. Rectification efficiency of a brownian motor. *Physical Review E*, 68(2):021906, 2003.

[67] Dimitri P Bertsekas. *Dynamic programming and optimal control*, volume 1. Athena Scientific Belmont, 1995.

[68] Crispin Gardiner. Stochastic methods: A handbook for the natural and social sciences springer series in synergetics. *Springer, Berlin, Germany*, 2009.